DESIGN AND ANALYSIS OF FLUORESCENT Ce:YAG SOLAR CONCENTRATOR

DESIGN AND ANALYSIS OF FLUORESCENT Ce:YAG SOLAR CONCENTRATOR

BY

ABRAR SIDAHMED

B. ENG.

A THESIS

SUBMITTED TO THE MATERIALS SCIENCE & ENGINEERING

AND THE SCHOOL OF GRADUATE STUDIES

OF MCMASTER UNIVERSITY

IN PARTIAL FULFILMENT OF THE REQUIREMENTS

FOR THE DEGREE OF

MASTER OF APPLIED SCIENCE

MASTER OF APPLIED SCIENCE (2014) McMaster University

Department of Materials Science and Engineering Hamilton, Ontario

TITLE: Design and Analysis of Fluorescent Ce:YAG Solar Concentrator

AUTHOR: Abrar Sidahmed

B. Eng. (Materials Science & Engineering)

McMaster University, Hamilton, Ontario

SUPERVISOR: Dr. Adrian Kitai

NUMBER OF PAGES: xv, 134

Abstract

Research in fluorescent solar concentrators (FSCs) commenced in mid-1970's to lower the cost of solar cells through the reduction of the required solar cell active area, and by incorporating them in-to buildings, thereby offsetting installation costs. In FSCs, light penetrates the top surface of a waveguide, is absorbed by the fluorescent material (FM) and is emitted at a longer wavelength that is then internally reflected towards edge solar cells. In this project, the use of cerium doped yttrium aluminum garnet (Ce:YAG) was explored as an FM, from which the optical transport of fluorescence must be enhanced towards solar cell edges.

Optical spectroscopic techniques were conducted to characterize a sample of Ce:YAG with a doping level of 0.180 mol%. An excitation and emission profile indicated a strong absorption at 476 nm and a strong radiation at 530 nm, where the fluorescence process lasted for only 62.3 ns, with a conversion efficiency of 80.0%. Meanwhile, x-ray analysis concluded that this material had a density of 4.56 g/cm^3.

An acrylic concentrator with local islands of Ce:YAG was successfully fabricated. A lens sheet was used to provide strong sunlight coupling to Ce:YAG. The concentrator was analysed using Optics Lab, Monte Carlo simulations (MCS) and through experimental flux measurements, the percentage of light that waveguided to the edges was determined. Optics Lab yielded 56.10%, MCS

yielded 59.20% and flux measurements resulted in 58.22% (without lenses) and 57.14% with lenses. Also, an overall experimental optical efficiency was determined to be 32.45% without lenses and 53.53% with lenses. These results can be improved by modifying the fabrication techniques and using substrates with higher refractive indices.

Acknowledgements

I would like to express my deepest gratitude and appreciation to my supervisor, Dr. Kitai, for always being approachable, and providing encouragement and guidance throughout the course of this project. I would also like to thank my colleagues for their support, helpful suggestions and assistance. Thanks to the staff at Brockhouse Institute for Materials Research and Centre of Emerging Device Technology for training me on several pieces of equipment, and their assistance with specific sample preparation techniques. I would also like to praise the department of Materials Science and Engineering for making the course of my graduate study as smooth as possible.

I would like to acknowledge NSERC Photovoltaic Innovation Network whose generous funding made this project possible. It was an honour to be a part of a network committed to strengthening the photovoltaic industry in Canada.

Finally, I would also like to express my deepest gratitude and appreciation to my friends and family, especially my parents for always keeping me grounded, and providing much needed support and motivation throughout my degree. I would like to dedicate this work to my parents.

Table of Contents

List of Figures

List of Tables

List of Abbreviations and Symbols

Abbreviations

DC = Down conversion

DS = Down shifting

EHP = Electron hole pairs

EQE = External quantum efficiency

FM = Fluorescent material

FQY = Fluorescent quantum yield

FSC = Fluorescent solar concentrator

IQE = Internal quantum efficiency

LED = Light emitting diodes

LSS = Luminescent spectral splitter

MCS = Monte Carlo simulation

OPS = Oxide polishing silica

PERL = Passivated emitter rear locally diffuse

QC = Quantum cutting

QD = Quantum dot

RE = Rare earth

TCSPC = Time correlated single photon counting

TIR = Total internal reflection

UV-Vis = Ultraviolet-Visible range

Elements

Al = Aluminum

As = Arsenide

Ce^{3+} = Cerium

Eu^{3+} = Europium

F = Fluoride

Ga = Gallium

Gd^{3+} = Gadolinium

Ge = Germanium

In = Indium

Li = Lithium

Nd^{3+} = Neodymium

O = Oxygen

P = Phosphide

Pr^{3+} = Praseodymium

Si/mc-Si = Silicon/multicrystalline Silicon

SiC = Silicon carbide

Y^{3+} = Yttrium

Yb^{3+} = Ytterbium

YAG = Yttrium aluminum garnet

Symbols

A = Area

c = Speed of light = 3.00×10^{8} m/s

C_{geom} = Geometric concentration

CS (λ) = CCD detector's spectral response

E = Energy

e_1 = Energy of excitation photon = $E_{excitation}$

e_2 = Energy of emitted photon = $E_{emission}$

E_g = Bandgap

eV = Electron volt

F (hkl) = Structure amplitude

G_{cyl} = Cylinder geometry

G_{sq} = Square geometry

h = Planck's constant = 6.63×10^{-34} m^2 kg/s

h_1 = Size of LED

h_2 = Size of reproduced image

$I_{Ce:YAG}$ = Spectral irradiance of Ce:YAG

I_{laser} = Spectral irradiance of the laser

I_o = Incident intensity

$I_{Spectral}$ = Spectral irradiance

k = Boltzmann constant = 8.62×10^{-5} eV/K

L = Length

m = Ratio between size of LED and image produced

n_1 = Refractive index of the medium

n_2 = Refractive index of substrate

N_A = Avogadro constant = 6.02×10^{23}/mol

Ø (hkl) = Radial angle of function

$Ø_{absorbed}$ = Photon flux of absorption

$Ø_{emitted}$ = Photon flux of emission

$Ø_{hkl}$ = radial function of angle

$Ø_{incident}$ = Photon flux

P_{TIR} = Probability of total internal reflection

R = Reflectance

R_s (λ) = Integrating sphere's response

S = Distance between lens and focal point

S_1 = Distance between LED and lens

T_0 = Ambient temperature = 298 K

V = Volume

W = Width

x = Path length for one reflection

α = Absorption coefficient

η_{abs} = Absorption efficiency

η_{FQY} = Fluorescent quantum efficiency

η_{FSC} = Fluorescent solar concentrator efficiency

η_{host} = Host efficiency

η_{opt} = Optical efficiency

$\eta_{overlap}$ = Strength of overlap

η_{PV} = Photovoltaic efficiency

η_{self} = Self-absorption efficiency

η_{stokes} = Stokes efficiency

η_{Therm} = Thermalization efficiency

η_{TIR} = Total internal reflection efficiency

θ_C = Critical angle

λ = Wavelength

ρ (x,y,z) = Electron density function

1 Introduction

1.1 Current Status of Photovoltaics

Solar energy is the most abundant energy source since there is essentially an infinite supply; however it only accounts for 0.004% [1] of global energy mainly due to high costs, low efficiencies and lack of economic energy storage systems [2]. Currently, the most prevalent commercial photovoltaic cell is made of single junction silicon devices. The passivated emitter rear locally diffuse (PERL) cell has reached an efficiency of about 26%, which is achieved by incorporating very pure silicon single crystal and light trapping techniques into the design [3]. In effect, research has gone into using different materials as well as thin film technologies to increase efficiency and reduce cost. Fluorescent Solar Concentrators (FSCs) began essentially as an alternative to lower the cost of solar cells [4]. FSCs consist of a transparent substrate, a luminescent or fluorescent material embedded in the substrate and solar cells that are attached at the edges [4], [5], [6]. They offer a cost reduction since the collecting face (the active solar cell area) is much smaller than in the traditional solar cell design [7]. Furthermore, the transparent substrate in FSCs permits them to be incorporated into buildings, therefore offsetting installation costs. Another significance of this design is that it allows for the concentration of light even under cloudy conditions.

Consequently, enhancing the optical transport within the waveguide towards the solar cells is one of the main objectives of FSCs' research [4], [6], [8].

1.2 History of Fluorescent Solar Concentrators

In 1973, Lerner from the Massachusetts Institute of Technology wrote a grant proposal for a device with similar working mechanisms as that of an FSC [6], [9]. However, this concept was not fully explored until 1975 by Lerner's graduate student. In 1976 [10], the idea of trapping light for solar concentrators was first conceived by Weber and Lambe who were working at Ford Research. They called it a "Luminescent Greenhouse Collector" [7], [9] [11]. The first efficiencies were reported to be 2.5% for a single dye system and 4% for a stacked FSC system [9], [12], using a Neodymium dye embedded in an extra-low dispersion glass and Rhodamine doped polymethacrylate [9].

Research in this field receded due to a decrease in oil prices in the early 1980's, but interest regenerated in the early 2000's with a team at Imperial College in London developing an FSC with an efficiency of 7.1% [6]. This accomplishment restored interest in FSCs since the previous reported efficiency was only 2.5% [6], [12], by using materials, such as rare earth metals, semiconducting polymers and quantum dots, that were not available 20-30 years ago [6], [13].

2 Literature Review

2.1 Device Design and Principles of Operation

Fluorescent Solar Concentrators consist of three parts: a transparent substrate, known as a waveguide, a fluorescent material embedded in the substrate and solar cells attached at the edges. It essentially works by light penetrating the top surface of the device, getting absorbed by the fluorescent material and being emitted at a different wavelength; refer to Figure 1 [6], [8], [13], [14].

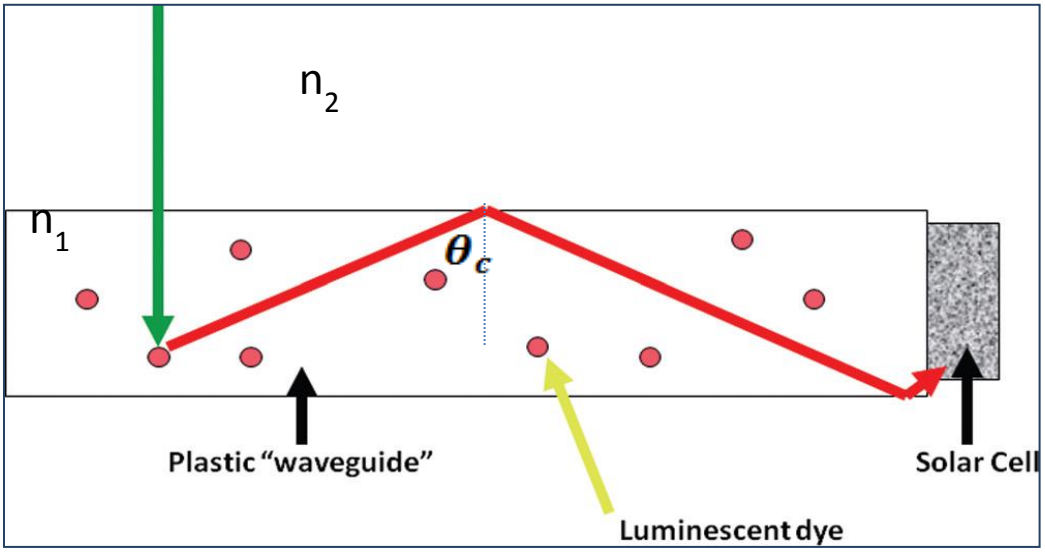

Figure 1: Principle operation of fluorescent solar concentrators. Green arrow represents incident light, red arrow emitted light from the photon, while n_1 and n_2 represent refractive indices of the substrate and medium (air), respectively [6].

A phenomenon known as total internal reflection (TIR), is observed in this device since the difference in the refractive indices at the interface between the

medium (e.g. air) and the substrate causes some of the light to be refracted out of the device while the remainder is internally trapped within the substrate [6], [9], [13]. Consequently, the 'trapped' light will be concentrated along the edges and waveguided towards the solar cells. Snell's Law (shown in Equation 1), determines the critical angle at which the light, emitted from the luminescent material, approaches the top surface [15]:

$$\theta_c = \sin^{-1}(\frac{n_2}{n_1})$$

Equation 1: Calculating critical angle, where n_1 and n_2 represent the refractive indices of the substrate and medium, respectively [15].

The critical angle determines the maximum amount of light that can be refracted out of the device through the escape cone fraction from the top and bottom surfaces. It is described by the following equation:

$$\frac{I_{escape}}{I_{source}} = \frac{1}{2}(1 - \cos\theta_c)$$

Equation 2: The escape cone fraction using the critical angle [7], [6].

which is derived in Appendix A.1: Escape Cone Fraction Derivation for a solar concentrator with a rectangular prism geometry.

2.2 Efficiency Limits FSCs

When using optics to concentrate light onto the concentrator, the factor of concentration is dependent on the geometric ratio between optics (e.g. lens or mirror) and the active solar cell area, using:

$$C_{geom} = \frac{optics\ area}{active\ cell\ area}$$

Equation 3: Geometric concentration of light in a concentrator [16].

There are nine different ways in which the "concentrated light" behaves in a solar concentrator, and are shown in Figure 2 below. The arrow labelled "1" symbolizes the incident photons on the top surface can be effectively absorbed by the fluorescent material in "2". The absorbed light may be reemitted at a different energy level depending on the material's fluorescent quantum yield (FQY), which is characterized by "3" and transported to the solar cell at the edge, as shown in "4". In "5", the incoming waveguided energy is converted to electricity by the solar cell [4], [6], [13], [19].

There are four main losses associated with fluorescent solar concentrators, which contribute to their low efficiencies. First, light maybe externally reflected before even entering the concentrator, as shown in "6". Alternatively, "7" illustrates that the fluorescent material maybe transparent to the incoming wavelengths and consequently exit the concentrator altogether. The final two fates of the emitted light may be due to refraction out of the device through the escape

cone fractions as shown in “8”, or “9” shows that the emitted light may be absorbed by an adjacent dye. Other loss mechanisms that are not exhibited in the figure below, have to do with the state the waveguide is in itself. Any imperfections or defects cause light to scatter or possibly parasitic absorption in the host matrix may also be observed [4], [6], [13], [19].

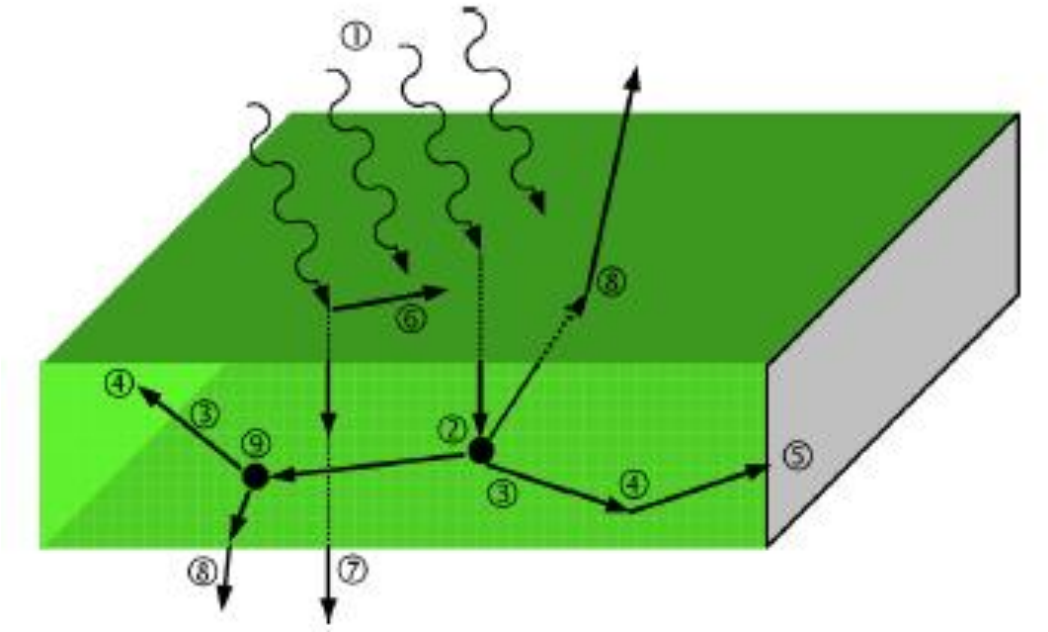

Figure 2: Cross-sectional diagram of an FSC, showing the 9 different loss mechanisms [13].

When taking into account the loss mechanisms mentioned above, the optical efficiency of the concentrator can be calculated through Equation 4,

$$\eta_{opt} = (1 - R)P_{TIR} \cdot \eta_{abs} \cdot \eta_{FQY} \cdot \eta_{stokes} \cdot \eta_{host} \cdot \eta_{TIR} \cdot (1 - \eta_{self})$$

Equation 4: Optical Efficiency. (1-R) represents transmission of light into the concentrator; P_{TIR} is the probability of fluorescence emission being trapped. η_{abs} is absorption efficiency of the fluorescent material of the incident light. η_{FQY} is the fluorescent quantum yield, which determines the probability that an excited fluorophore will decay by emission of fluorescence. The Stokes efficiency, η_{stokes}, is the fraction of energy remaining after fluorescence process. The host efficiency, η_{host}, is the fraction of transmission of emitted photons by the host (after absorption). The total internal reflection efficiency, η_{TIR}, accounts for any damages or foreign particles that cause light to scatter. Finally, (1- η_{self}), is the fraction of light reaching the edges without being lost to reabsorption [6], [13], [19].

where the overall FSC efficiency can be determined by:

$$\eta_{FSC} = \eta_{PV} \cdot \eta_{opt}$$

Equation 5: Overall efficiency of fluorescent solar concentrator, a product of the efficiency of the optical efficiency (η_{opt}) and photovoltaic efficiency (η_{PV}) which is the difference between incoming energy and that of the solar cells [19].

The efficiencies for these concentrators are typically low, with the highest being only 7.1%, which is mainly attributed to material challenges and device design constraints. Table 1 outlines some of the reported efficiencies for FSCs for some common materials.

Table 1: Reported efficiencies of fluorescent solar concentrators [6].

Luminophore	Cell Type (# of Edges)	FSC Size (cm)	Efficiency (%)
CdSe/CdS QD	Si (1)	5x5x0.3	2.1
Red 305/CRS040	mc-Si (1)	5x5x0.5	2.7
Coumarin, Rhodamine	Si (1)	140x140x3	3.2
Red 305	Si (1)	5x5x0.3	3.3
CdSe/CdS QDs	GaAs (1)	140x140x3	4.5
Red 305/CRS040	GaAs (1)	5x5x0.5	4.6
Red 305/CRS040	GaAs (4)	5x5x0.5	7.1

2.3 Recent Research

Research in fluorescent solar concentrators was renewed after being dormant for nearly two decades. This was a result of increased interest in green alternative energy because of escalated environmental concerns, in addition to declining fossil fuel reserves. The advances in technology and discovery of materials that were not available twenty years ago, such as rare earth metal and quantum dots, has made it possible to explore different options for FSCs. Recently, research has also gone into using alternative designs for FSCs, instead of traditional rectangular prism geometry to enhance the optical transport of light through the device [14], [20].

2.3.1 Materials Challenges

Table 2 outlines five main criteria that the ideal fluorescent material must satisfy. This material is designed for a solar cell with a bandgap of E_g.

Table 2: Ideal properties of a fluorescent material for a concentrator [13], [21].

Desired Property	**Organic**	**Inorganic**	**Hybrid**
Absorb all photons $E \geq E_g$ and emit at $E \approx E_g$	X	$\surd^{\pm}$ / X^{+}	√
Exhibit minimal reabsorption losses	X	$\surd^{+}$ / $X^{\pm}$	√
Quantum efficiency close to 100%	√	$\surd^{+}$ / $X^{\pm}$	√
Environmentally stable for at least 20 years	$\surd^{*}$	$\surd^{+}$ / $X^{\pm}$	√
Produced at low costs	$\surd^{*}$	$\surd^{+}$ / $X^{\pm}$	√

Several different types of materials have been investigated, both organic and inorganic, as indicated in Table 2. However, before discussing the limitations of these materials, the concept of Stokes shift has to be addressed, since it is a determinant of the extent of reabsorption losses exhibited in FSCs and is shown in Figure 3.

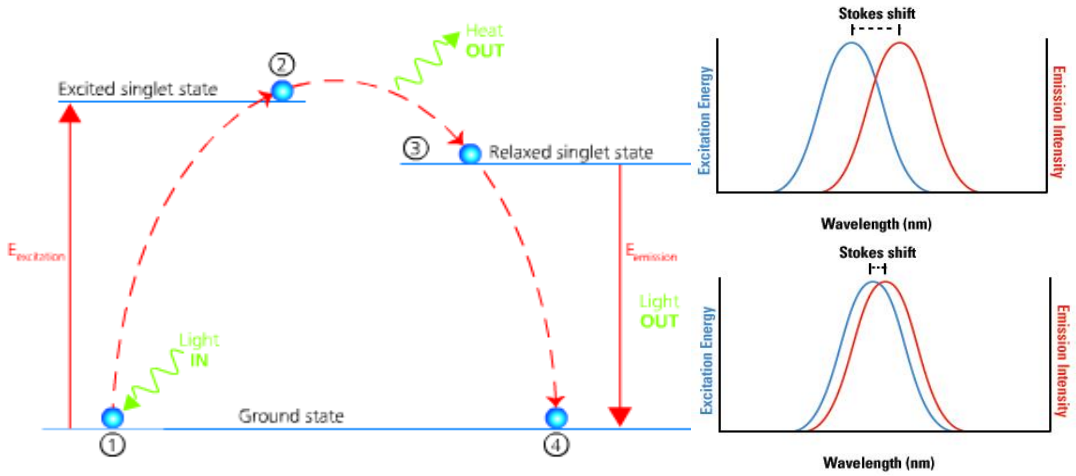

Figure 3: Schematic of Stokes shift [22].

When the fluorescent material absorbs photons of energy, $E_{excitation}$, electrons jump to the 'excited singlet state' in (2) from the ground state (1) and remain there for nanoseconds. The fluorophore undergoes internal structural change and releases some energy in the form of heat, during the process. This causes the electrons to transfer to a different orbital of a more stable energy level known as the 'relaxed singlet state' in (3). After some time, electrons fall back down to their original ground state in (4), and in doing so, energy is released in the form of fluorescence, $E_{emission}$. The difference between $E_{excitation}$ and $E_{emission}$ is known as Stokes shift. This difference needs to be small enough to minimize energy losses (the heat generated as a result of the transition from one orbital to another), but also large enough to minimize reabsorption losses through the reduction of the overlap between the excitation and emission spectra [22], [23].

Initially, organic dyes were investigated since they were more readily available than inorganic materials, more specifically, Rhodamines, Coumarins and perylene derivatives are the most commonly used dyes in FSCs. Rhodamines have high quantum yield values and high molar extinction coefficients, but small Stokes shifts that lead to increased reabsorption losses and consequently increased FSC losses. Coumarins on the other hand, display larger Stokes shift than Rhodamines, and high quantum yield and reduced photostability in comparison to perylene-based dyes. Perylenes have intense fluorescence, decent photostability, and low solubility, which can be improved by adding ortho-alkylated aromatic groups. A main disadvantage of using organic dyes is that they have limited spectral absorption range. The molecular structure of those organic dyes is shown in Figure 4 [6], [24].

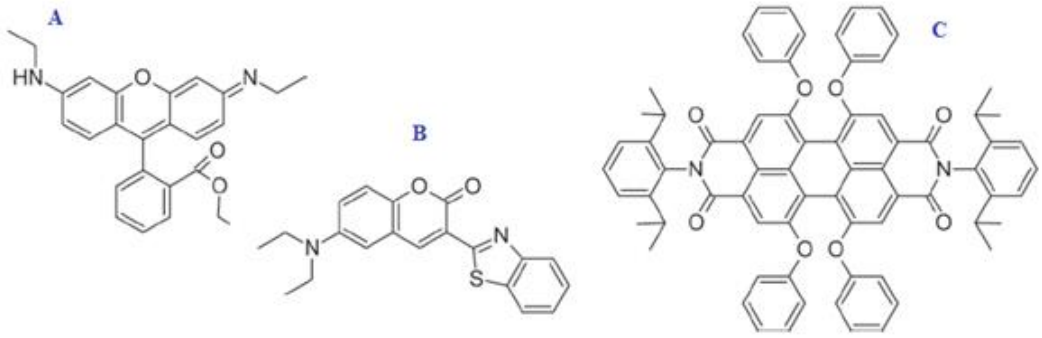

Figure 4: Examples of organic dyes used in FSCs, A) Rhodamine 6G, B) Coumarin and C) Perylene Bismide [6].

With regards to inorganic materials, rare earth (RE) ions such as Nd^{3+} and Yb^{3+}, and quantum dots (QDs) (mainly indium phosphide, zinc sulphide or

cadmium selenide) are investigated as viable fluorescent materials. REs have good photostability and large enough Stokes shift; however, they have low absorption efficiency. This in turn requires very high concentrations of these ions to yield high efficiency, and consequently, leads to very high costs. Quantum dots have a distinct advantage over other materials since their band gaps can be tuned according to their size. Increasing their diameter decreases their E_g. They also have good photostability when encapsulated in a matrix; otherwise, they are sensitive to oxygen, light and are very toxic in nature [6], [13], [25].

Table 2 compares organic and inorganic materials and the "ideal properties" they satisfy. As can be seen, neither fulfils all the requirements. However, it was predicted that a hybrid material would, but this has not been tested yet since its feasibility is yet to be determined [13].

2.3.2 Device Design

In addition to exploring different materials, research is targeted towards enhancing the optical transport of emitted photons towards the solar cells. One way of doing this is through using a Luminescent Spectral Splitter (LSS), shown in Figure 5. This design uses sheets containing different dyes tuned to different bandgaps, which are separated by air gaps to prevent optical coupling. This allows for maximizing the use of the solar spectrum, in addition to recovering escape cone losses. The disadvantage of LSS is the high costs associated with increased solar cell area and higher assembly costs [6], [26].

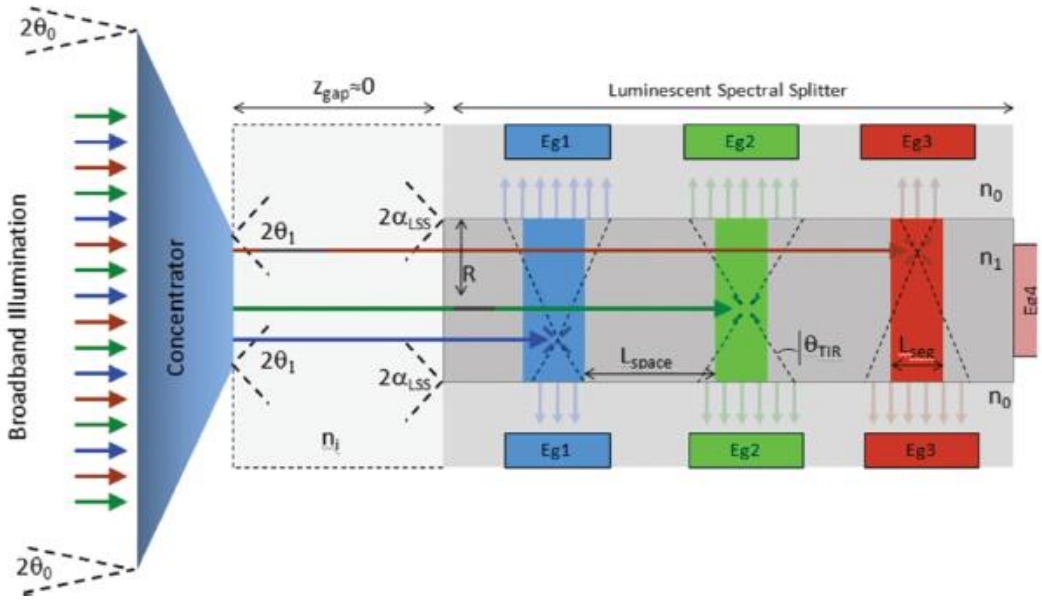

Figure 5: Luminescent Spectral Splitter [26].

Another way to ensure the maximum amount of light reaching the edges is through using a cylindrical (both single and multi-cylinder) configuration, instead of the traditional square planar design. McIntosh, Yamada, and Richards theoretically compared the loss mechanisms for those geometries in 2007, in addition to the implication of their optical concentrations. It was found that the cylindrical design offers an optical concentration of 1 to 1.9 times the equivalent area of a square design [7]. The geometric ratio for a cylinder with respect to a square is derived as:

$$G_{cyl} = \frac{L}{2W} = 2G_{sq}$$

Equation 6: Geometrical concentration relationship between cylindrical and square FSC [7].

where a full derivation of Equation 6 is found in Appendix A.2: Geometric Ratio for Cylindrical Design.

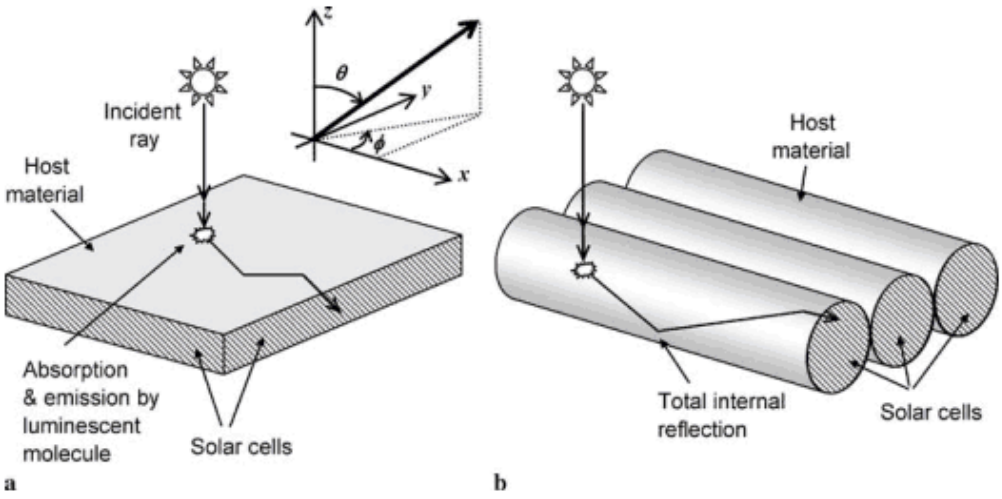

Figure 6: Incident ray travelling through a) planar FSC, and b) a multi cylindrical FSC [7].

McIntosh et al., found that less light was externally reflected for multi-cylinder design than either the flat plane or a single cylinder, whereas escape cone fraction yielded approximately the same or larger amount of light escaping the cylindrical concentrator compared to the planar one. The details for those results can be found in their published paper [7]. In 2011, Professor Ghosh and his students at the University of California, Merced, made cylindrical and hollow cylinder solar concentrators. Their experimental values yielded that the concentration effect was only marginally better for the cylindrical design, and consequently, resulted in similar efficiencies. The hollow cylinder on the other

hand, absorbed 20% – 30% more light, had lower reabsorption losses and 55% more of emitted light transported to edges than the solid cylinder. This resulted in an optical efficiency of 53%, while only 43% and 31% for a solid cylinder and square FSC, respectively [27].

3 Research Objectives

3.1 Motivation

Currently, the highest record photovoltaic solar cell efficiency is 44.7%, for a triple junction concentrator cell made of three subcells, where each is tuned to different spectral ranges to maximize the utilization of the entire solar spectrum, as shown in Figure 7. Due to the high cost of the materials used for these subcells (GaInP, GaInAs and Ge), this multijunction cell is generally reserved specifically for space applications [28], [29]. Meanwhile, silicon solar cells remain the most commercially available cells with the highest reported efficiency of 27.6% [30], [31].

When analysing the conversion efficiencies of the Silicon and GaInP subcell for wavelengths less than 500 nm, there are significant thermalization losses shown in light blue and grey in Figure 7 and Figure 8, respectively. The thermalization losses can be calculated by assuming a photon of incoming light at 500 nm is absorbed and thermalized in silicon. It would have a maximum useable energy equal to the bandgap of silicon or 1.10 eV. If GaInP absorbed the same photon, it would have a maximum useable energy of 1.70 eV. Calculating the percentage losses for each type of cell results in higher thermalization losses in silicon compared to GaInP [29], [31].

With respect to concentrators, more work was conducted for converting the low energy photons to a specific bandgap, typically one matching that of gallium arsenide or silicon. This research, however, the concept of a solar concentrator is employed so that the fluorescent material efficiently absorbs all high-energy photons and emits them at wavelengths that can be effectively utilized by either of the solar cells mentioned above. This will essentially improve the conversion efficiency of the smaller wavelengths and therefore lead to an increase in the overall efficiency of the cell.

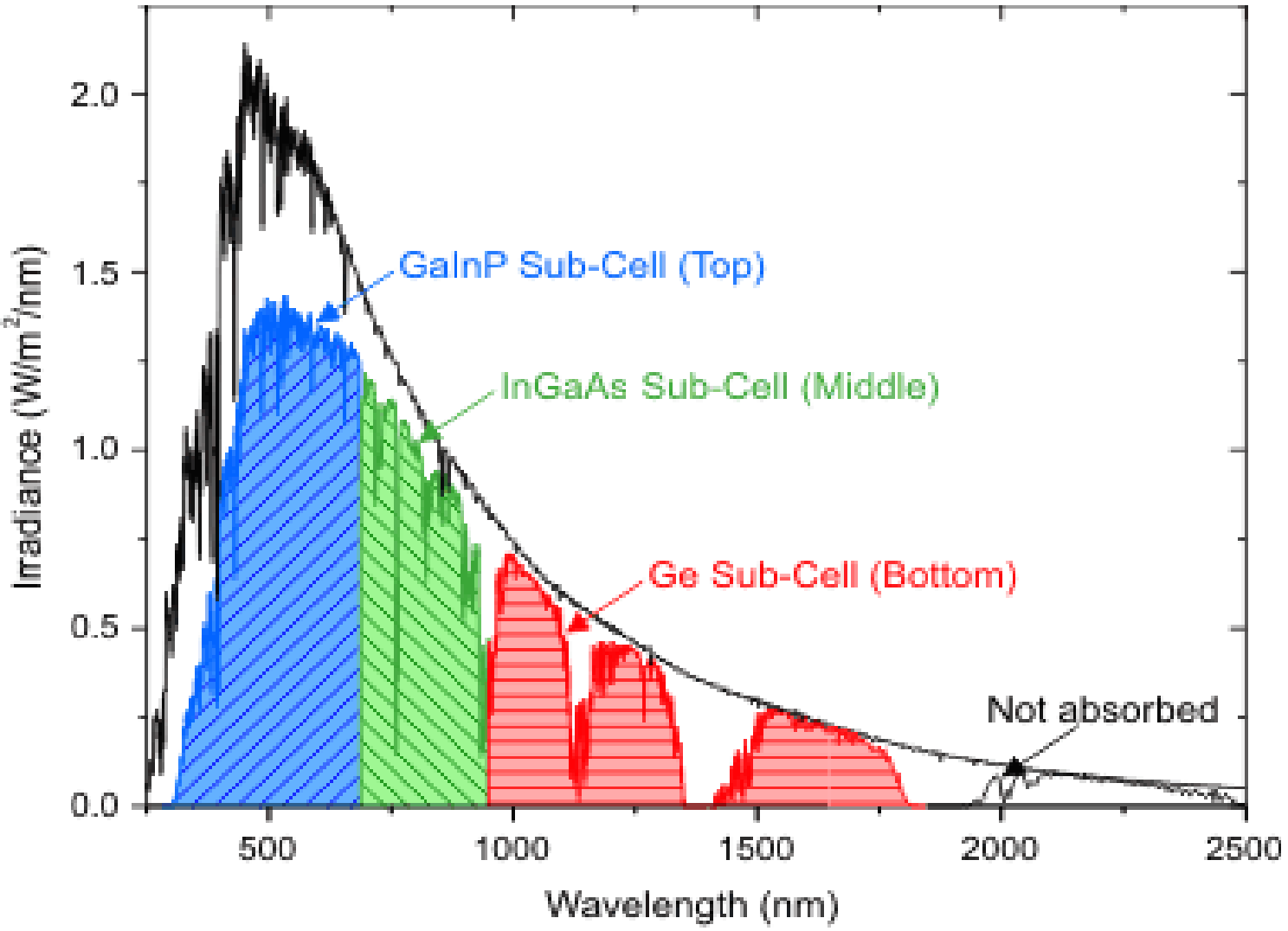

Figure 7: Multijunction solar cell showing the portions of the spectrum covered by each material [29].

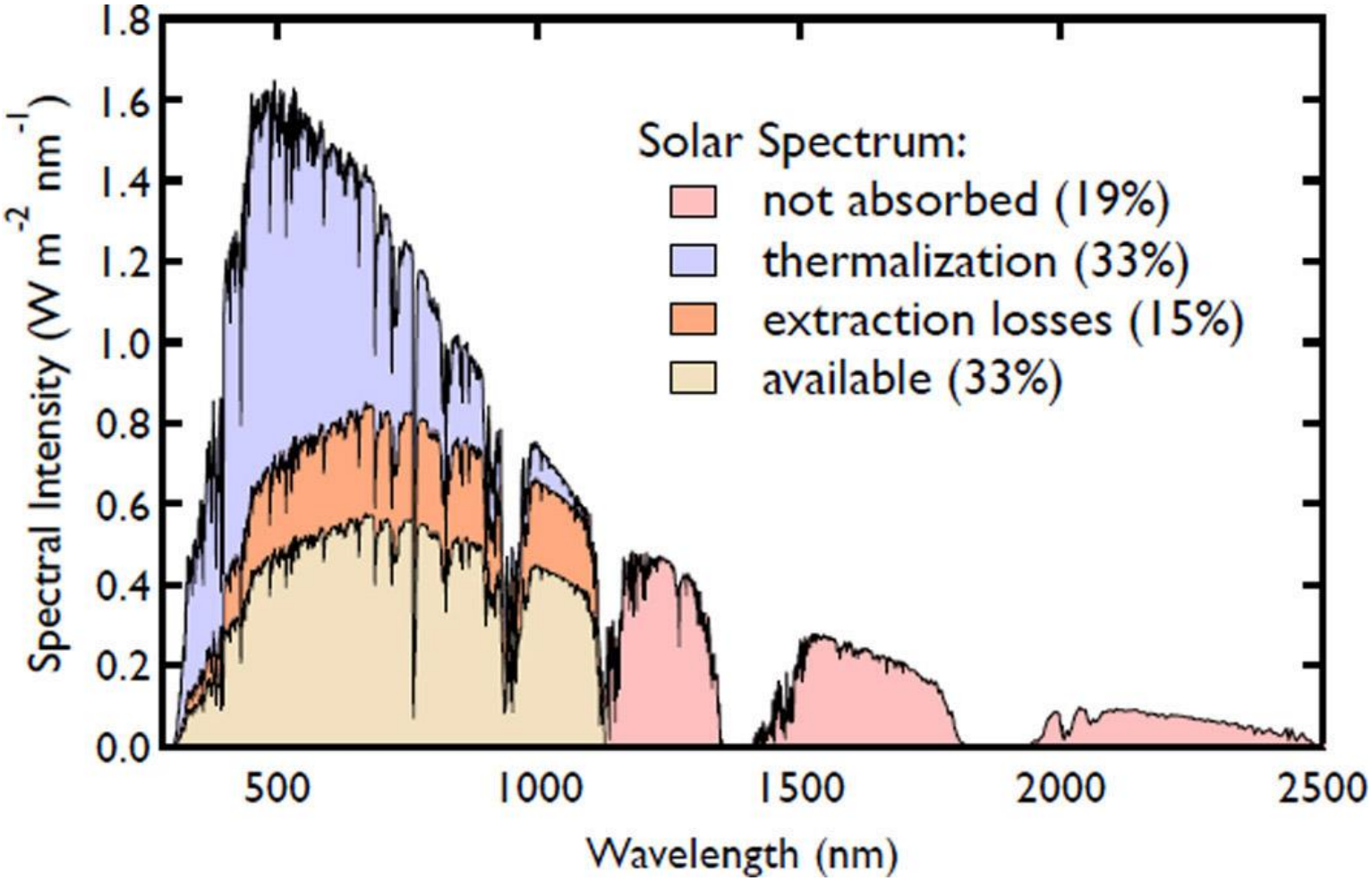

Figure 8: Conversion efficiency of silicon solar cell [32].

3.2 Material Selection

There are two types of materials that absorb light at a specific energy level and emit at a lower one: down conversion (DC) and downshifting (DS) materials. In the case of down conversion, a high-energy photon ($2E_g$) is absorbed and two photons of lower energy, typically with $E = E_g$ are emitted [33]. There are three different processes that can cause the emission of two photons in a material, i.e. achieve down conversion: quantum cutting (QC) using host material, QC on single rare-earth ions and DC using rare-earth ions pairs [34].

In the first mechanism, an interband Auger effect is observed for an incoming energy $\geq 2E_g$. An electron is excited deep into the conduction band from the valence band, and the excess energy excites a second electron to the conduction band, thereby generating two electron-hole pairs (EHP). These EHP combine at luminescent centres and emit two photons each with $E = E_g$, as illustrated in Figure 9. This mechanism is observed mainly in nanocrystals (e.g. Si nanocrystals).

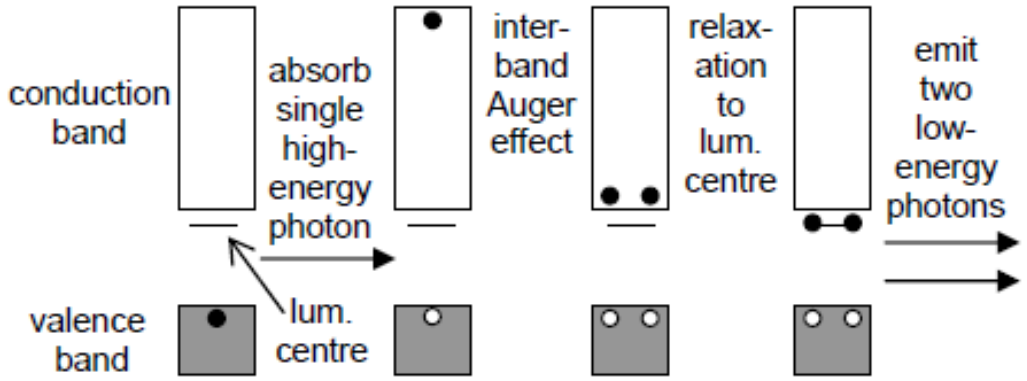

Figure 9: Interband Auger mechanism for the generation of two-photons from each high-energy incident photon [34].

For QC in single RE ions, absorption of light occurs via the host lattice and transfers to an electron causing a *4f-5d*, transition in the rare earth ion and subsequently one photon is emitted. When the electron relaxes back to the ground state, a second photon is emitted. An example of a material that exhibits this behaviour is praseodymium doped yttrium fluoride (Pr^{3+}:YF_3), which was first studied back in the mid 1970's [34], [35]. Not entirely dissimilar to the third mechanism, is down-conversion using rare-earth ions pairs, where in this case, energy is transferred to a neighbouring ion by cross-relaxation. Figure 10 depicts the down-conversion mechanisms for rare-earth ions. Figure 10: (a) shows the two photon emission within one ion, whereas Figure 10: (b)-(d) emphasizes the energy transfer between two ions A and B. In gadolinium lithium fluoride doped with europium ($LiGdF_4$:Eu^{3+}), Gd^{3+} is first excited, part of the energy is transferred to Eu^{3+} by cross relaxation, while the remaining energy is transferred

to a neighbouring Eu^{3+} by energy transfer (as illustrated in Figure 10 (b)) [34], [36], [37], [38].

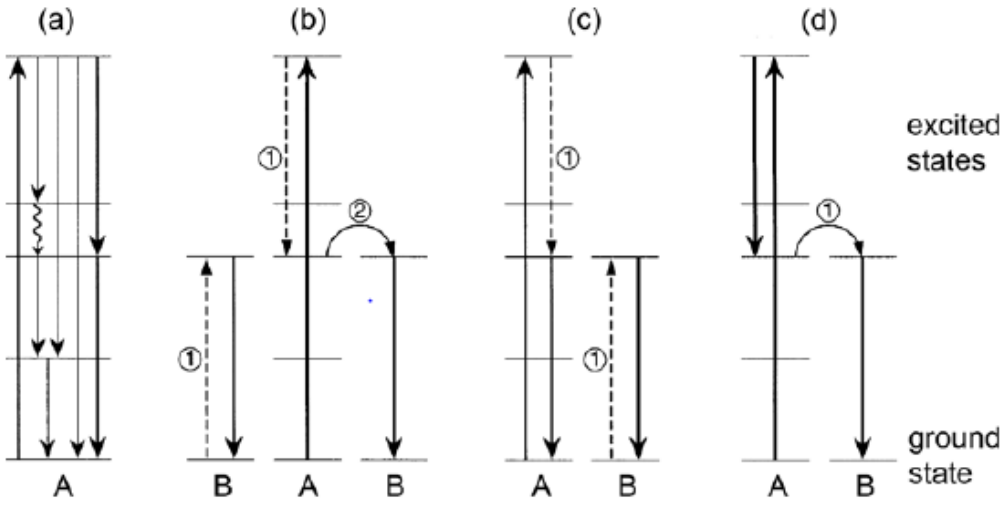

Figure 10: Quantum cutting mechanisms for rare earth ions: (a) two photon emission from a single ion, (b) cross-relaxation from ion A to ion B (1) and energy transfer from ion A to ion B (2) with emission from ion B, (c) and (d) cross-relaxation followed by emission from ions A and B [34].

On the other hand, when a downshifting material absorbs energy of E_g, only one photon with $E < E_g$ is released. Since the law of conservation of energy must be maintained, this undoubtedly indicates that some thermalization losses occur within the material first before light is emitted. This occurs in the form of Stokes Shift, where electrons transition to a different orbital first, releasing some heat after excitation, remain at that specific state for fractions of a second, and finally relax back down to the ground state (refer to section 2.3.1: Materials Challenges: Stokes Shift) [33], [39]. The difference between the down conversion and down

shifting materials is illustrated in Figure 11. Generally, achieving DC is very rare and hard to find; most luminescent materials undergo the down shifting process.

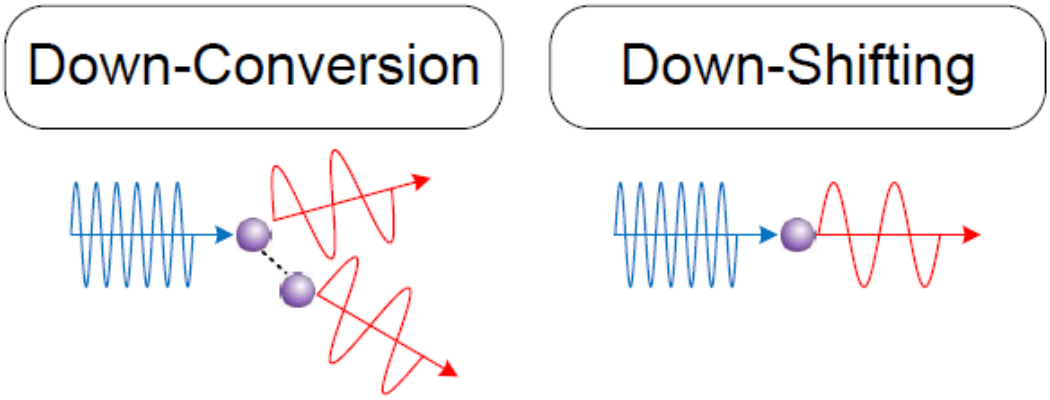

Figure 11: Illustration showing the downshifting and down conversion process. The high-frequency waves (blue) represent high-energy photons, and the low-frequency waves (red) represent low-energy photons [39].

For the purpose of this research, the requirements outlined in Table 2 were used to determine what fluorescent material should be selected. Yttrium Aluminum Garnet doped with Cerium [$(Y_{3-x}:Ce_x)Al_5O_{12}$ or Ce:YAG] was chosen since it satisfies most of those criteria. In this material, electrons transition from a 5d to a 4f sublevel in the Ce^{3+} atom, which causes the light released, when electrons relax back to ground state, to be emitted at a lower energy level than that absorbed, therefore making it a downshifting material [40]. Although some energy is lost to heat during this transition, the overall advantages of using this material outweigh its disadvantages.

Ce:YAG is currently used in light emitting diodes (LEDs) to generate yellow light from the blue light produced by indium gallium nitride, where the combination of the emitted yellow light with the non-converted blue light results in bright white light [41]. A theoretical excitation and emission profile is shown below in Figure 12. Since the peak, excitation and emission are approximately 450 nm and 550 nm, the Stokes Shift for this material is 100 nm. As can be observed, the overlap between the two spectra appears to be minimal, therefore indicating the minimization of reabsorption losses [40], [41], [42], [43]. Also, despite the fact that there is a region in the excitation spectrum that is not absorbed at all, this material does cover a good portion of the wavelength range up to 550 nm.

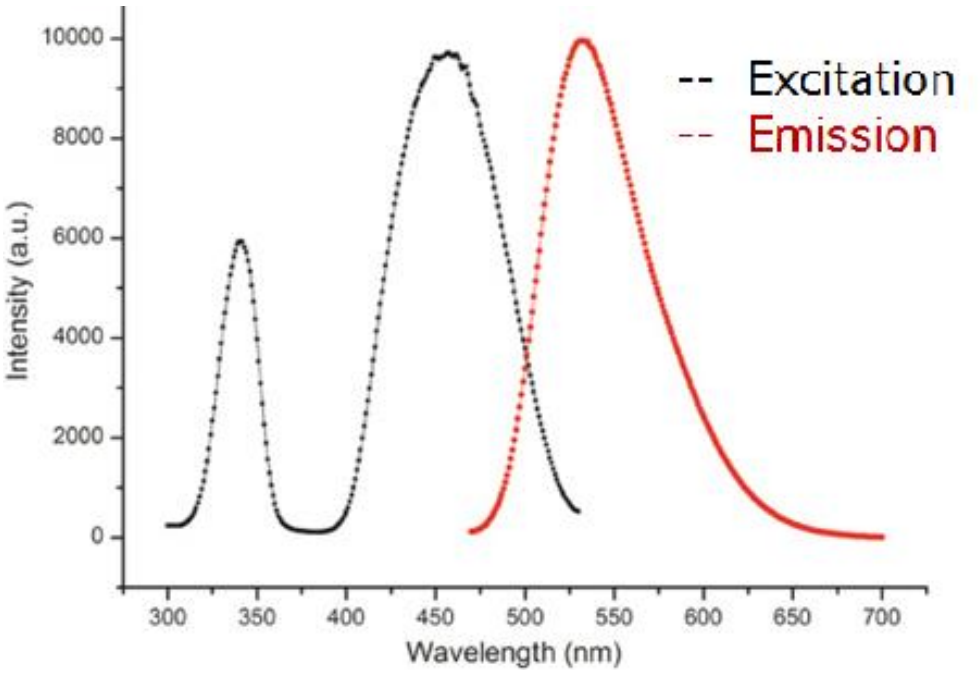

Figure 12: Theoretical excitation and emission spectra of Ce:YAG [40].

The use of Ce:YAG in light emitting diodes (LEDs) requires it to be highly stable and maintain its quantum efficiency under high temperatures. In 2007, Mesli conducted photodegredation tests on the different types of phosphors to determine which phosphor would behave most ideally for LED applications. Ce:YAG was found to be superior. Figure 13 shows that even under elevated temperatures, the quantum yield of Ce:YAG remains very high [44], [45]. This behaviour is indicative of its stability when subjected to extra amounts of energy (i.e. under sunlight concentration effect). When this material is embedded in the transparent substrate, it needs to be able to absorb all photons without degrading.

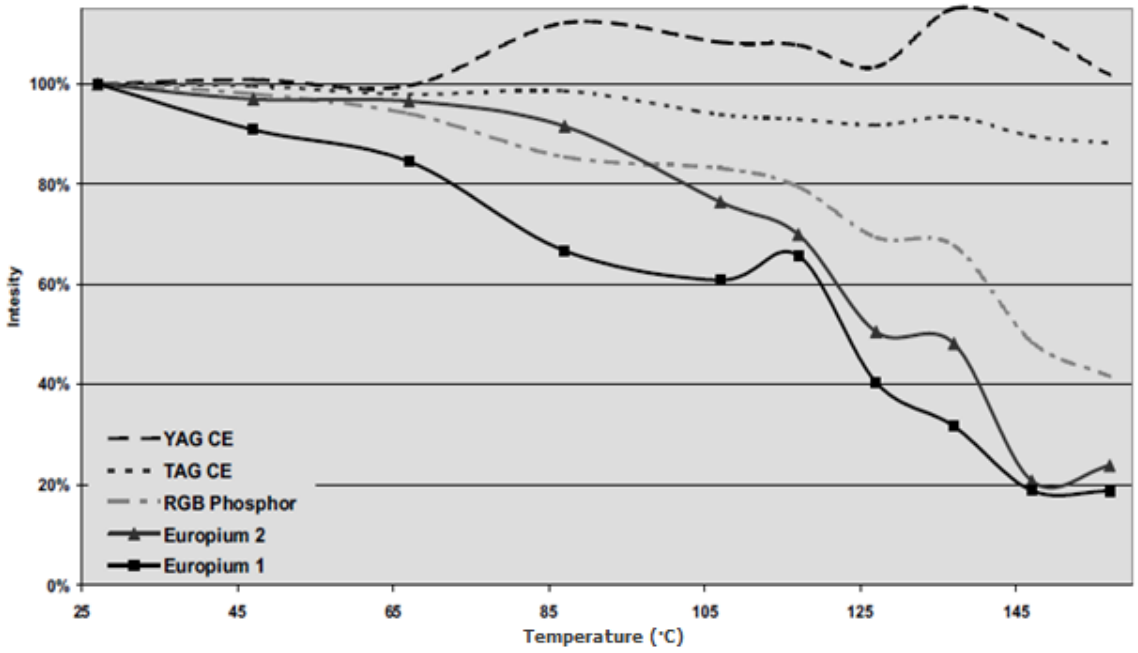

Figure 13: Phosphor's luminescence vs. temperature [44].

3.3 Goals

To improve the conversion efficiency, two specific goals must be accomplished. First, Ce:YAG must be characterized to confirm its fluorescent properties, and to determine its suitability specifically for solar cell applications. Next, since some losses are attributed to the nature of the waveguide, as explained in section 2.2, it is of the utmost importance to enhance the optical transport of the emitted photons to the edge-solar cells, to ensure a maximized optical efficiency, and consequently, an increase in the overall efficiency of the concentrator.

4 Approach

4.1 Characterizing Ce:YAG

As one of the main goals of this project is to characterize Ce:YAG to determine its candidacy as a viable FM, specific techniques are used to analyse its properties such as X-ray and photoluminescent measurements. The subsequent sections explain what each method is and how it was used to accomplish the pre-set goal.

4.1.1 Physical and Chemical Characterization

Set Up

X-ray analysis is a non-destructive technique mainly used to determine the nature of the material in question such as the crystal structure, lattice spacing, and preferred orientation. In this method, essentially a beam of x-ray interacts with the sample as it rotates along an incremental 2θ angle range. The diffracted rays are collected and produce constructive interference when Bragg's Law is satisfied, which states

$$n\lambda = 2d\ \sin\theta$$

Equation 7: Bragg's Law, where n is an integer, λ is the wavelength of incident ray, d interlattice spacing and θ is the angle of incidence.

This analysis was used to compare between YAG and Ce:YAG to determine whether or not cerium had any effect on the structural properties and inherent characteristics of the material. X-ray analysis was also used to detect the presence of phases in the powder sample to quantify the purity of the material. Any impurities or anomalies may have a significant impact on the optical properties of this material.

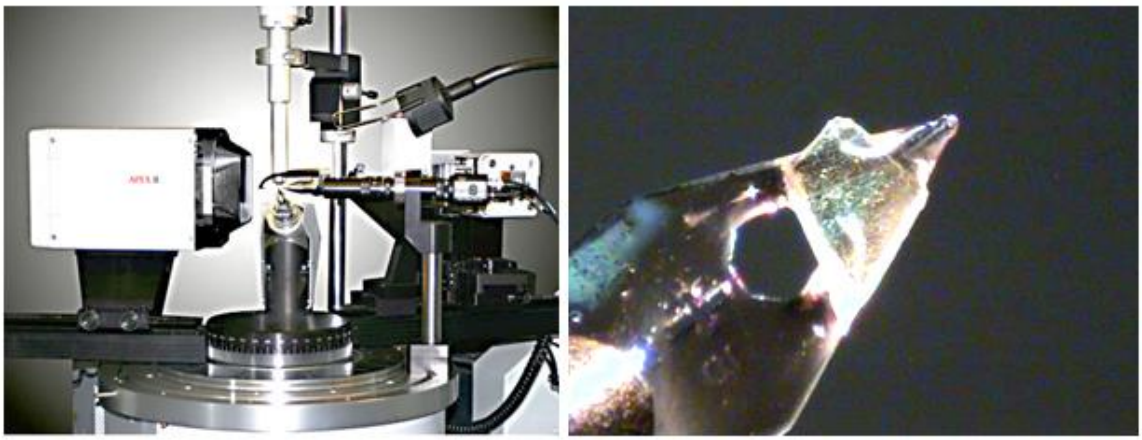

Figure 14: Diffractometer used for single crystal analysis (left) and the mounted 500 µm sized-single crystal (using oil) on the goniometer (instrument used to rotate the sample) on the right.

First, a single crystal analysis was used to solve and refine the crystalline structure of Ce:YAG and was used to compare with YAG's published results. To solve the crystal structure, the electron density function was calculated using the diffraction pattern obtained through

$$\rho(x,y,z) = \frac{1}{V}\sum_{h}\sum_{k}\sum_{l}\left|F(hkl)\right|\cos\left[exp\left[2\pi\left(hx_j + ky_j + lz_j\right)\right] - \emptyset(hkl)\right]$$

Equation 8: Electron density function, where V is volume, F(hkl) is the structure amplitude and Ø(hkl) is the radial angle of function.

where the summation is over all values of h, k, l and the volume of the unit cell. Since the diffraction attained was of the whole crystal, the calculation was therefore averaged over the volume of the whole crystal. This equation essentially yields electron density maps in which the maxima correspond to the positioning of an atom in the cell [46].

Next, a phase analysis was conducted on the powder samples to compare the positioning of the peak intensities occurring in both YAG and Ce:YAG. A different machine was used for this analysis, which is shown in Figure 15. A copper x-ray source was used instead of a molybdenum one, for this experiment. In this machine, when Bragg's Law is satisfied, and a peak intensity is detected, the signal is processed and is converted into a count rate, which is then outputted to a computer for further analysis.

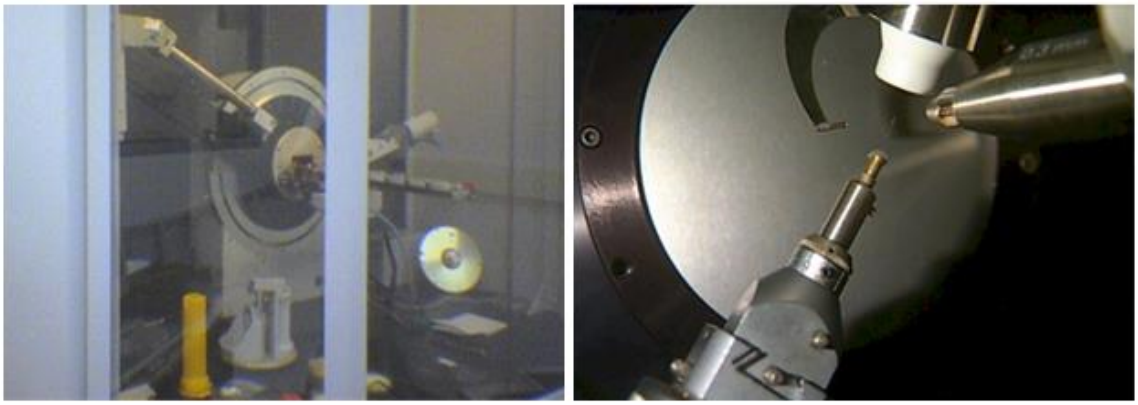

Figure 15: X-ray machine used for phase analysis (left), powder sample mounted on the goniometer (right).

Results

Single crystal x-ray analysis resulted in a body-cantered cubic crystal structure for Ce:YAG. More specifically, this material belongs to '$Ia\bar{3}d$' space group. Figure 16 shows the diffraction pattern observed specifically on the (211) and (400) planes. These two examples confirm the presence of the 3-fold axis. The angles of the unit cell were 90º as expected, with a lattice constant of 12.004 Å, density of 4.56 g/cm^3 and orientation of <111>.

The phase analysis results are shown in Figure 17 below, where both Ce:YAG and YAG are plotted for comparison. As can be observed, both samples yield intensity peaks at the exact same two-theta angle, which implies the lack of additional phases present in either sample. Therefore both samples contain the same phases. The only difference between the two is that the presence of the cerium atoms causes the Ce:YAG results to shift to higher intensity values

relative to the YAG (the baseline for Ce:YAG is at a much higher intensity counts compared to YAG).

It can be concluded that since both the single crystal and phase analysis show that Ce:YAG results coincide with non-doped YAG, the presence of 0.180 mol% of cerium does not change the structure of YAG. This is because cerium enters the YAG structure as a substitutional defect on the yttrium site. In addition, the lack of additional phases indicates a very pure, high-quality sample, which is essential since any anomalies in the results could substantially alter this material's optical properties.

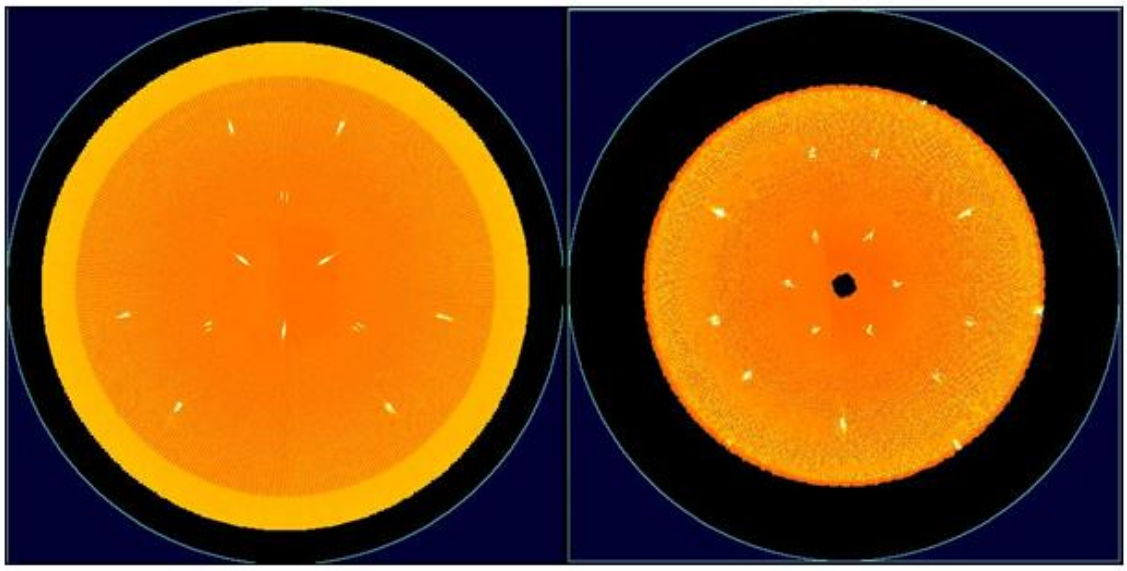

Figure 16: Single crystal x-ray analysis results.

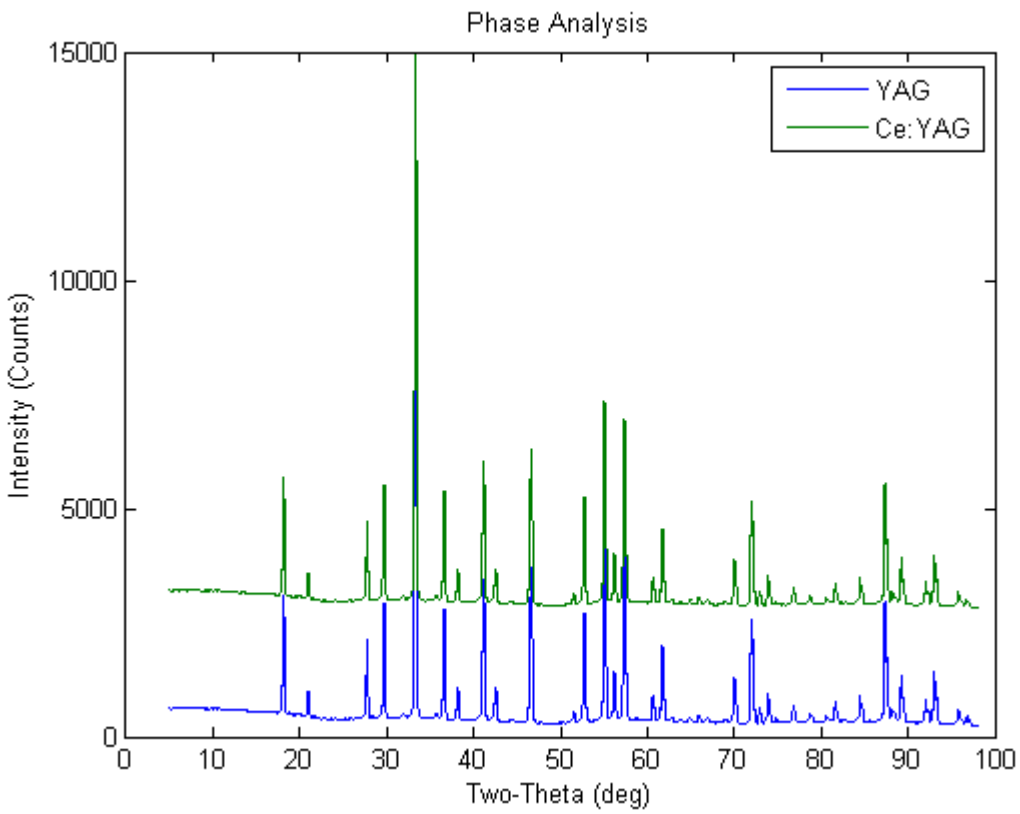

Figure 17: Phase analysis of YAG and Ce:YAG.

4.1.2 Optical Characterization

To optically characterize a cubic sample of single crystal Ce:YAG with dimensions of 0.926x0.924x0.214 cm, a number of instruments have been used throughout the course of this project: Varian Cary Spectrophotometer, Time Correlated Single Photon Counting system (TCSPC), USB2000+ Miniature Fiber Optic Spectrometer and a photometer. Although each instrument was used for a very specific reason, their essential working principal remains very much the same, which is outlined in Figure 18 below. The spectrophotometer was used to

obtain Ce:YAG's excitation, emission and transmission profile for all wavelengths, however it lacked the means to detect the fluorescence lifetime since it had a very large fall time light pulse (~µsec range). As a result, TCSPC was used for measurements that required very fast response time (~nanosecond range). The Optic Spectrometer was used to control the wavelength range of the excitation source to isolate only blue light. Finally, the photometer was needed to measure the luminance out of the edge and bottom surfaces (i.e. amount of light that gets waveguided and refracted out of the bottom surface).

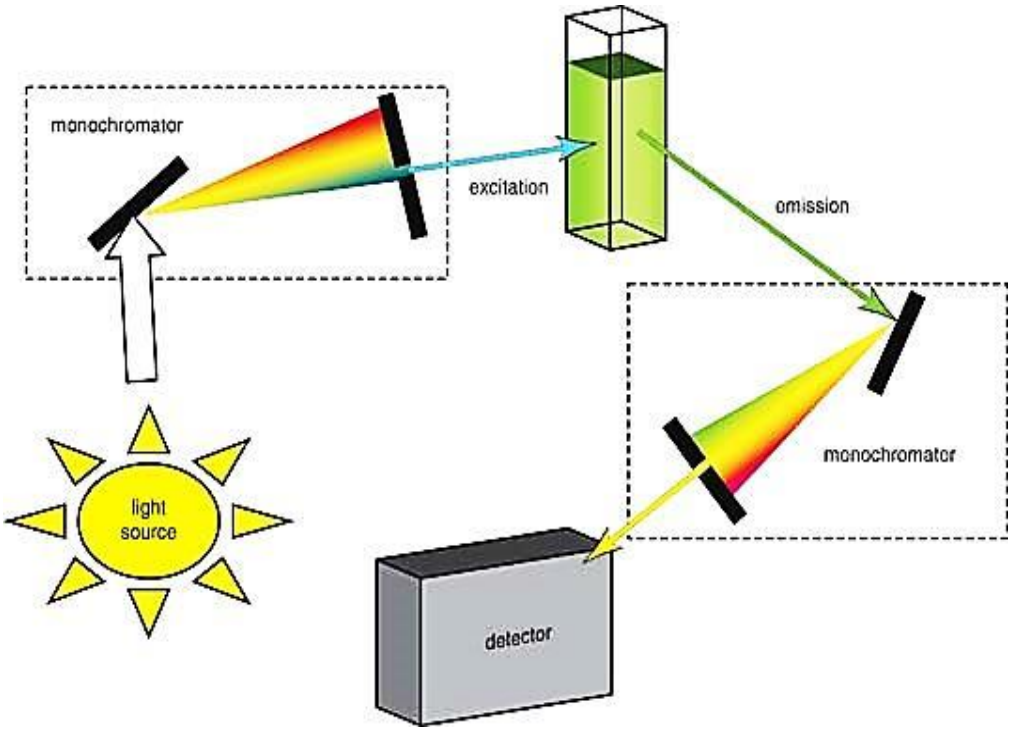

Figure 18: Photoluminescence measurements setup [47].

4.1.2.1 Varian Cary Spectrophotometer

Set Up

To determine how light interacts with a sample of Ce:YAG, two types of Varian Cary Spectrophotometer were used to conduct this measurements. UV-Vis Cary 50 Spectrophotometer measured the transmission of light (for all wavelengths) through the sample, while a Cary 50 Fluorescence Spectrophotometer was utilized to determine the excitation and emission profile of Ce:YAG. They both have the exact same operating procedure, but the first machine does not have the capability to detect fluorescence. An example of what either instrument looks like in working condition is shown in Figure 19.

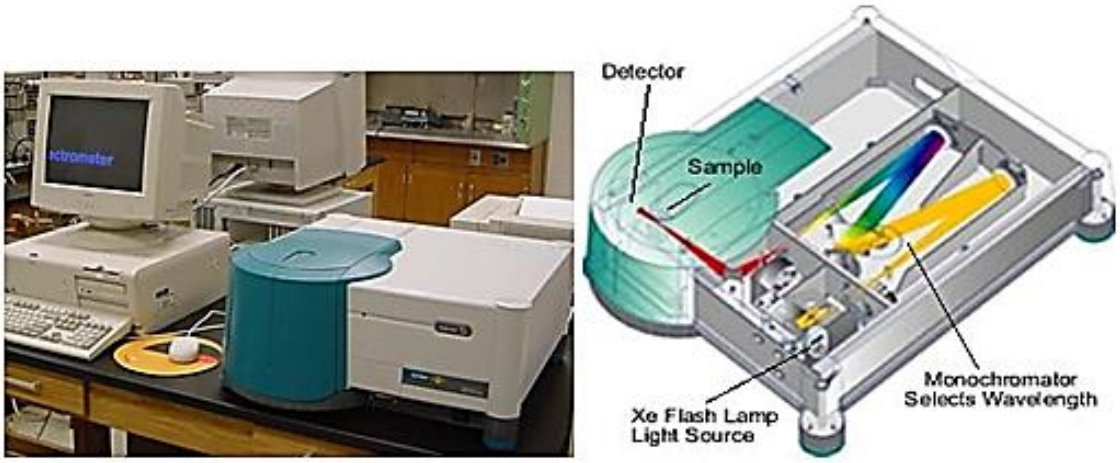

Figure 19: Varian Cary Spectrophotometer.

The spectral range was set to detect between 300 – 1100 nm, with a peak excitation at 465 nm, a peak emission at 550 nm and a slit bandwidth was set to 2.00 nm.

Results

Using a Cary Eclipse Fluorescence Spectrophotometer, the excitation and emission profiles were obtained. Figure 20 shows a peak excitation at 476 nm, and a peak emission at 530 nm.

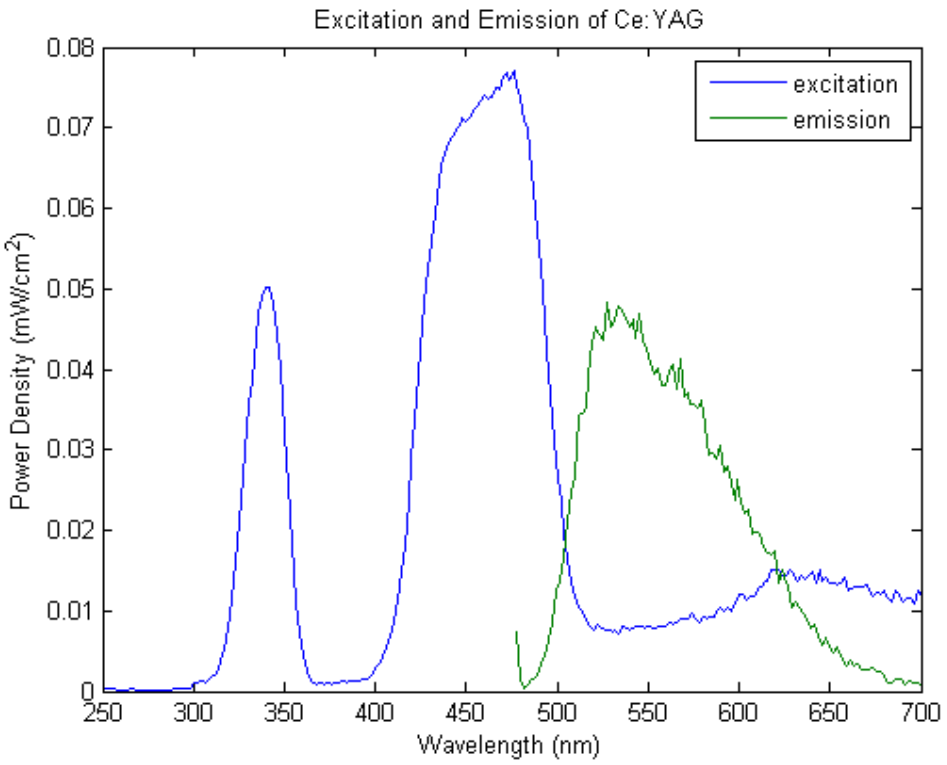

Figure 20: Experimental result of excitation and emission of Ce:YAG.

The transmission profile is shown in Figure 21, which – as expected - is the mirror image of the absorption profile shown in Figure 20. With the previous measurements, the results were obtained in power density, whereas the latter measurement was conducted to get the amount of light that was transmitted on a percentage basis (a UV-Vis Cary 50 Spectrophotometer was required) so that the absorption coefficient for a given wavelength can be determined.

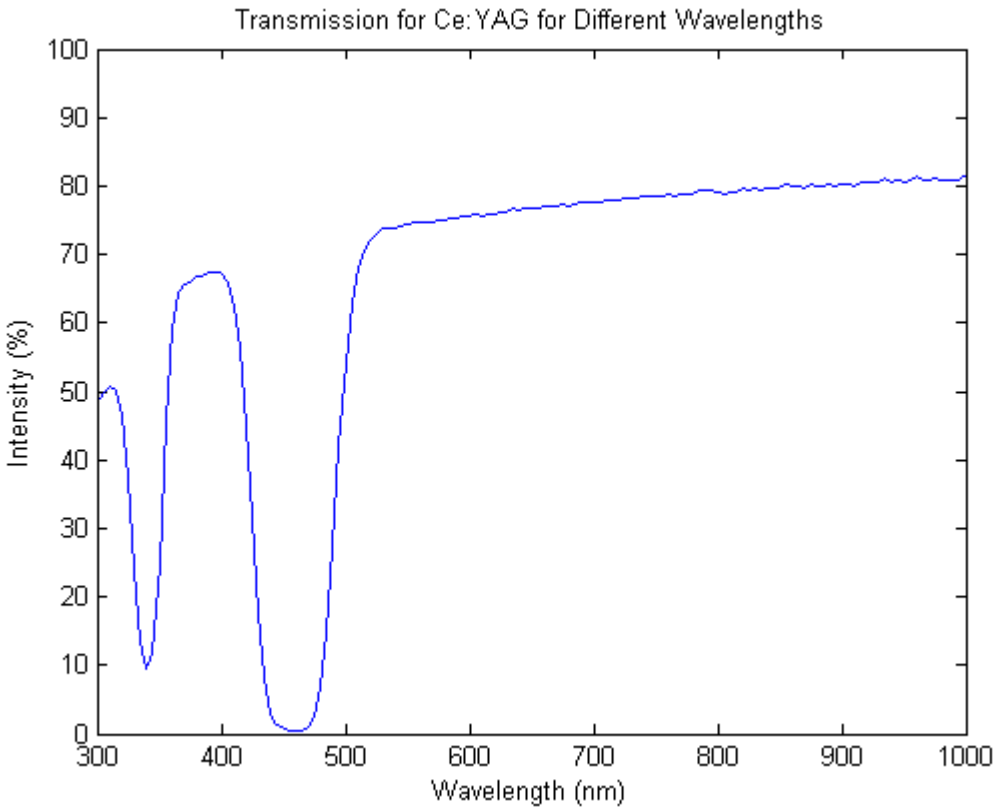

Figure 21: Transmission of light through Ce:YAG for all wavelengths.

From those results, the absorption coefficient for this material was calculated accordingly using Equation 9,

$$I = I_o \exp(-\alpha d)$$

Equation 9: Beer-Lambert's Law, where I_o is incident light, α is the absorption coefficient of the material and d is the thickness of the material [48].

Isolating for the absorption coefficient, gives the following equation:

$$\alpha = -\frac{1}{t} \ln\left(\frac{I}{I_o}\right)$$

Equation 10: Beer-Lambert Law isolating for absorption coefficient.

Using the values obtained for the transmission measurements for I/I_o, the absorption coefficient for a given wavelength is therefore given in Figure 22. At the peak absorption (476 nm), the absorption coefficient is 25.8 cm^{-1}, and only 1.57 cm^{-1} at the peak emission (530 nm).

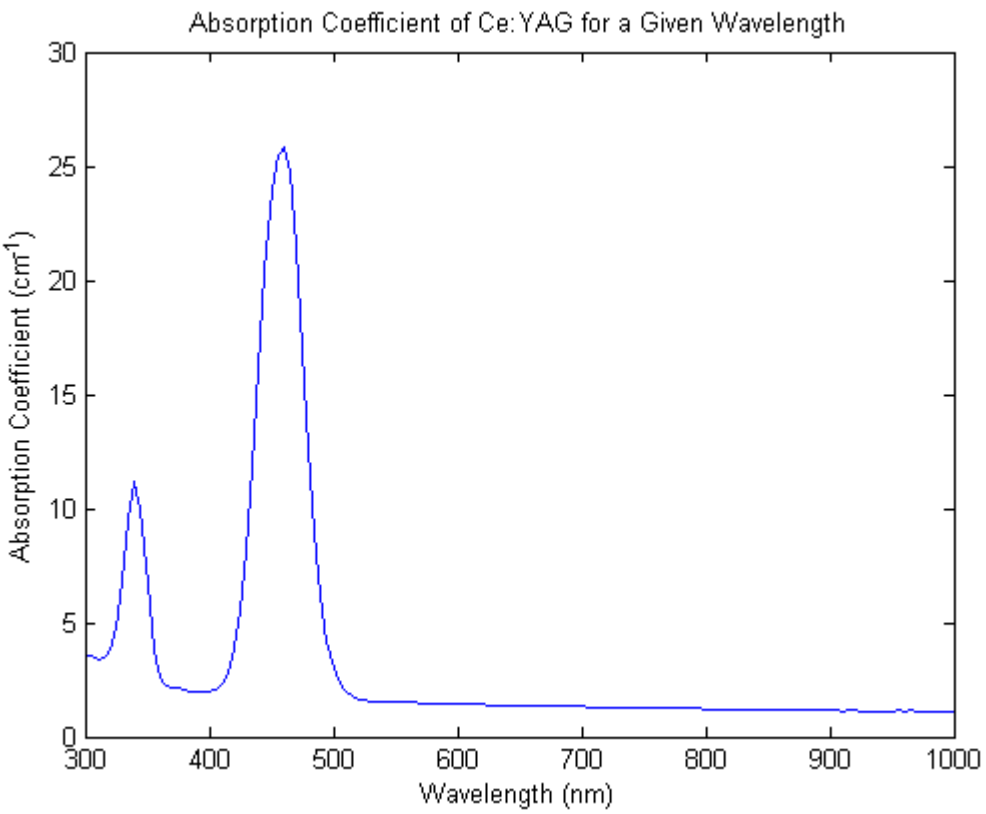

Figure 22: Absorption coefficient of Ce:YAG for a given wavelength.

With the absorption coefficient results, the transmission of light for different wavelengths was modelled for different thicknesses. This was done to determine what the ideal thickness of Ce:YAG should be to ensure maximum absorption of blue light and maximum transmission of yellow light. Once again, the transmission profile was obtained using Beer-Lambert's Law by varying thickness: ranging from 0.010 cm to 0.220 cm at increments of 0.010 cm. Only the transmission profiles for 0.010, 0.050, 0.100, 0.150 and 0.200 cm are displayed in Figure 23.

To establish the value of the ideal thickness, a very low, or rather, deep minima must be exhibited at 476 nm while demonstrating a very high transmission value at 530 nm. A high transmission at 530 nm is required to minimize reabsorption losses, while a “deep minima” maximizes the absorption of blue photons, and therefore more photons would be converted into yellow ones. From Figure 23, a thickness of 0.010 cm maximizes transmission but just over approximately 20% of blue light is absorbed. On the other end, at 0.200 cm thickness, 70% of the blue wavelength is absorbed while approximately 75% of yellow light would be transmitted. To compromise between absorption and transmission, a thickness of 0.050 cm was chosen, about 65% of blue is absorbed and 90% of yellow is transmitted. This particular thickness of Ce:YAG was used to fabricate the concentrator.

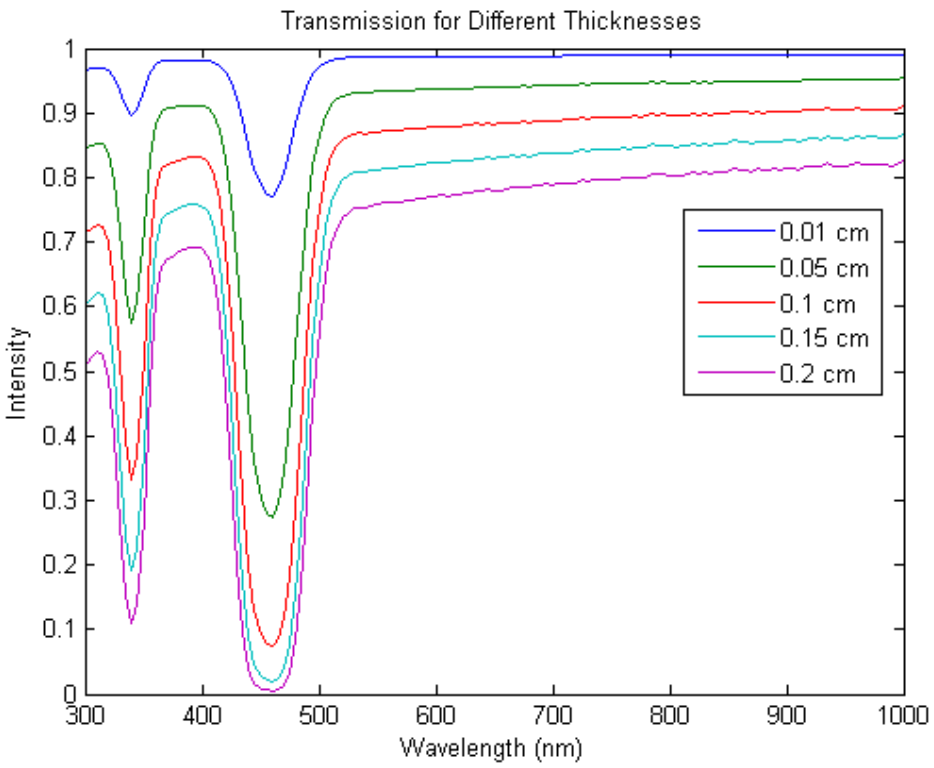

Figure 23: Transmission of light through Ce:YAG for different thicknesses.

4.1.2.2 Time Correlated Single Photon Counting Spectroscopy

Set Up

Time-Correlated Single Photon Counting Spectroscopy (TCSPCS) measured the fluorescence lifetime of Ce:YAG. Unlike in a spectrophotometer, a laser pulse (a NanoLED light source with a wavelength of 455 nm) with a 1.40 ns fall time was used in this setup to excite the cerium atoms. A 500 nm short-pass filter was used to block out longer wavelengths over the active region of the spectrum, while a 515 nm long-pass filter was used to attenuate the shorter

wavelength and transmit the longer ones. In this system, the bandwidth for both excitation and emission were set to 32.0 nm.

Results

TCSPC successfully measured the time it takes electrons to absorb blue photons, get excited to a different energy level, transition to a more stable, lower energy, and finally relax back down to ground state and emit yellow photons. Three different measurements were conducted to obtain a more accurate lifetime, which averaged to 62.3 ns. Refer to Figure 24 for the fluorescence decay of Ce:YAG, which confirms the literature value of approximately 60.0 ns [49], [50].

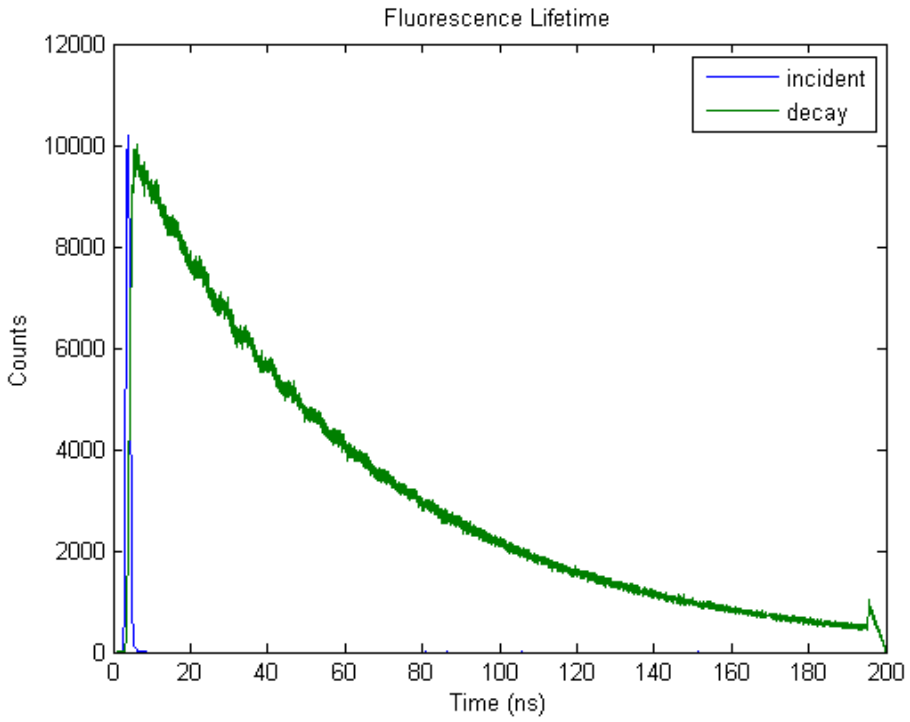

Figure 24: Fluorescence lifetime of Ce:YAG.

4.1.2.3 Quantum Yield

4.1.2.3.1 Saturation

Set Up

The doping level used is rather limited and the cerium atoms would be subjected to a substantial amount of high-energy blue photons from the sun. It is therefore necessary to verify whether these cerium atoms can handle being under the photon flux without experiencing saturation. Essentially, the issue was to determine if there were enough Ce atoms to convert all the blue photons into yellow ones. The number of cerium atoms available for conversion was calculated using Equation 11, where the values for the parameters were obtained experimentally.

$$\text{Ce atoms/unit cell} = \frac{n}{V} = \frac{\rho N_A}{At}$$

Equation 11: Number of cerium atoms available for conversion.

The blue region of the spectral irradiance (from AM1.5G spectrum data [51]), $I_{spectral}$ was integrated to determine the number of photons available for absorption, and a factor of 100 suns was assumed to account for the concentration of light using:

$$\phi_{incident} = 100 \int_{427}^{498} \frac{I_{spectral}}{hc/\lambda}\, d\lambda$$

Equation 12: Photon flux of incident light: $I_{spectral}$ is the spectral irradiance, the term hc/λ is the amount of energy in Joules per photon at wavelength λ, where h is Planck's constant and c is the speed of light.

Finally, the ratio between the two was resolved through:

$$QY = \frac{emitted\ photons}{incident\ photons} * 100\%$$

Equation 13: Quantum yield, ratio of emitted photons to incident ones.

Results

Equation 12 ascertained that there are $3.78x10^{22}$ blue photons/cm^2s available for conversion to yellow photons. Using Equation 12, the number of cerium atoms was found to be $3.15x10^{29}$ at/cm^2s, where the parameters used for this calculation are summarized in Table 3.

Table 3: Properties of Ce:YAG.

Parameter	Value
ρ (g/cm^3)	4.56
N_A (at/mol)	$6.023x10^{23}$
A (g/mol)	140.12
t (ns)	62.3

If it takes one cerium atom to convert one photon, this results in approximately 8.34×10^9 Ce atoms/cm^2/s still available for converting blue photons. Thus, since there are enough atoms available for conversion, no saturation occurs and therefore no luminescent quenching should be observed by this material.

4.1.2.3.2 Quantum Efficiency

To measure the absolute quantum efficiency, a setup consisting of an integrating sphere from LabSphere and a spectrometer/CCD from Ocean Optics (USB 2000+) was used. The experimental set up is shown below in Figure 25.

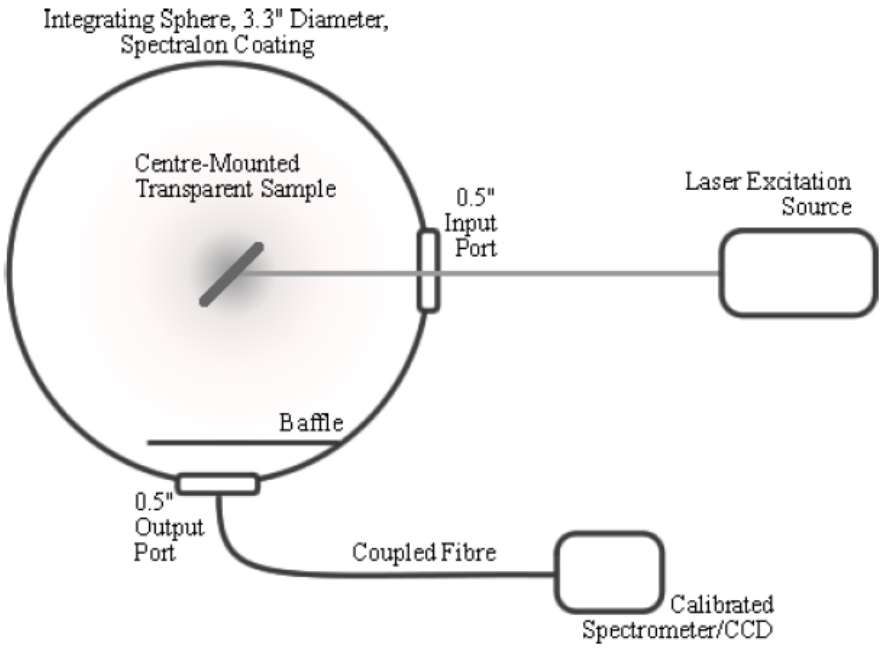

Figure 25: Absolute quantum efficiency setup [39].

The laser used for excitation has a wavelength of 465 nm. The integrating sphere was used to spatially integrate an optical flux while minimizing the amount of losses. Therefore, the CCD's (CS(λ)) and the sphere's response ($R_s(\lambda)$) were accounted for in the calculations for quantum efficiency. This data is found in Appendix A.3.1: Sphere's Response ($R_s(\lambda)$), but is also shown in a graphical form in Figure 26, where the sphere's response is a step function due to low resolution of the reflectivity data, and a smooth approximation polynomial is used to fit the data. In addition, the detector needed to be calibrated to measure Ce:YAG's response in units of absolute irradiance using an Ocean Optics LS-1-CAL lamp. The lamp's irradiance as a function of wavelength is shown in Figure 27.

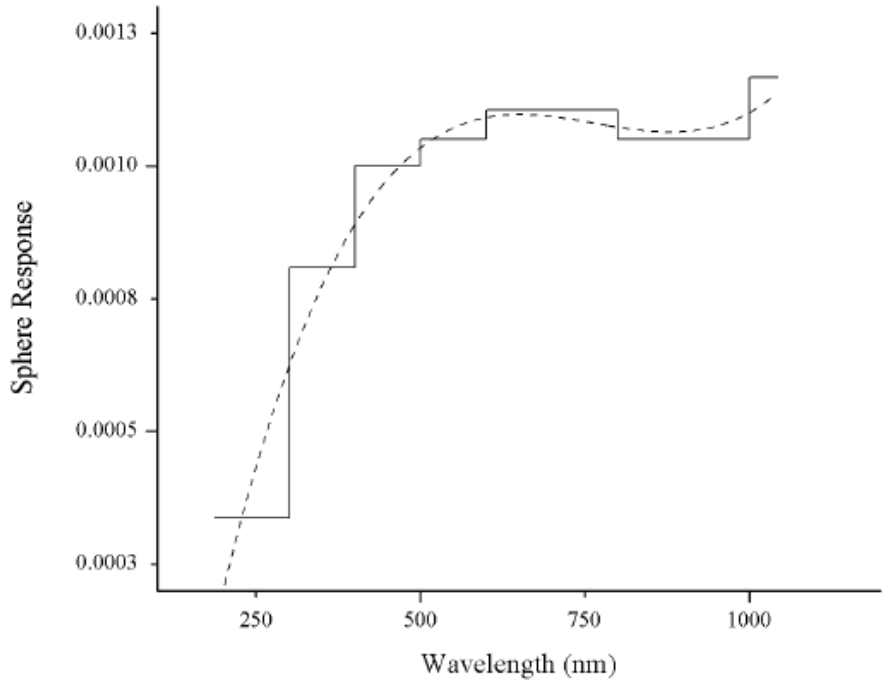

Figure 26: Integrating sphere's spectral response [39].

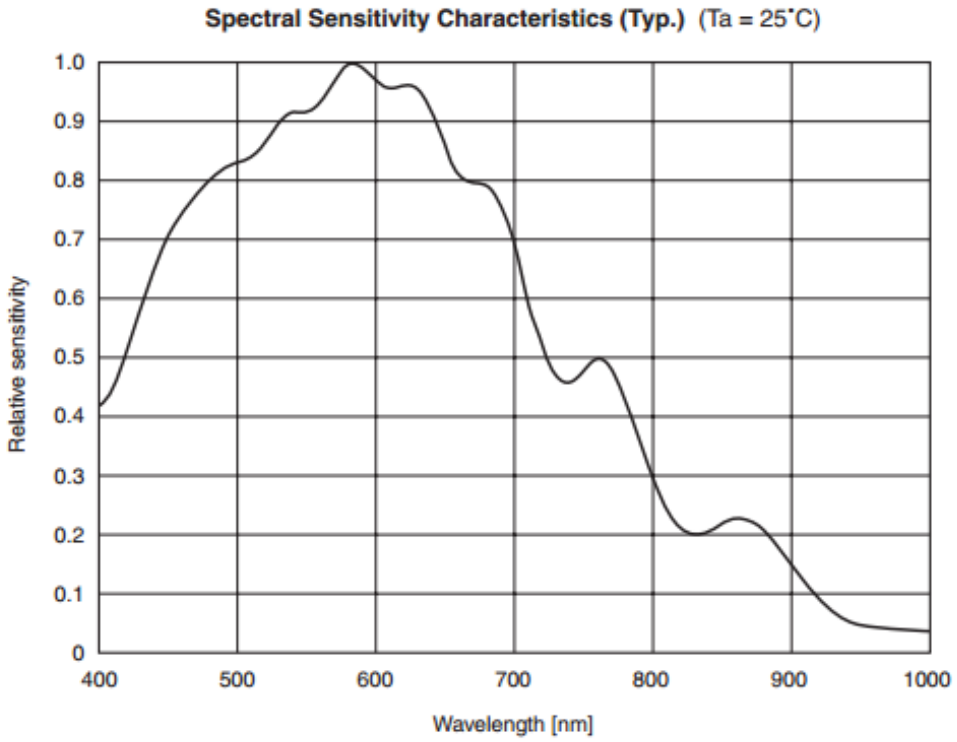

Figure 27: CCD detector's spectral response [39].

To obtain External Quantum Efficiency (EQE) experimentally, the excitation source (incident laser) was first measured in absolute irradiance ($\mu W \cdot cm^2/nm$). Next, the data was corrected for CCD calibration, sphere's response and converted to spectral photon flux (J/m^2s). The results were integrated to determine the total amount of incident light using Equation 14:

$$\phi_{incident} = \int_{427}^{498} \frac{I_{laser} \cdot R_s(\lambda)^{-1} \cdot CS(\lambda)}{hc/\lambda} \, d\lambda$$

Equation 14: Photon flux of incident light (blue light): I_{laser}, is the spectral irradiance, the term hc/λ is the amount of energy in Joules per photon at wavelength λ, where h is Planck's constant and c is the speed of light. $R_s(\lambda)$ is the integrating sphere's spectral response, and CS(λ) is the CCD detector's spectral response.

Similarly, to measure the photon flux emitted by Ce:YAG, a sample was placed inside the integrating sphere to measure $I_{Ce:YAG}$ in absolute irradiance and was converted to photon flux using Equation 15:

$$\phi_{emitted} = \int_{493}^{655} \frac{I_{Ce:YAG} \cdot R_s(\lambda)^{-1} \cdot CS(\lambda)}{hc/\lambda} \, d\lambda$$

Equation 15: Photon flux of emitted photons, $I_{Ce:YAG}$, is the spectral irradiance, the term hc/λ is the amount of energy in Joules per photon at wavelength λ, where h is Planck's constant and c is the speed of light. $R_s(\lambda)$ is the integrating sphere's spectral response, and CS(λ) is the CCD detector's spectral response.

The EQE was then calculated as per Equation 13.

The same procedure was applied to measure internal quantum efficiency (IQE), however, in this situation, only the absorbed photons were accounted for instead of the total incident light. Since light can be reflected, transmitted or absorbed through the material, only the absorbed ones can be used to determine the conversion efficiency of Ce:YAG, and consequently:

$$IQE = \frac{emitted\ photons}{absorbed\ photons} * 100\% .$$

Equation 16: Internal quantum efficiency, ratio of emitted photons to absorbed ones.

From the obtained spectra of both the incident laser ($\phi_{incident}$) and emitted photons ($\phi_{emitted}$), the absorbed photon flux $\phi_{absorbed}$ was calculated through Equation 17:

$$\phi_{absorbed} = \phi_{incident} - \phi_{emitted}$$

Equation 17: Absorbed flux by Ce:YAG.

which was integrated for the specific absorption range of Ce:YAG (between 427 – 496 nm). Using Equation 16, IQE of this material can then be easily computed.

Results

The quantum efficiency of a cubic sample of Ce:YAG is displayed in Figure 28 below. The incident power is indicated in blue, with a peak at 476 nm but is ranging from 427 to 498 nm, whereas the emission by the Ce:YAG is shown in green. In the absorption range (427 to 498 nm), there is some emission by the Ce:YAG, which is in fact 15.5% of the incident power that does not get effectively absorbed and is instead transmitted and reflected. When integrating the areas under both curves and using Equation 13, the EQE was calculated to be 67.6%. The internal quantum efficiency (IQE) on the other hand was calculated to be 80.0% using Equation 16, where Equation 17 was used to account for

specifically absorbed photons instead of the entire incident power. These two values are lower than values obtained in literature, since EQE was reported to be about 75.0% – 77.0% [45], [52], and IQE was generally reported to be close to unity [53].

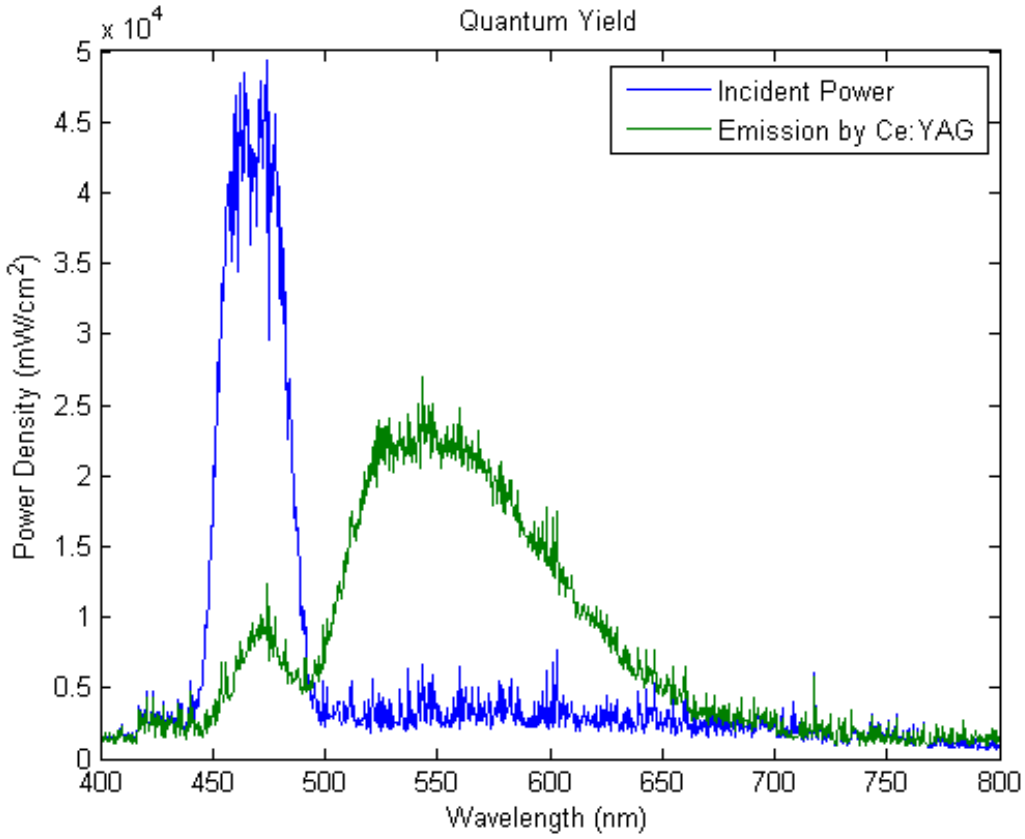

Figure 28: Quantum yield of Ce:YAG, incident light is shown in blue, and emitted by Ce:YAG indicated in green.

4.1.3 Modelling

Two methods were used to model concentrators for this project: Optics Lab and Monte Carlo simulations. Optics Lab is a ray-tracing software used to

physically track the light's path in a medium where the concentrator can be designed to represent a physical one. Specific parameters and conditions can be applied to influence the optical properties of materials and consequently, the behaviour of light through this medium [54].

Monte Carlo Simulations (MCS) is another method that can simulate light's behaviour through a concentrator. It uses a repeated random number sampling to obtain numerical results. It essentially yields the probability distribution for each variable to produce a significant number of possible outcomes [55]. For a concentrator analysis, MCS was used to predict the fate of photons once they are emitted from the FM. As shown in Figure 29, light could travel in different directions at varying angles; consequently, it could be refracted out of the device altogether, intersect with a collecting edge, or reabsorbed if it reaches another fluorescent material [56], [57], [58], [59].

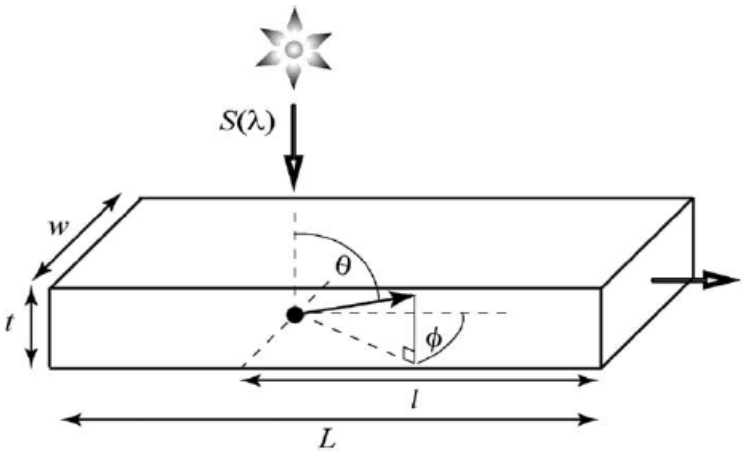

Figure 29: Angle of emission from fluorescent material [56].

5 Preliminary Analysis

5.1 Amount of Emitted Light Waveguided

Using the absorption profile obtained in section 4.1.2.1, the amount collected by the solar cell edges was calculated using Beer-Lambert's law, Equation 9. Figure 30 demonstrates the sample geometry and total internal reflection within a sheet of Ce:YAG. To calculate the light intensity, the absorption coefficient for the emitted photons (yellow) was first deduced to be 1.57 cm^{-1} from Figure 22. Referring to Figure 30, the path length for one reflection was calculated using 33.1° (from Equation 1) as the critical angle:

$$x = \frac{d}{2}\tan\theta_c = 0.0698\ cm$$

Equation 18: Path length for one reflection along the z-axis, where t is the thickness of the material, and θ_c is the critical angle.

making the number of reflections:

$$\#\ of\ reflections = \frac{L}{x} = \frac{0.926}{0.0698} = 13.3$$

Equation 19: Number of reflections during total internal reflection along the length of the concentrator (L), divided by the path length of one reflection.

To calculate the intensity for this one reflection, Equation 9 was used with x for t:

$$\frac{I}{I_o} = \exp(-\alpha x) = \exp(-1.57 \cdot 0.0698) = 0.896$$

Therefore the amount waveguided was:

$$I_f = 100 \cdot \left(\frac{I_1}{I_o}\right)^{\#\ of\ reflections} = 100 \cdot 0.896^{13.3} = 23.3\%$$

Equation 20: Amount of light waveguided at the end of total internal reflection.

This yields approximately 23.3% of light reaching the edges, where 89.6% of intensity is available at the first reflection for a sample of thickness 0.214 cm, compared to an intensity of 97.5% for a 0.050 cm thick sample, with only 23.4% of light waveguided. This result is indicative of Ce:YAG's high attenuation effect.

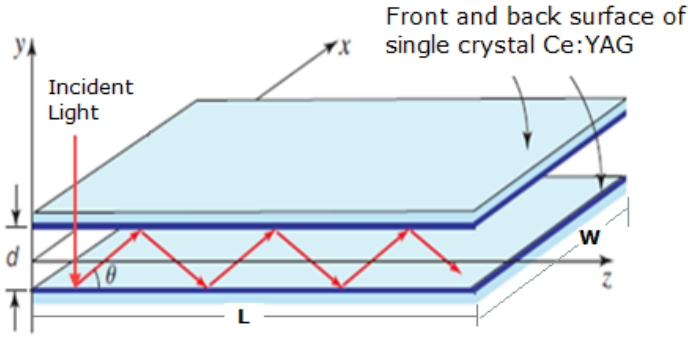

Figure 30: Guided light along a concentrator for dimensions: L = 0.926 cm, w = 0.924 cm and t = 0.214 cm.

5.2 Cost Analysis

The cost for using Ce:YAG was calculated to determine the financial feasibility of the concentrator if this material was used as a fluorescent material. Calculations were made by determining the weight of each element required to make 1.00 m^2 with a thickness of 0.050 cm for a 0.180 mol% doping level of cerium. The cost of $Y_{2.82}Al_{5.00}O_{12.0}$ and $Ce_{0.18}$ was obtained from the companies Alpha Aesar and MTI Corporation; their results are shown in Table 4:

Table 4: Cost of a sheet of Ce:YAG with dimensions 1.00x1.00x0.00005 m^3.

	Alpha Aesar ($) [60]	**MTI Corporation ($) [61]**
$Y_{2.82}Al_{5.00}O_{12.0}$	13 326.11	3 932.30
$Ce_{0.18}$	2 648.06	1 756.57
Total	15 974.17	5 688.87

A detailed calculation is in Appendix A.4.1: Initial Cost Analysis. There is a significant price range since MTI Corporation is a mining company while Alpha Aesar generally supplies to well-funded research institutions; therefore, it would be extremely expensive for them to produce mass quantities. Accordingly, the lower price limit for using Ce:YAG was set to be approximately $5 700 and an upper limit to $16 000. In either case, the cost is exceedingly high considering that a commercial silicon solar cell averages about $200 at the moment, hence it would be extremely impractical to use a sheet of Ce:YAG as a fluorescent

material. Since the main goal of using concentrators in the first place is to reduce costs of solar cells, any potential increase in efficiency will be offset by the cost of Ce:YAG.

5.3 Design Concept

To overcome the attenuation effect of Ce:YAG and its financial concerns, a new design entailing Ce:YAG situated within specific locations (forming a hexagonal array) within an acrylic substrate was proposed. Since the light emitted from the fluorescent material (FM) would be essentially waveguided throughout the acrylic, the attenuation effect would be reduced substantially. In addition, since only local islands of Ce:YAG are required, the cost for using this material is minimized. The design concept of the fluorescent concentrator for this work is shown in Figure 31.

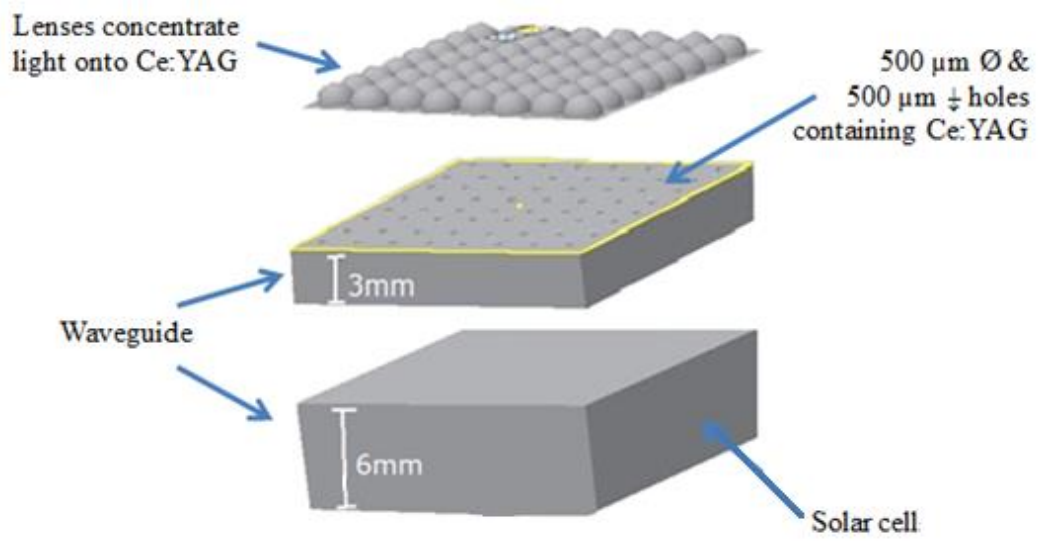

Figure 31: Design concept of the concentrator for this research.

This design uses spatially patterned Ce:YAG arrangement of 500 µm diameter holes and 500 µm thickness located at a distance equivalent to the focal length of a lens sheet. This lens sheet is used to permit strong sunlight coupling to those local islands, while the emitted light from the Ce:YAG is waveguided towards the edges using the second acrylic block. A solar cell is attached at the edge to absorb the photons emitted from Ce:YAG.

To determine the optical efficiency of the concentrator, an Aeroview 70 diffusing screen from Stewart Film screen was bonded onto the side and back surfaces for light measurements. This screen scatters incoming light in all directions and has an almost perfectly Lambertian emission (the brightness does not change regardless of the angle of view) [62].

5.3.1 Preliminary Analysis

5.3.1.1 Amount of Light Waveguided

Following the steps outlined in section 5.1, the amount of light waveguided was calculated using the absorption coefficient of acrylic instead of Ce:YAG, since total internal reflection occurs within this material in the new model. Using the values outlined in Table 5, 75.46% of light is waveguided to the edge solar cell.

Table 5: Variables for calculating the amount of light waveguided

Variable	Value
Critical Angle (º)	41.8
Dimension of Concentrator (cm)	1.90x1.90x0.9
Path length for one reflection (cm)	0.402
# of reflections	4.72
Absorption coefficient	0.148 cm^{-1}
I/I_o for one reflection (%)	94.21
I/I_o Waveguided (%)	75.46

5.3.1.2 Cost Analysis

With the new design, the weight of Ce:YAG required for a 1 m^2 panel has decreased substantially from 2280 g to 1.50 g, the price will therefore drop

accordingly. Table 6 compares the initial required weight with the final weight and the prices for supplier MTI Corporation and Alpha Aesar. The new cost for both companies is a very small fraction, only 0.0658% of the old cost. Detailed calculations will be found in Appendix A.4.2: Cost Analysis for the New Design.

Table 6: Comparing the cost of Ce:YAG for the new and old design.

Material	**Alpha Aesar ($) [60]**		**MTI Corporation ($) [61]**	
	2280 g	1.50 g	2280 g	1.50 g
$Y_{2.82}Al_5O_{12}$	13 326.11	8.77	3 932.30	2.59
$Ce_{0.18}$	2 648.06	1.74	1 756.57	1.15
Total	15 974.17	10.51	5 688.87	3.74

6 Fabrication Technique

6.1 Transparent Substrate

With respect to the waveguide, the polishing procedure was determined followed by identifying which binder to use to allow sufficient adhesion between different samples. It was nearly impossible to attain an optical quality with the resources available, so an acrylic block of an optical finish was purchased instead. The acrylic was cut down to the required size, the front and back surfaces maintained their optical finish whereas the edges undoubtedly resulted in damage from cutting. To remove as much damage as possible, the edges were ground manually using 600, 800 and 1200 silicon carbide (SiC) paper, followed by a brief 6 µm diamond polish. To account for the remaining damage, measurements were taken for an optically finished sample, and for one that had been polished using the steps described above. The losses are therefore calculated and taken into consideration when determining the efficiency of the waveguide.

In order to choose the appropriate adhesive, two specific conditions should be satisfied: it must have a refractive index similar to the acrylic (~1.50) so that the light can pass with minimum reflections between the adhesive and the acrylic, and it must be optically transparent (so that little or no absorption occurs within the adhesive). The four different types of binders used to congeal yttrium aluminum garnet (YAG) powder were: optical cements Sk-9 and J-91, two-part

epoxy and krazy glue. This mixture was embedded in an acrylic substrate followed by adhesion to a second acrylic block, as shown in Figure 23 (to simulate the design explained in section 5.3). Krazy glue was used in (1), J-91 in (2), Sk-9 in (3) and the two-part epoxy in (4). Since the goal of fabricating a concentrator was to maximize the light's optical transport to the edge solar cell, the interface (the binder) needs to be as smooth as possible to reduce light trapping and scattering effects specifically within that region. Although it is cannot be observed in the picture below, using Krazy glue (1) yielded a substantial amount of air bubbles in the physical sample; it was therefore ruled out as an adhesive.

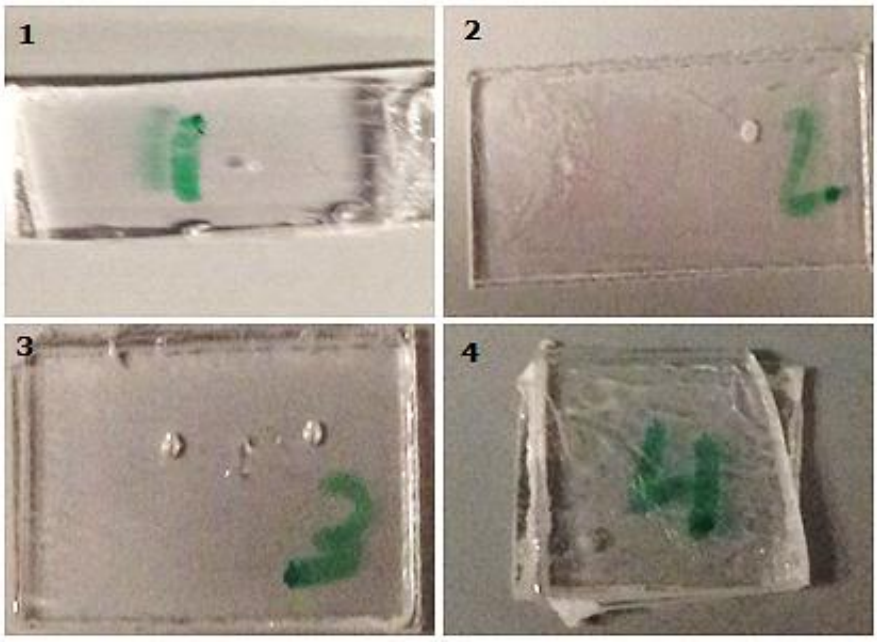

Figure 32: Different binders used for adhesion: (1) Krazy glue, (2) J-91, (3) Sk-9 and (4) Two-part epoxy.

The optical cements, J-91 and Sk-9 yielded very promising results as the interface appeared to be very smooth and almost free of any air bubbles, as can be seen in Figure 32, (2) and (3). The epoxy, on the other hand, resulted in the worst interface as shown in (4). As a highly viscous material, it did not flow across the surface as easily without applying a substantial amount of force in comparison to the others. In addition, it did not cover the entire surface. There were areas that remained completely free of the epoxy, but for the most part the interface was extremely uneven and in some areas even appeared to be peeling.

Results

Moving forward, only J-91 and Sk-9 obtained from Summers Optical were used when fabricating the concentrator; in addition, they were chosen to coagulate Ce:YAG powder so as to minimize the differences in refractive indices throughout the concentrator. Their properties are displayed for comparison in Table 7.

Table 7: Properties of Sk-9 and J-91 [63].

	Sk-9	**J-91**
Viscosity ($N \cdot s/m^2$)	0.080 – 0.100	0.250 – 0.300
Refractive index	1.49	1.55
Operational temperature range (˚C)	-50.0 – 100	-50.0 – 110
Shrinkage on cure (%)	<0.250	0.300
Surface tension (N/cm)	$(3.50 – 3.70)x10^{-4}$	$4.00x10^{-4}$

Although Sk-9 was easier to apply to the substrate due to its lower viscosity, J-91 yielded better results. They both have very high transmission for 350 nm $\leq \lambda$. Figure 33 indicates that J-91 has a transmittance very close 100%, particularly for wavelengths of 530 – 550 nm.

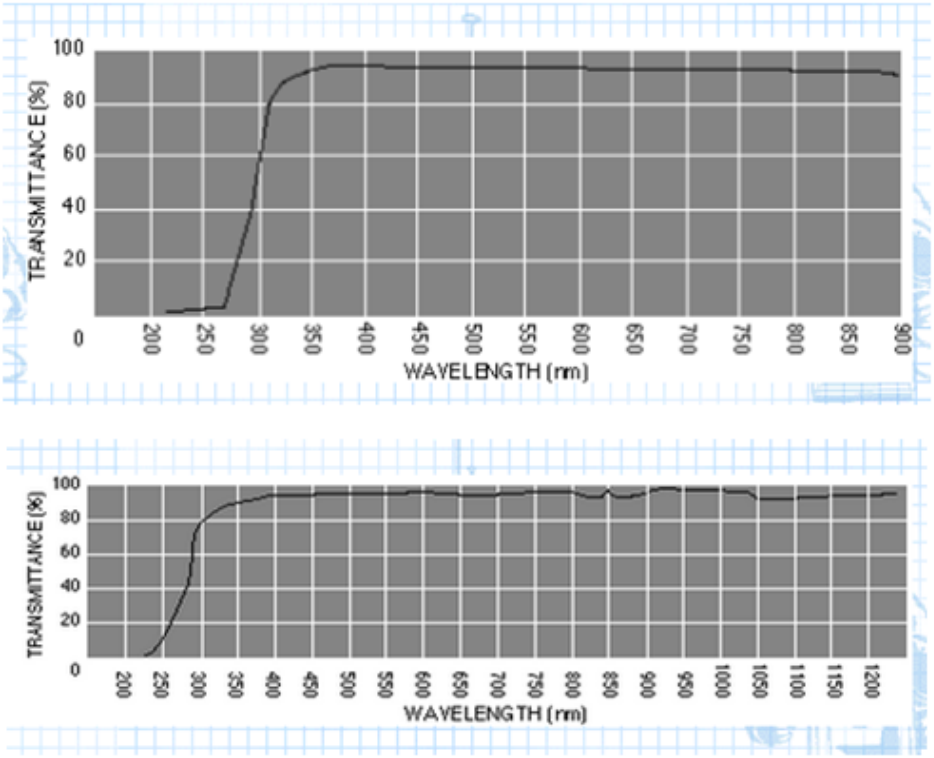

Figure 33: Transmittance of wavelengths through Sk-9 (top), and J-91 (bottom) [63].

6.2 $(Y_{3-x}:Ce_x)\ Al_5O_{12}$

Commercially, the most common Ce doping level is only 0.180 at.%, since a higher quantity causes supersaturation which ultimately leads to higher

reabsorption losses and consequently luminescent quenching [43]. On the other hand, a lower amount does not yield satisfactory intensity results. Ce:YAG in itself was not fabricated during the course of this project. Instead, a single crystal sample was obtained from Scientific Materials Corporation, as well as powder samples with an average particle diameter of 4 – 8 µm from Phosphor Technology Ltd that had a cerium content of 0.180 at.%.

The single crystal was cut using a Struers precision cutter, with a 200-µm blade to a dimension of 0.926x0.924x0.214 cm. The front and back surfaces were polished using 3 µm, 1 µm, 0.3 µm soft polishing cloths that were saturated with colloidal alumina to remove any imperfections and scratches, followed by active oxide polishing silica (OPS) to give the crystal more of an optical finish. A force of 18 N was applied onto the sample holder, and the polishing time was approximately 8 hours for each step.

To determine which lens bond (Sk-9 or J-91) would embed the powder better, 5.00 wt. % of lens bond was first added to two different vials containing 0.125 g of Ce:YAG. The contents were mixed thoroughly using a ball mill to ensure a homogeneous mixture for approximately 15 minutes. Next, the mixture was impregnated in the transparent substrate and exposed to a long wavelength ultra violet (UV) lamp (under 287.5 W) for 30.0 minutes. This process was repeated for another mixture containing 33.0 wt.% of optical cement instead of 5.00 wt. %.

Results

Between the J-91 and Sk-9 lens bond, both were found to congeal Ce:YAG well, however the main difference came from amount of lens bond used (wt.%). The samples with the 5.00 wt.% of optical cement, did not effectively coagulate the entire weight of the powder used, instead when impregnating the holes with the mixture, some powder was able to escape and scatter across the surface when bonded to the second acrylic block.

On the other hand, the samples with the 33.0 wt.% of lens bonded the powder exceptionally well. The entire mixture was well contained within the holes after impregnation and did not scatter across the surface when the substrate was fused with the second acrylic block, as can be seen in Figure 34.

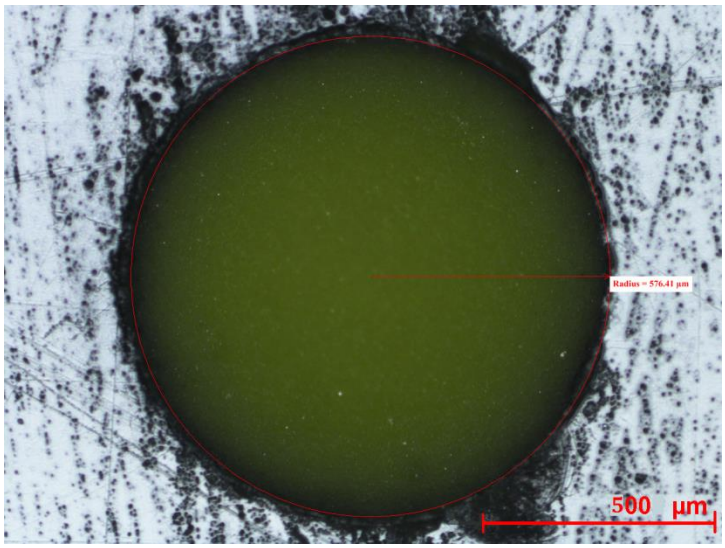

Figure 34: Ce:YAG congealed using Sk-9 and embedded in acrylic.

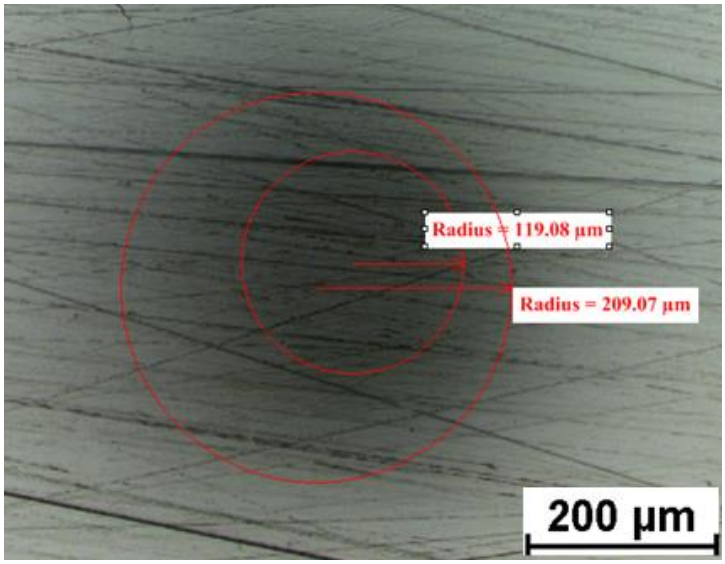

Figure 35: Embedded Ce:YAG in a concentrator.

6.3 Design Concept

The overall fabrication procedure consisted of drilling 500 µm diameter holes arranged in a hexagonal pattern 500 µm deep into the acrylic block (refer to the engineering drawing shown on Figure 36). The acrylic was polished using the steps outlined in section 6.1, then the holes were impregnated with Ce:YAG, and an adhesive was applied to the surface and fused with another acrylic block. Then UV light was used to cure the adhesive.

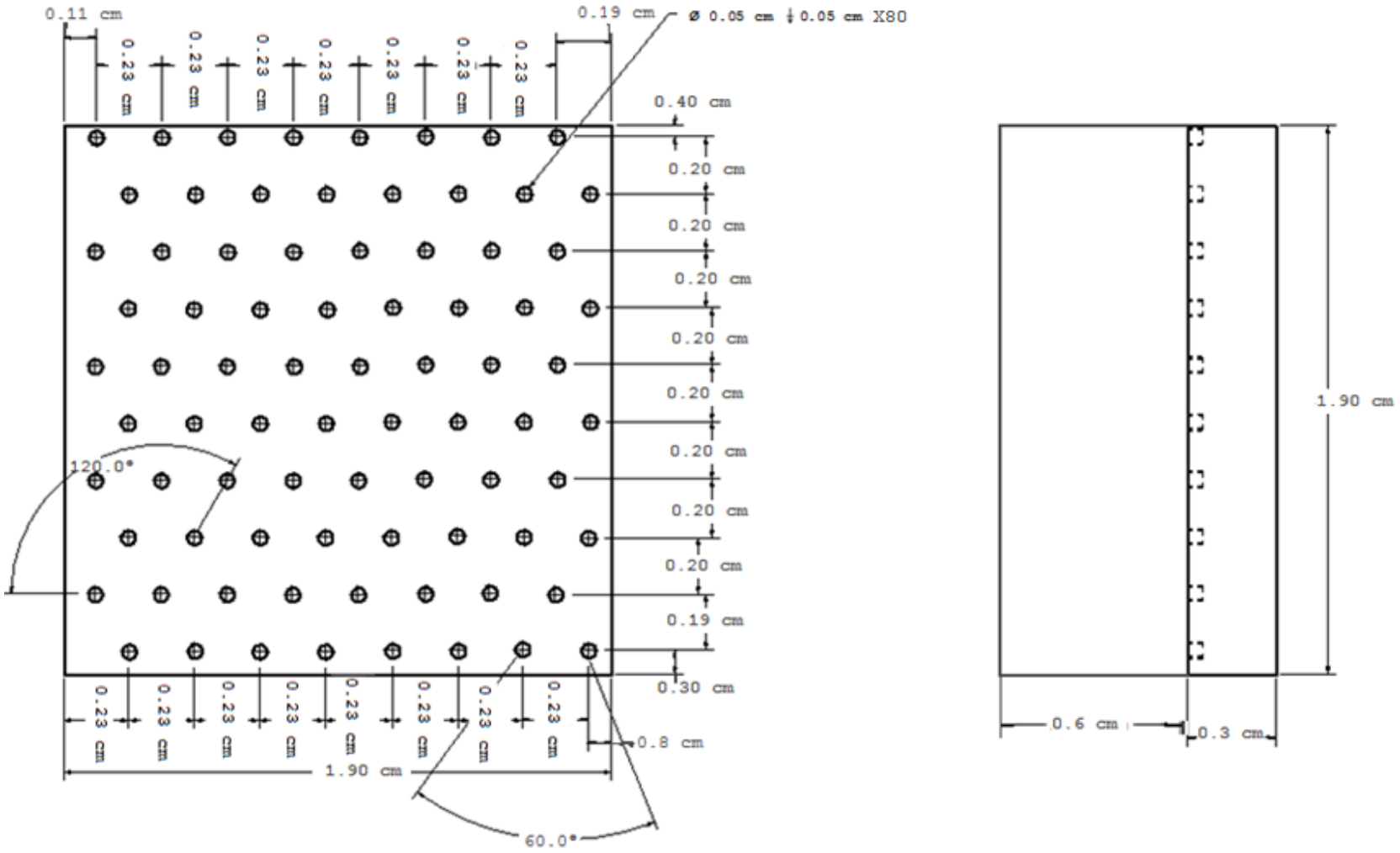

Figure 36: Engineering drawing of concentrator.

With respect to impregnating the substrate containing holes with Ce:YAG, it was observed that the mixture containing J-91 did not cover the entire depth of the hole and it was rather difficult to do so. Using Sk-9, it was easier to force the mixture 500 µm deep into the substrate. This could be attributed to the fact that Sk-9 had a slightly higher surface tension (although it seemed insignificant initially). If these holes were treated as a tube, higher surface tension could draw 'liquid' to a higher depth (phenomenon known as capillary action [64]); therefore allowing the entire depth of these holes to be covered. For this reason, and the ease of application of the lens bond to a substrate (for fusion), Sk-9 was used to fabricate the concentrator, despite a slightly lower transmission of light. Figure 37 is an example of a successfully fabricated prototype.

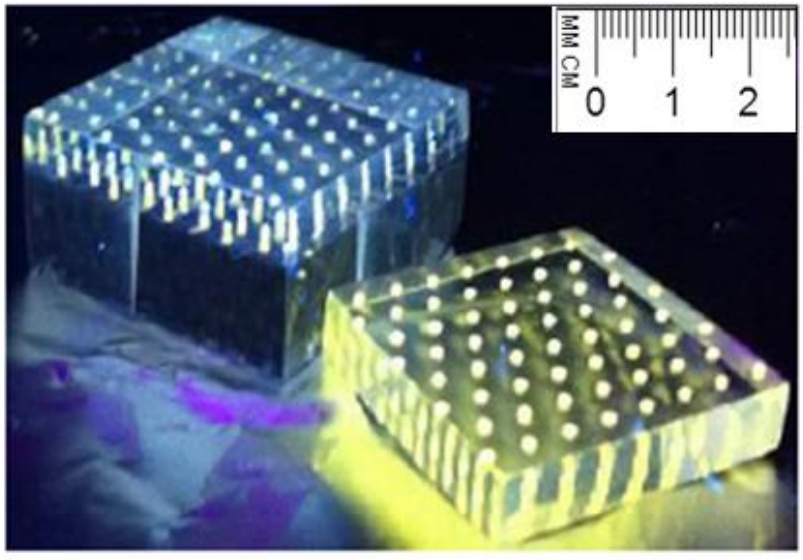

Figure 37: Fabricated concentrator. Light is shone on top of the prototype, getting absorbed by Ce:YAG and waveguided to the edges.

7 Concentrator Analysis

7.1 Optics Lab Simulation

Set Up

Optics Lab is a ray tracing software that evaluated the performance of the concentrator using the design described in section 5.3. Using this software, a concentrator with dimensions 1.90x1.90x0.90 cm was simulated with a refractive index of 1.50. Five convex lenses with a diameter of 0.229 were placed on top of the acrylic and have a focal length of 0.300 cm. These lenses were situated to show where the focal point of which the incident photons would converge to, but does not serve to account for how much light intensity the Ce:YAG would be subjected to under concentration. At this particular distance away from the lenses, five light sources, were simulated to represent Ce:YAG (therefore properties of Ce:YAG were used) and behave in the same way this phosphor would when it absorbs blue photons. The parameters for these local islands of Ce:YAG are summarized in Table 8. Another blue light source is placed at a far enough distance from the concentrator such that the rays travel parallel to each other, and bend when they interact with the lenses to form a focal point on the Ce:YAG. In addition, detectors were placed at two edges of the concentrator to detect how much light gets waveguided, in addition to one on top and one below the concentrator to detect the amount that is refracted out. A simulated schematic is shown in Figure 38.

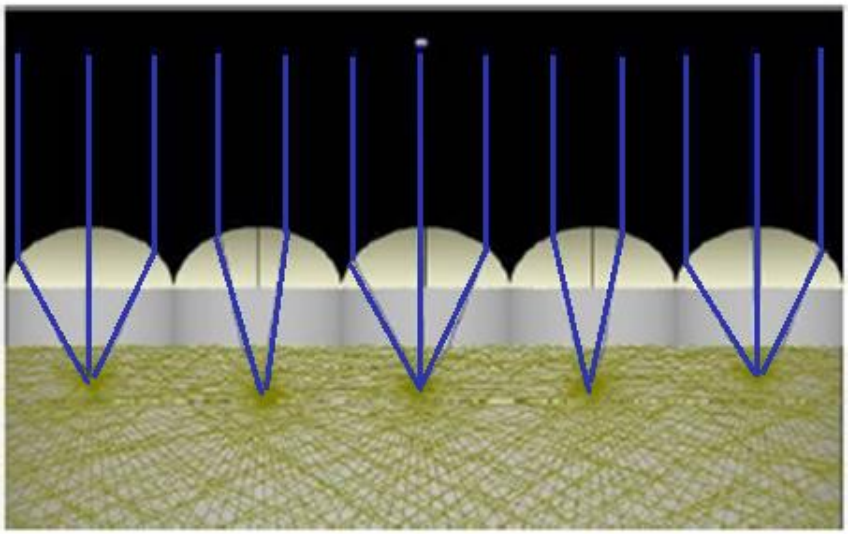

Figure 38: Optics Lab simulation showing absorbed blue concentrated onto Ce:YAG and emitting yellow photons.

Table 8: Source parameters input into Optics Lab for simulation.

Source Parameters	
Number of rays	1817 (2D)
Size of source	0.500 mm
Radius of curvature	0.001 mm
Radiation direction	Both ways (360˚ radiation)
Index of refraction	1.83
Power emitted per source	1.00 W

In this software, only the emitted photons can be simulated and their behaviour traced throughout the concentrator, but this does not model the effects of incident photons (i.e. absorption and transmission). Therefore, due to the

limitations of this program, it was assumed only blue photons enter the concentrator, and Ce:YAG effectively absorbs them all (absorption efficiency is 100%). In addition, when determining the amount of light that can be waveguided, the results are compared to 100% emitted by the Ce:YAG (1.00 W per light source for a total of 5.00 W).

Results

Figure 39 indicates that 16.9% of light was refracted out of the top surface, while a much more significant amount was refracted out of the bottom surface – 22.2%. The remainder, 56.1% was waveguided towards the edges. One reason for having more photons escaping from the bottom than the top is the presence of the lenses above the concentrator. As can be clearly seen in this figure, each lens acts to trap some light at the interface between two lenses (Figure 39, on the right). This however still leads to a similar conclusion that 21.7% still refracted out of the concentrator and does not get waveguided. When calculating the escape cone fraction for an acrylic substrate with a critical angle of 41.8º, only 12.7% was refracted out of the concentrator for half of the length of the concentrator (L/2), and 25.5% for the entire length of the concentrator (i.e. out of the full solid angle of a sphere, 4π). The 3.30% difference between the calculated I_{esc} and that simulated in Optics Lab, was small, making the two results comparable.

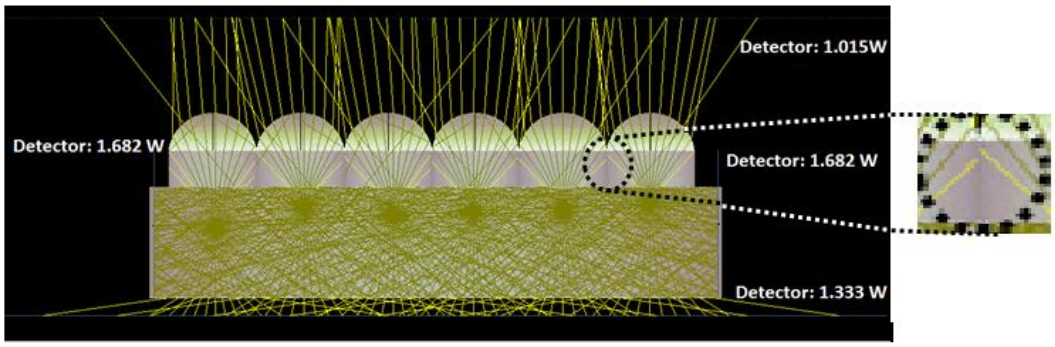

Figure 39: Optics Lab simulation of concentrator with Ce:YAG embedded in an acrylic substrate, total amount of light emitted in total is 5.00W. A zoomed area between two lenses is shown trapping some of the fluorescence.

7.2 Monte Carlo Simulation

For easier comparison with the results obtained from Optics Lab, MCS was simulated to represent the way light travels through an acrylic substrate with the dimensions 1.90x1.90x0.900 cm. This simulation was initialized after emission of specifically yellow photons with a wavelength of 530 nm (corresponding to the peak emission for the 0.180 mol.% doping level) from 500 µm diameter and 500 µm thick fluorescent material embedded in the concentrator. Essentially, a random direction was assigned to the emitted photon by generating a random number between [0, 360º] in the theta and phi direction. The photon would be trapped internally for angles between:

- $41.8^{\circ} < \emptyset/\theta < 138.2^{\circ}$,
- $221.8^{\circ} < \emptyset/\theta < 318.2^{\circ}$

and refracted out of the concentrator for all other angles. Using this assigned angle, the path length for this photon was calculated using

$$d = \frac{l}{\sin\theta \cdot \cos\emptyset}$$

Equation 21: Path length for one reflection in a 3D model [56].

from which it could be determined whether or not this photon would intersect a collecting face, or would get reabsorbed. If it does not get reabsorbed, the number of reflections the photon can be subjected to before collection can be determined through Equation 19.

Since all the local islands of Ce:YAG would be located in very specific positions, it was deduced that self-absorption could only occur if the photon was emitted at 90º or 270º in the theta range given that phi is 0 º (since they are located 0.3 cm from the top of the concentrator). Similarly, absorption of fluorescence could only occur for angles of 45º, 67.5º, 90º, 112.5º, 135º, 225º, 247.5º, 270º, 292.5º and 315º (due to the hexagonal array pattern of the holes) for the phi range, given that theta is 0º (refer to Figure 40).

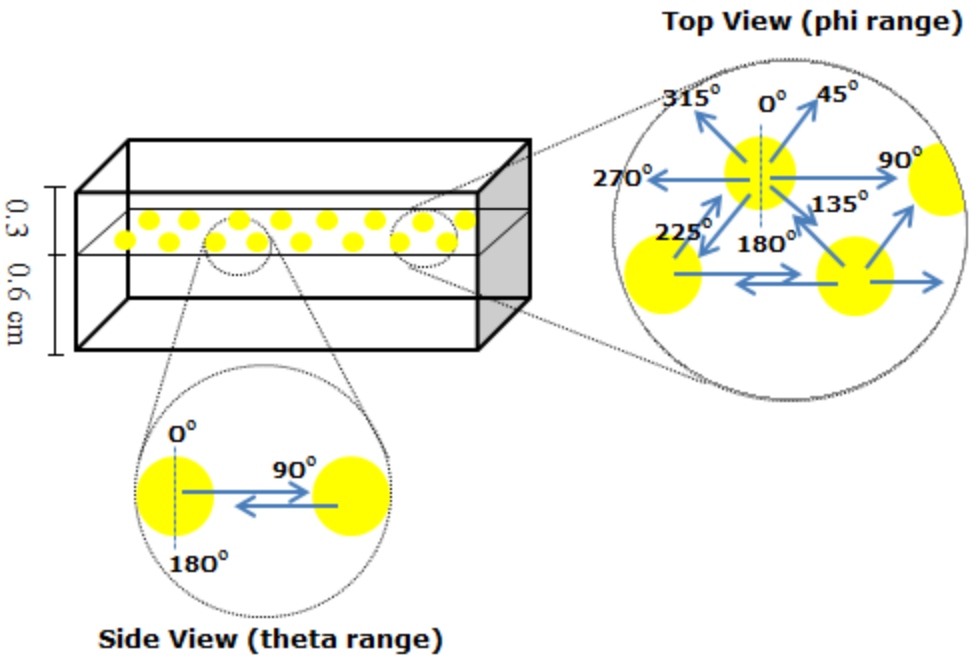

Figure 40: Conditions for reabsorption of fluorescence by Ce:YAG.

An assumption could be made that only blue photons are absorbed, and Ce:YAG would be transparent to all other wavelengths since the absorption efficiency of yellow light is extremely low by this material (absorption coefficient of 1.57 cm^{-1} for yellow light vs. 25.8 cm^{-1} for blue). Using the values for the absorption coefficient obtained experimentally, the intensity of light for the first reflection, I_1, was calculated using:

$$\frac{I_1}{I_o} = exp\left[-\left(\alpha_{m,\lambda} + \alpha_{Ce:YAG,\lambda}\right)d\right]$$

Equation 22: Beer-Lambert's Law where $\alpha_{m,\lambda}$ is the absorption coefficient of the matrix for a given wavelength, $\alpha_{Ce:YAG,\lambda}$ is the absorption coefficient of Ce:YAG for a given wavelength, and d is the path length for one reflection.

Since this concentrator consists of two different materials (Ce:YAG and acrylic), both of their absorption coefficients are taken into consideration. Depending on the number of reflections, the final intensity, I_f, collected by the edge solar cell was then calculated using Equation 20.

Once I_f was determined, the second photon undergoes the same route. This method was repeated 100 000 times until all photons were processed, which were then integrated to determine the total number that was actually waveguided from the 100 000 photons emitted. A flow chart representing the Monte Carlo Simulation is shown in Figure 41. This simulation was conducted in Excel, and a screen shot of the code used is found in Appendix A.5: Monte Carlo Simulation Code.

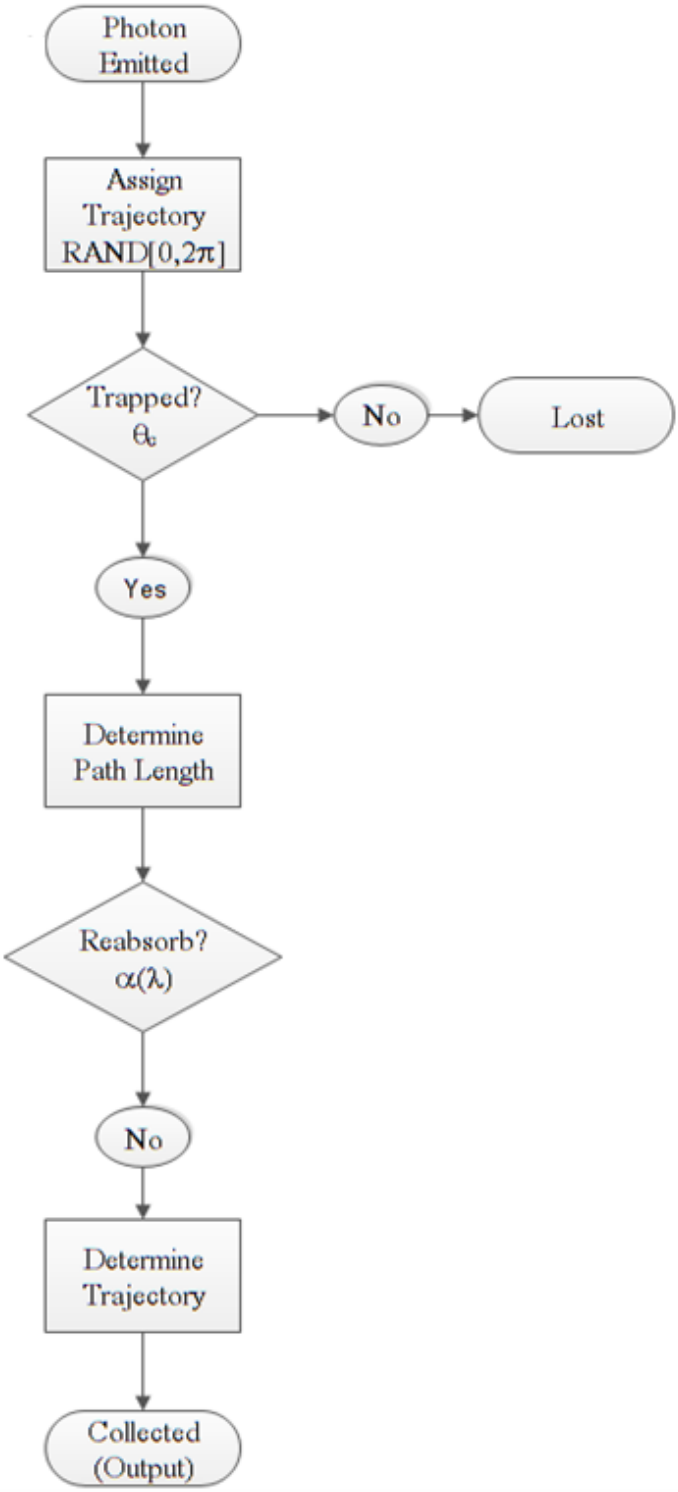

Figure 41: Flow chart representing the Monte Carlo Simulation conducted.

Results

In this simulation, Ce:YAG converts only blue to yellow photons, thus the absorption coefficient for those two wavelength ranges were compared. The absorption coefficient for yellow is only 1.37 cm^{-1} compared to 21.3 cm^{-1} for blue light (an average value of absorption coefficient is used for blue and yellow wavelengths), consequently, making light within 530 – 575 nm wavelength range poorly absorbed, therefore it was assumed that there would be no reabsorption of fluorescence.

For this model, a random number was generated for the angle of emission in both the phi and theta range (refer to Figure 29). If the path length calculated using Equation 21, was greater than 1.90 cm, the photon would intersect a collecting edge since the dimension of this concentrator is 1.90x1.90x0.900 cm. Therefore 1.90 cm was used; otherwise, the number of reflections was determined using Equation 19. Subsequently, the amount of yellow light waveguided to the edges was calculated to be 59.2%, and an average for 100 000 photons was computed to which the results still yielded 59.2%. A snap shot of the simulation is shown in Figure 42. Blue light, on the other hand, shows that $2x10^{-15}$ % was waveguided to the edges for 100 000 photons, which was consistent with the assumption for this simulation that 100% of blue light was effectively absorbed and converted to yellow light by the Ce:YAG.

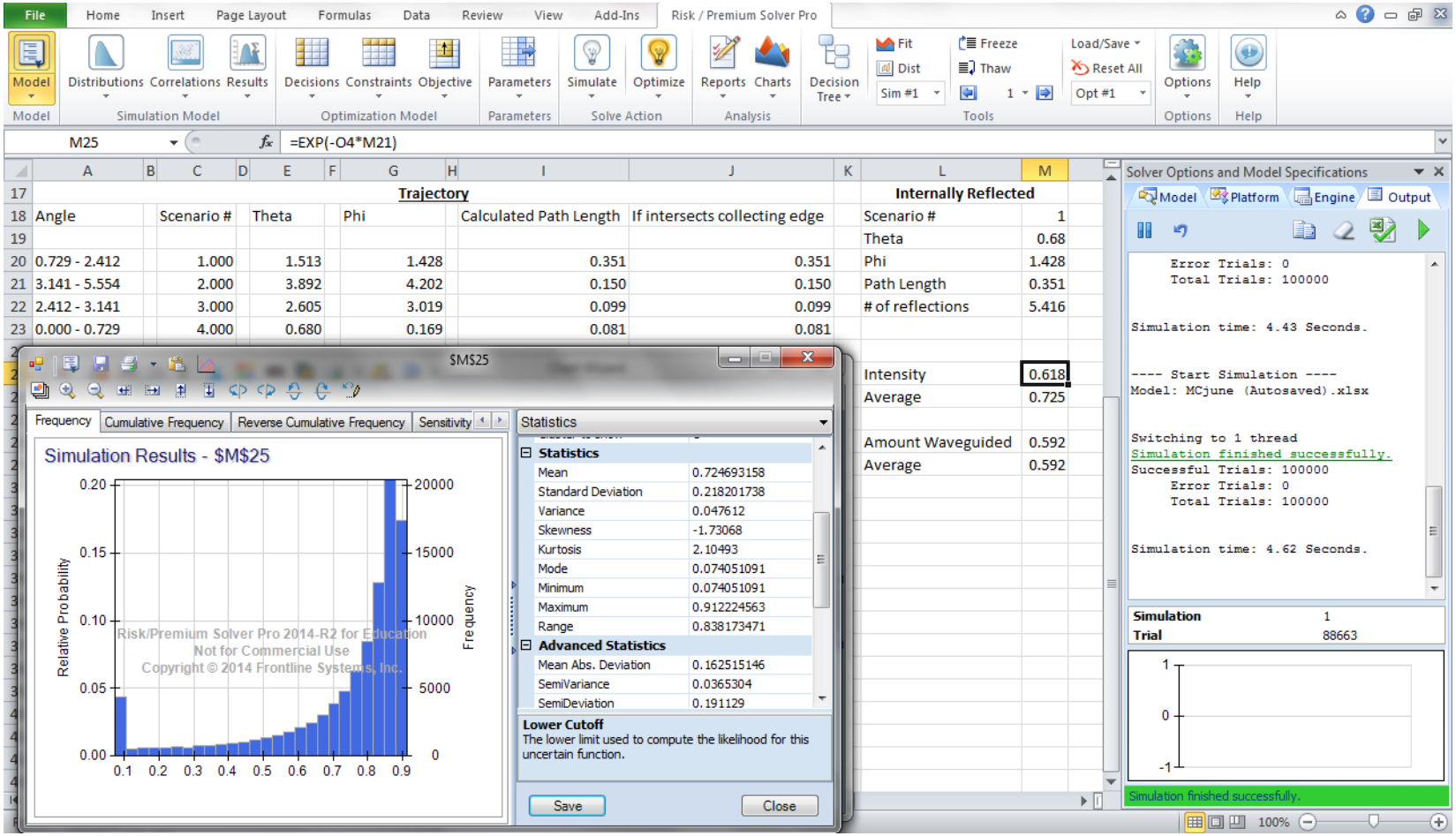

Figure 42: Snapshot of Monte Carlo simulation: angle of emission is measured in radians, thus the photon is internally reflected for angle range between 0.729 - 2.412 rad and between 3.141 – 5.554 rad, in both the theta and phi direction.

7.3 Optical Efficiency

7.3.1 Flux Measurements

To determine the optical efficiency of the concentrator, several parameters must first be measured as per Equation 4. Since the parameters pertaining to the fluorescent material were measured when Ce:YAG was characterized, the main objective for this experiment was to determine the efficiency of the waveguide.

In this apparatus, a photometer was used to measure the light intensity on the surface of the fabricated concentrator, in which six different experiments were conducted with its parameters listed in Table 9. The anode of the blue LED was soldered to a resistor that was connected to the cathode of an HP6217A power supply, while an alligator clip was used to connect the anode of the power supply to the cathode of the LED. To measure the flux of strictly blue light, a 068 Lee Blue filter was used to transmit wavelengths within the range 450 nm $\leq \lambda \leq$ 500 nm while a 021 Lee Gold Amber filter was used to transmit 525 nm $\leq \lambda \leq$ 600 nm. These filters' transmission with respect to wavelength is found in Appendix A.6: Filters' Transmission.

Table 9: Values of parameters used to setup flux measurements.

Parameter	Value
Distance between LED and area of interest	10.0 cm
Distance between photometer and area of interest	15.0 cm
LED wavelength	465 nm
Current	15.0 mA
Resistance	467 Ω
Units of flux measurements (luminance)	Cd/m^2

The first setup required the blue LED to shine perpendicular to a surface with the photometer situated next to it also perpendicular to the surface, as shown in Figure 43 below. The first experiment consisted of a surface of Lambertian white paper to determine the flux of light exiting the blue LED. The second experiment entailed a condensed Ce:YAG powder contained in a white plastic dish to determine the flux of emitted photons.

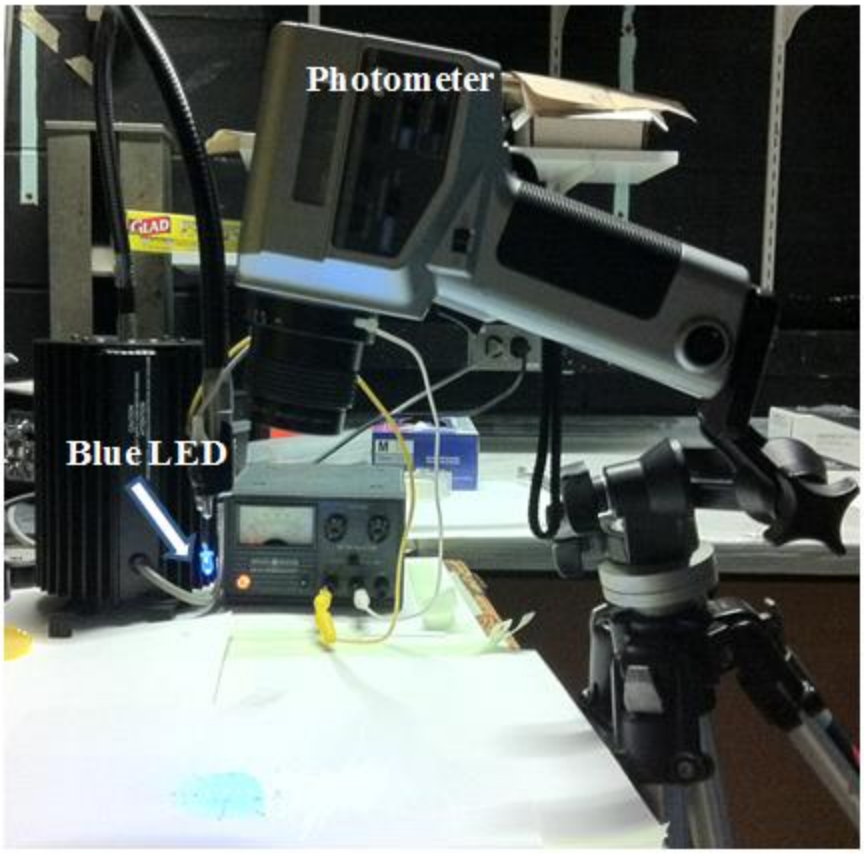

Figure 43: Blue light shining perpindicular to a suface, and photometer set up perpindicular to the surface to take luminance measurements.

The second apparatus contained two different sets of measurements. In both cases, the blue LED was shining onto the top surface of the fabricated concentrator while the photometer was located so as to measure flux off the side edge, as shown in Figure 44 B) below. The only difference between the two is that in one experiment, lenses were placed on top of the concentrator while the other one did not.

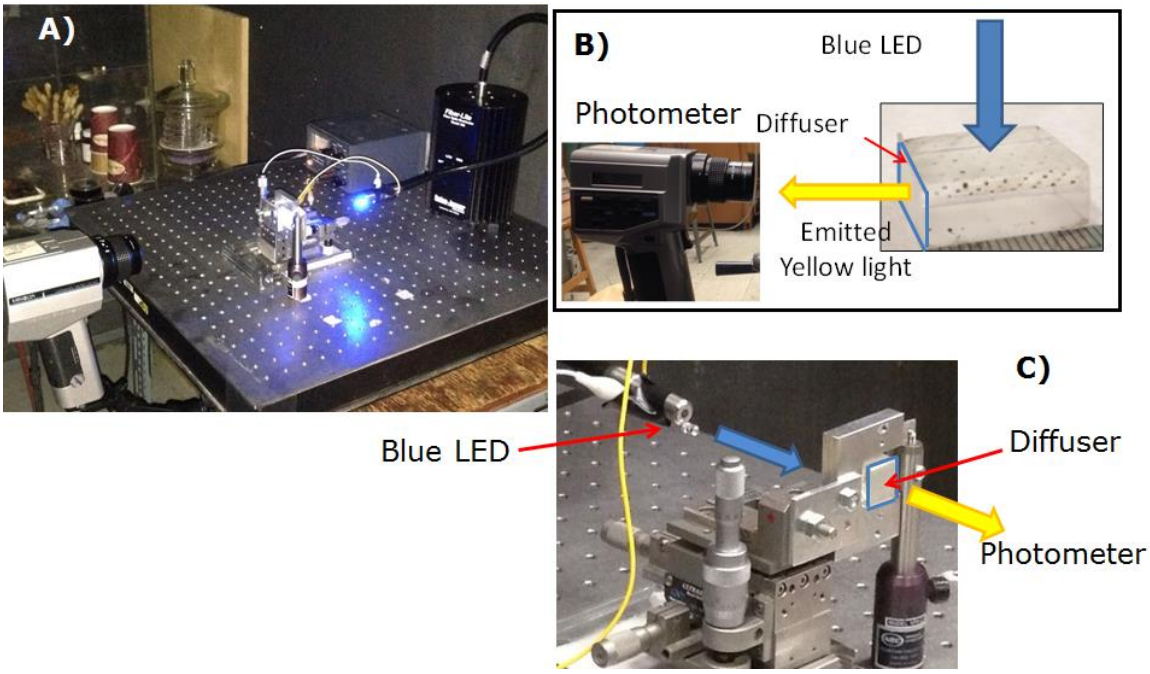

Figure 44: A) Overall Experimental Setup for flux measurements, B) Measuring flux at the edge surface, C) flux out of the back surface.

The third apparatus was set up exactly in the same manner as the second one, but the only difference between them is that in the third case, the flux was measured at the back surface instead of the side edge as shown in Figure 44C. For both the second and third setups, the concentrator was varied from its preferred position in the x and y direction at 30 µm intervals to simulate the sun's position with respect to the lenses. Since the sun moves across the sky from sunrise to sunset, the sun rays would always be at a 90.0º angle to the lenses. Therefore, light would not be focusing onto the Ce:YAG most of the time. Instead, the focal point would constantly change throughout the day. This experiment would yield a better understanding of how much light would still be waveguided whether or not

the local islands of Ce:YAG were situated at optimal position with respect to the lenses.

Results

The outcome for this analysis is outlined in Table 10. Measurements were taken for both blue and yellow light that exited the edge and back surfaces, without the presence of lenses and with lenses at its optimal position with respect to Ce:YAG islands. These results were strictly normalized to the total Ce:YAG area (0.00132 cm^2) with respect to the total surface area of the concentrator (0.0342 cm^2), i.e., normalized to total light emitted by Ce:YAG, where yellow and blue light were analysed separately. Meanwhile, the columns marked "Total" represent the total amount of light that satisfies that particular condition, for yellow and blue light combined. Significantly, more yellow light was waveguided in comparison to blue light since blue light (approximately 85% of absorbed light) was supposed to be efficiently converted to yellow light and emitted by the phosphor.

Table 10 shows that with the presence of lenses, 0.678% more yellow light was waveguided to the edges compared to the results without the presence of lenses. A decrease of 0.264% of blue light was refracted out of the back surface with lenses, indicating slightly more blue light was absorbed and converted to yellow light. The overall amount of light refracted out from the top and bottom of the concentrator decreased by 1.08%.

Table 10: Results of flux measurements, waveguide efficiency normalized to Ce:YAG area (100% emitted).

Surface	No lenses (Yellow)	Lenses (Yellow)	No Lenses (Blue)	Lenses (Blue)	Total No Lenses	Total Lenses
Waveguided to Two Edges (%)	56.73	57.41	0.410	0.814	57.14	58.22
Refracted Out of Back Surface (%)	20.60	20.33	0.824	0.559	21.43	20.89
Refracted Out of Top Surface (%)	20.60	20.33	0.824	0.559	21.43	20.89

Table 11: Comparing waveguide efficiencies for Optics Lab, Monte Carlo, and experimental results.

	Optics Lab (%)	Monte Carlo (%)	Experimental No Lenses (%)	Experimental Lenses (%)
Edge Surface	56.10	59.20	57.14	58.22
Refracted out of Back Surface	22.20	20.40	21.43	20.89
Refracted out of Top Surface	21.70	20.40	21.43	20.89

Table 11 compares experimental results with those calculated previously through Optics Lab and Monte Carlo simulations. Experimental results fall within experimental error of calculated results, which was expected. This was the outcome because those results were normalized to emitted photons. In other words, the amount of fluorescence measured at the edges is strongly dependent on the waveguiding efficiency. Given that optical finish was maintained within the substrate, there should be very little to no damage, and the percentage of fluorescence reaching the edges should not be affected.

The second portion for this experiment required varying the position of the lenses as shown in Figure 45 below, with respect to the position of the local islands of the phosphor in the x and y direction at 30 µm increments.

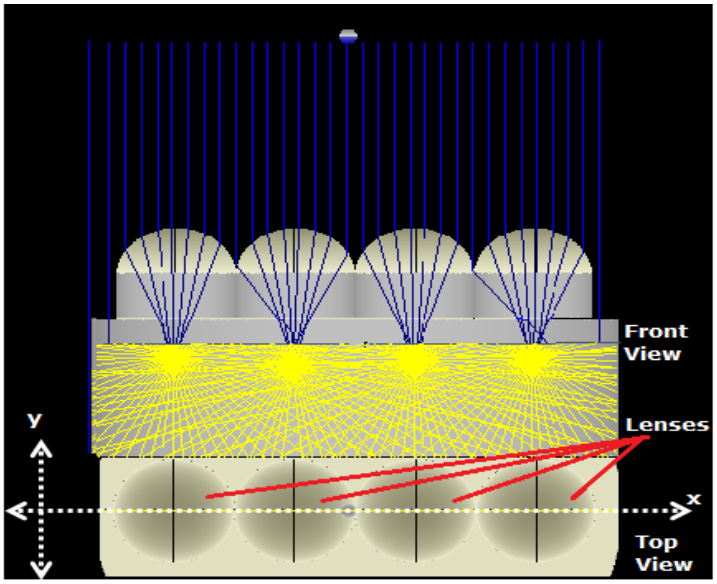

Figure 45: Front and top view of design with lenses to show x and y direction in which the lenses would move.

Those results are displayed in contour plots shown in Figure 46. The regions shown in red pertain to the maximum luminance measured, which correspond to when the lenses are at an optimal position that allow the light to focus directly onto the Ce:YAG. The dark blue imply that the lenses are situated to focus light onto a point half-way between two local islands of Ce:YAG.

The outcomes for blue and yellow light out of the edge surface were consistent with each other, meaning that they both exhibited a maximum and a minimum luminance at the same lens positions with respect to the Ce:YAG (refer to Appendix A.7: 2D Plot of Luminance with Respect to Position of Lenses). This was consistent with theory since very little blue light was expected to be waveguided relative to input power since the absorption efficiency of blue light for this material is approximately 85%, and the little that was observed could be a result of imperfections and defects. Also, it is possible that some of the blue LED rays scatter off the outside all surface of the holes containing Ce:YAG, therefore causing the blue photons to change direction and internally reflect instead of all photons transmitting out of the back surface concentrator.

The opposite effect was observed out of the back surface, where a maximum of yellow light corresponded to the minimum of the blue light and vice versa as shown in Figure 47 (also shown in Appendix A.7: 2D Plot of Luminance with Respect to Position of Lenses). This was expected because if the blue LED light was focused onto Ce:YAG, the blue should be converted to yellow and refracted out of the back surface, and very little amount of non-absorbed blue

should be detected. Meanwhile, at the half-way point between the two local islands Ce:YAG, only blue light should be observed since theoretically there are no cerium atoms present to convert those photons. However, some yellow light was still seen at those positions since there were some traces of Ce:YAG powder visible in between those local islands. Also, there is always a chance that the local islands of Ce:YAG would be exposed to absorption of blue light even if they were not positioned at the focal point of the lenses. As mentioned previously, defects cause the incoming light to change course of direction towards Ce:YAG, thereby yellow light would be radiated.

The results from this experiment allude to the fact that there would always be yellow light present even when the lenses are located in an undesirable position, i.e. located so that light is not focused onto Ce:YAG but on some other position. Therefore, some light would always be waveguided towards the edges. However, since a relatively poor luminance of yellow light is observed at this position, more blue light would be absorbed at the edge solar cell instead of yellow.

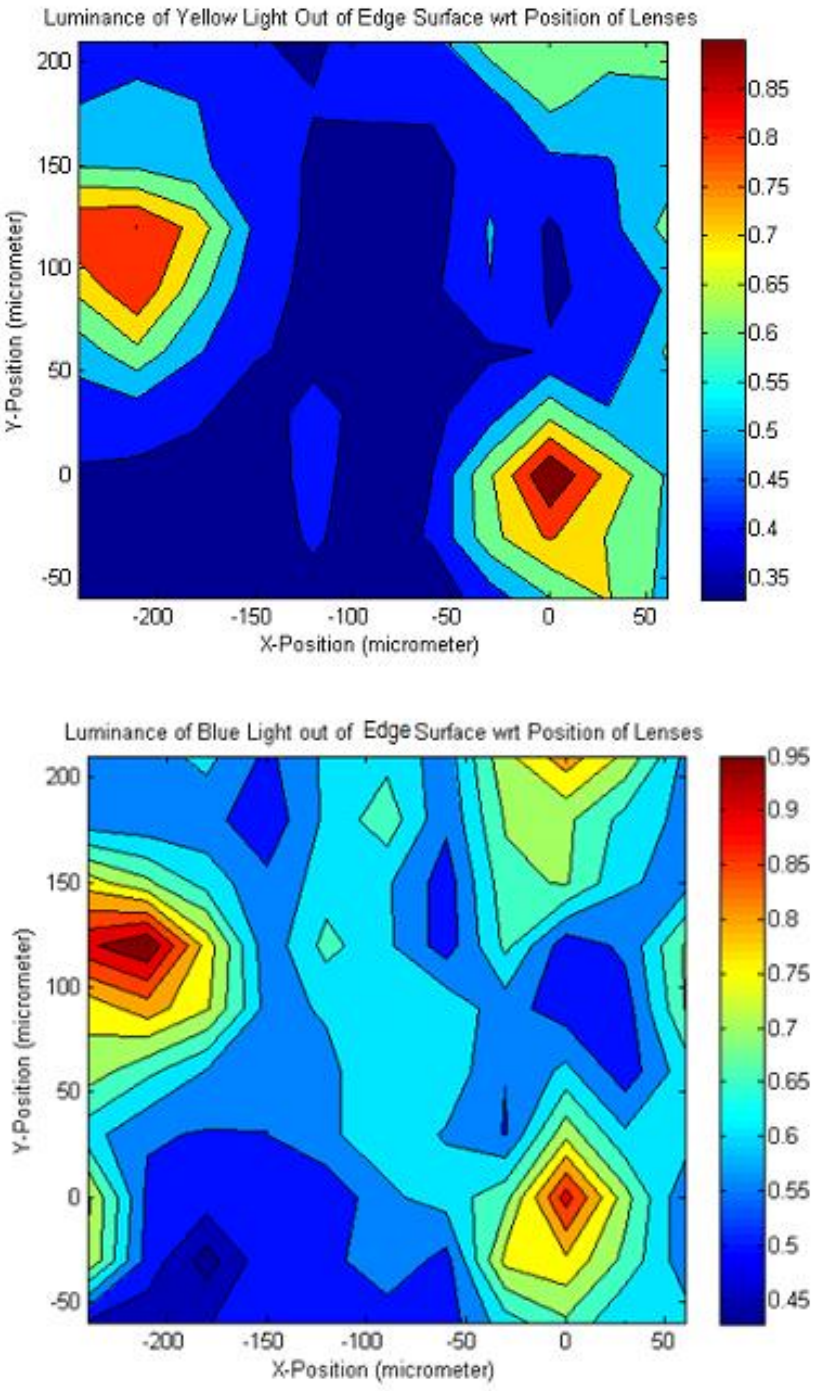

Figure 46: Luminance out of the edge surface of yellow light (top) and blue light (bottom).

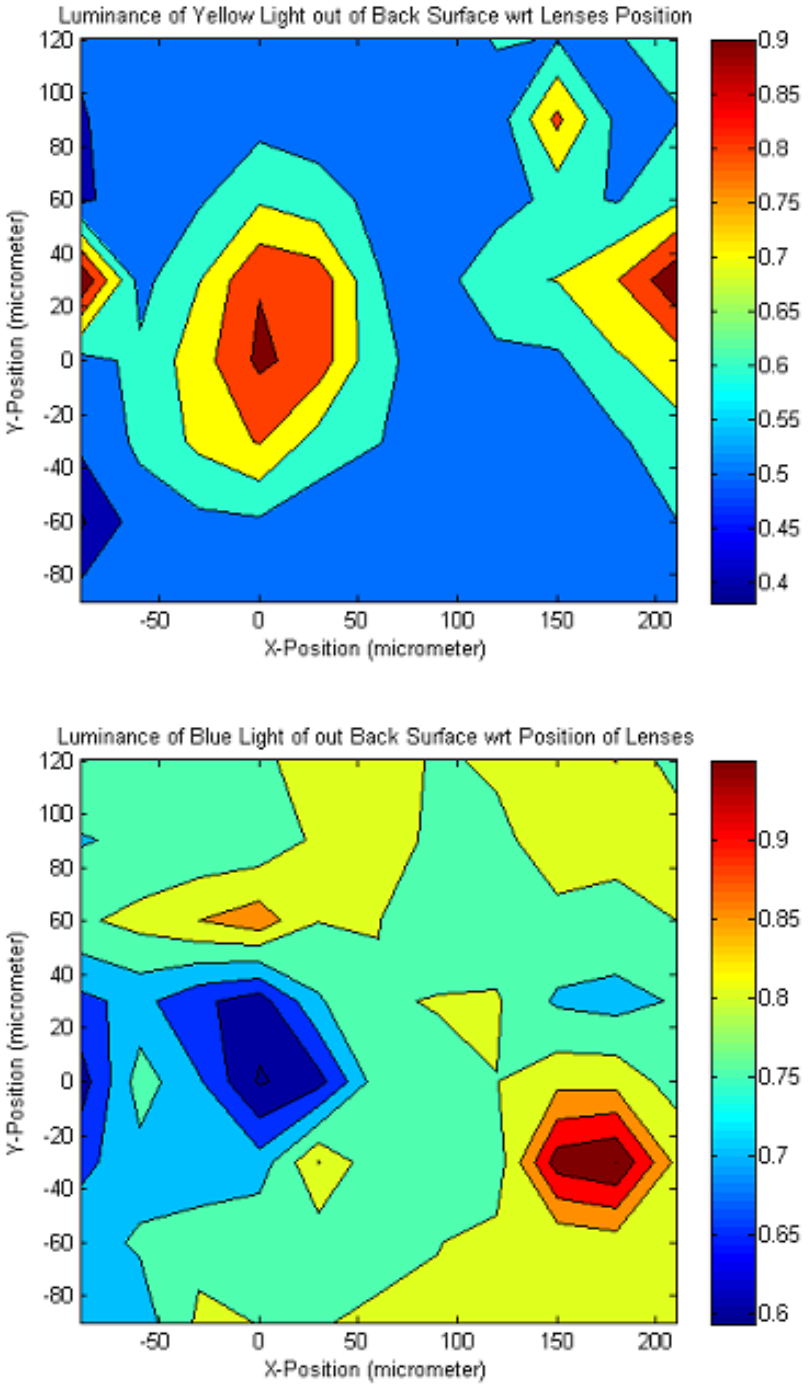

Figure 47: Luminance out of the back surface, yellow light (top), blue light (bottom).

When referring back to Figure 46, a relatively strong luminance (equivalent to the range of red to green-blue colour on the luminance scale) for yellow light is observed for a distance of approximately 800 µm, which is greater than the size of Ce:YAG (500 µm). Since the lenses are moved across the concentrator's surface, it follows that the LED's focal point would be translated across the fixed positions of Ce:YAG (size of 500 µm). When light from the LED was refracted through the surface of the lenses, a smaller mirror image of the LED would be produced at the focal length of the lenses. To determine the size of this LED image, simple geometry and optics rules were taken into account that yield a size of 234 µm, the details for this calculation are found in Appendix A.8: LED Image Size.

Essentially, the results obtained from the contour plots were fit by a convolution of a square function that correspond to Ce:YAG with a width of 500 µm and a Gaussian function with a full width half maximum (FWHM) equivalent to 234 µm that represents the LED light. A square function for Ce:YAG was chosen since the solidified mixture was contained within holes of a specific size (500 µm diameter), and the cerium content is consistent across this 500 µm range. Therefore, it follows that at any point blue light is shone on Ce:YAG, the same luminance should be observed across the entire range of the hole, containing the phosphor, without the presence of any lenses.

To determine what function would fit an LED profile, a separate experiment was conducted, where a blue LED was shone on a white piece of

paper and luminance measurements were taken across the entire diameter of the reflection of the LED. A maximum intensity was observed at the centre of the reflection and a minimum at the edges, where the detailed results can be found in Appendix A.9: Gaussian Distribution of LED. A Gaussian function fits this intensity distribution,

$$f(x) = a \cdot exp\left(-\frac{(x-b)^2}{2 \cdot c^2}\right) + d$$

Equation 23: Gaussian function for an LED, where a = 32.07, which is the height of the curve's peak, the center of the peak is denoted by b (= 0.25), c is the standard deviation which is equivalent to 0.0994, and finally, the y-intercept is d (which is 0 in this case) [65].

Figure 48 below shows the convolution of the two functions, which are consistent with the approximately 800 µm range of detected yellow light instead of strictly within the local island of 500 µm.

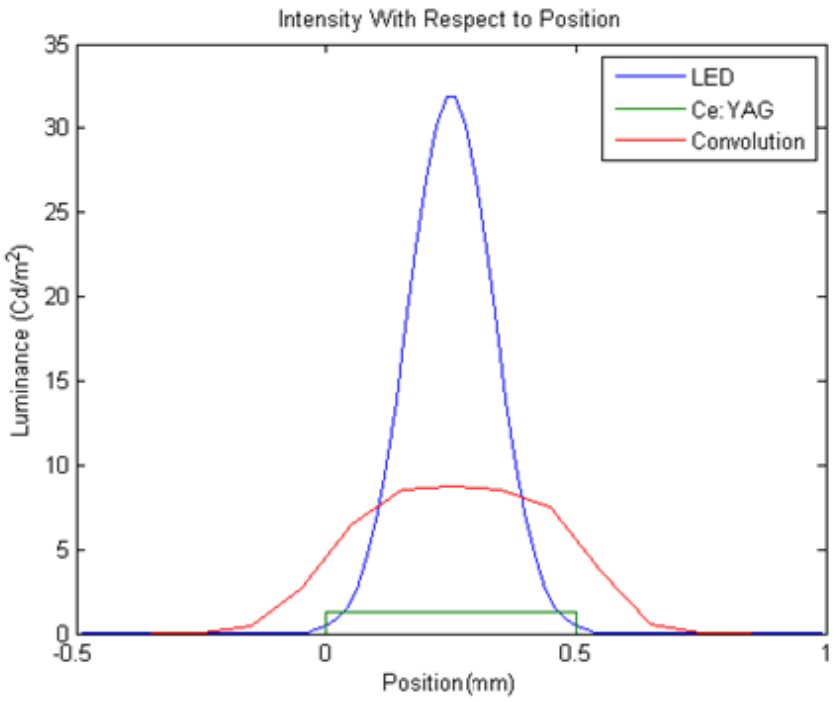

Figure 48: Convolution of Ce:YAG (square function) and LED (Gaussian distribution).

Although Figure 46 and Figure 47 conclude that there would always be yellow light waveguided to the edges, however, a strong luminance is only exhibited for lens positions within a radius of 430 µm from the optimal position, as indicated in Figure 48. Figure 49 illustrates at what time range throughout the day this concentrator would be efficient using simple geometry rules. The extent of the focal point position from optimal position was translated into angle, which in turn was correlated to the time of day through interpolation. The results determined that this concentrator is effective between 11:43 am and 12:16 pm.

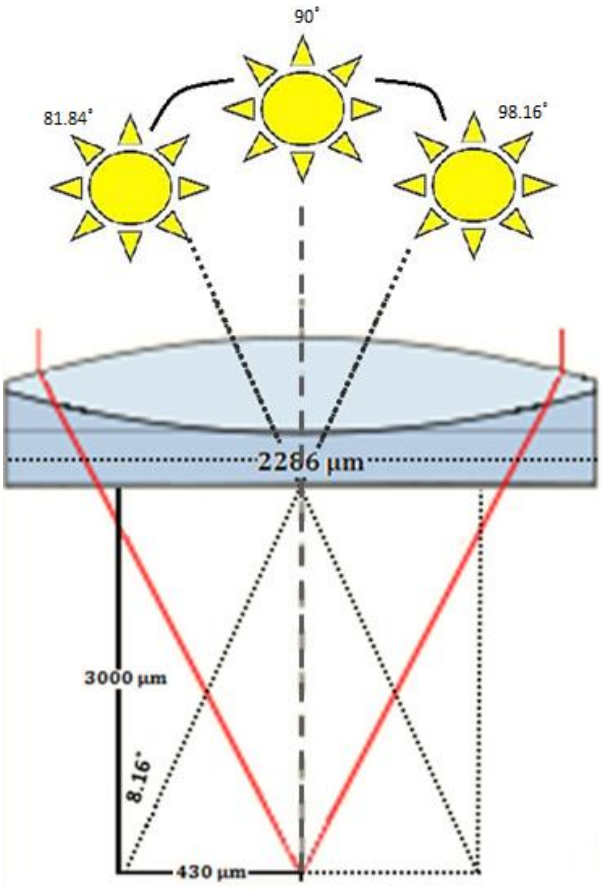

Figure 49: The focal point of rays as the sun moves across the sky.

7.3.2 Optical Power Calculations

When speaking in terms of solar cells, units of 'Watts' for power are most commonly used since the amount of light converted to electricity is of importance. In addition, the photometer's response is more sensitive to yellow light than blue, the luminance values were converted to power to account for the photometer's difference in spectral response. To convert 'luminance' (Cd/m^2) to 'power' (W), the following steps were taken:

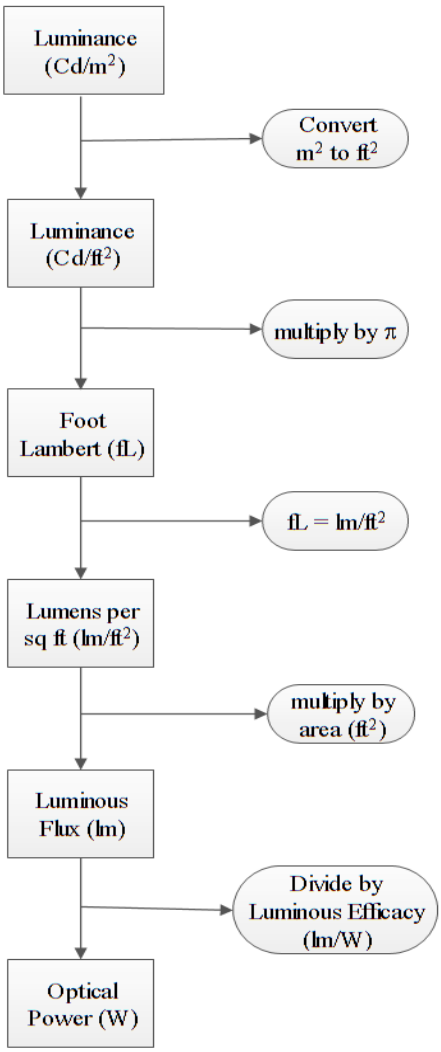

Figure 50: Converting flux measurements into optical power.

Dividing by luminous efficacy (how well a light source produces visible light) optical power is calculated. The calculation is shown in Appendix A.10: Luminous Efficacy, where a value of 60 lm/W was used for blue light and 575 lm/W was used for yellow light. The total efficiency was determined by dividing the measured value one of the concentrator surfaces by that of the Ce:YAG.

Results

Using the methodology to determine the overall optical power waveguided to the edges, explained in the previous section, it yielded a value of only 0.254 mW out of 0.783 mW of yellow light reaching the edges without the presence of lenses and 0.419 mW (with respect to an input power of 0.783 mW) with lenses. More yellow light is waveguided than blue for both without (0.216 mW vs 0.0376 mW) and with (0.213 mW vs 0.106 mW) lenses. This is indicative of how well Ce:YAG converts blue to yellow light and would definitely help improve the conversion efficiency for both Si and InGaP solar cells. Table 12 below shows the overall optical power for each colour with and without the presence of lenses, and the amount that is waveguided versus refracted out of the concentrator.

Table 12: Optical efficiency of waveguided and refracted out percentages of output power relative to input power.

	530 nm ≤ λ ≤ 600 nm		**λ ≤ 500 nm**	
	No Lenses	**Lenses**	**No Lenses**	**Lenses**
Input Power (mW)	0.783	0.783	0.783	0.783
Edge Surface (mW)	0.216	0.312	0.0376	0.106
Optical Efficiency (%)	27.65	39.93	4.80	13.61
Back Surface (mW)	0.0786	0.111	0.0755	0.0732
Refracted out (%)	10.04	14.14	9.65	9.35

7.4 Overall FSC Performance

7.4.1 Optical Efficiency

The product of the different loss mechanisms mentioned in section 2.2, determines the overall optical efficiency of the concentrator as indicated in Equation 4, where the value for each component was resolved for a 1.90x1.90x0.900 cm concentrator [6], [19], [66].

The term (1-R) indicates the amount of light transmitted into the concentrator after accounting for Fresnel reflection from the front surface of the FSC sheet, where R was computed through Equation 24. The reflection from the back surface was neglected here since it was adjusted for in the efficiency of total internal reflection.

$$R = \frac{(n-1)^2}{(n+1)^2}$$

Equation 24: Calculating reflectance using refractive index of the material.

The probability of total internal reflection (P_{TIR}) reveals the probability of emitted photons from the fluorescent material that would be internally trapped within the substrate and waveguided, i.e. the amount of light remaining after photons are lost into the escape cone fraction zone. As explained previously, this was determined using the critical angle, using Equation 25 or Equation 26:

$$P_{TIR} = 1 - \frac{I_{escape}}{I_{source}}$$

Equation 25: The probability for total internal reflection within the concentrator.

or, using the refractive index, P_{TIR} could also be calculated using

$$P_{TIR} = \frac{\sqrt{n^2 - 1}}{n}$$

Equation 26: The probability for internal reflection within the concentrator calculated using the refractive index.

Unlike the host efficiency, the efficiency of total internal reflection, η_{TIR}, refers to the effectiveness of total internal reflection without any scattering events due to the presence of any defects or foreign particles. This value was determined experimentally by measuring the amount of light that would be waveguided of an acrylic sample with an optical finish and compared to a sample that underwent the same grinding and polishing steps described in section 6. In addition, the luminance of congealed (using Sk-9 lens bond) and non-congealed powder, were measured and compared to determine how much light is absorbed in the adhesive. The loss is incorporated into the efficiency of total internal reflection parameter.

The terms, η_{abs} and η_{host}, refer to the absorption efficiency of the fluorescent material and the host efficiency of the substrate respectively for a wavelength ranges $450 \leq \lambda \leq 600$ nm (the LED Spectrum is found in Appendix A.11: LED Optical Power as a Function of Wavelength). Absorption efficiency is

a measure of how effectively the FM absorbs incoming photons and was therefore, determined by integrating the area under the absorption curve shown in Figure 20 and dividing by the input power. Similarly, the host efficiency demonstrates the capability of the waveguide to transmit photons to the edges without being absorbed (refer to Figure 55 found in Appendix A.12: Acrylic Transmission). Correspondingly, the host efficiency was computed by integrating under the absorption curve for an acrylic sample and dividing by the input power. The presence of lenses can only affect the absorption range of the Ce:YAG, since the substrate has very limited absorption (i.e., mostly transparent to all wavelengths). Equation 3 was used to determine what the concentration of light would be and the result is multiplied by $\eta_{abs.}$

The efficiency of the fluorescent quantum yield, η_{FQY}, refers to the ratio of number of photons emitted to the number of molecules excited as explained and determined in previous sections (4.1.2.3: Quantum Yield). Meanwhile, stokes efficiency,η_{stokes}, refers to the amount of energy remaining after the fluorescence process takes place and thermalization losses occur within the fluorescent material. Since the emitted photon is at a higher wavelength than that of the absorbed one, it follows that some energy is lost. It is therefore determined by,

$$\eta_{\text{stokes}} = \frac{e_{emitted}}{e_{absorbed}}$$

Equation 27: Stokes efficiency of fluorescent material: Ce:YAG.

Finally, self-absorption, η_{self}, applies to reabsorption of fluorescence. This parameter depends on the probability of fluorescence intersecting an absorption site (i.e. an island of Ce:YAG). Since those Ce:YAG sites have very specific locations, the probability of intersection can be calculated for a specific site. If emission from an island located right at the centre of the concentrator (s_o) was used as an example since it has the highest possible number of neighbouring absorption sites, the nearest neighbour sites form a spherical shell with a surface area of $4\pi r^2$ (refer to Figure 51).

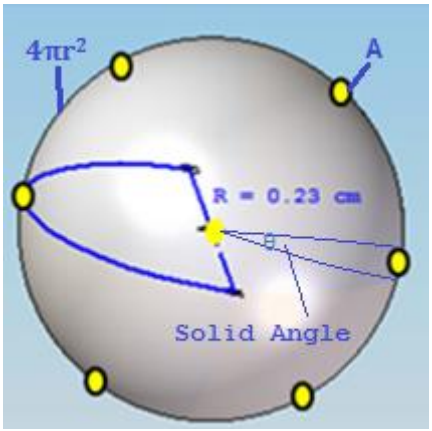

Figure 51: 6 nearest Ce:YAG neighbouring sites forming a spherical shell with area $4\pi r^2$ around site, s_o.

The probability of emission hitting a neighbouring island located at a distance r from s_o is

$$P(intersection) = \frac{A}{4\pi r^2} \cdot \#\ of\ sites$$

Equation 28: The probability of fluorescence intersecting an absorption site. Area of Ce:YAG site (A) located at distance, r, from a defined centre (i.e. s_o).

Results

Now that the optical properties of Ce:YAG and the concentrator have been determined, Equation 4 was used to approximate the overall efficiency of this concentrator of size 1.90x1.90x0.90 cm, where the detailed results are displayed below in Table 15. A value of 1.50 was used for the refractive index to calculate R and P_{TIR} in Equation 24 and Equation 25, which yield 0.04 and 0.745 respectively. Meanwhile, it was established that 7.90% of light was lost as a result of the polishing procedure in addition to the 2.30% absorbed by the lens bond resulting in 89.98% efficiency of total internal reflection (η_{TIR} = 0.977*0.921).

Integrating the area under the curve yielded an absorption efficiency of 87.68% and a host efficiency of 91.1%. As indicated above, Equation 3 was used to resolve what the factor for concentration of light will be, as shown below,

$$C_{geom} = \frac{\#\ of\ lenses \cdot area\ of\ lens}{\#\ of\ cells \cdot cell\ active\ area} = \frac{80 \cdot (2\pi r^2)}{2 \cdot l \cdot w} = \frac{80 \cdot \left(2\pi \left(\frac{0.2286}{2}\right)^2\right)}{2 \cdot (0.9\ x\ 1.9)}$$

$$= 1.92\ suns$$

In practice, measured concentration ratio is generally within the range of 2 – 10 suns [17], [67], which was reflected in the calculated C_{geom}, to 1.92 suns. Consequently, the presence of lenses theoretically increases the absorption efficiency by a factor of 1.92 to 168.34%. Stokes efficiency was resolved by determining how much energy remains after thermalization losses occur, i.e., 89.8% (η_{Stokes} = 2.34/2.60).

The probability of self-absorption depends strongly on the chosen centre of Ce:YAG site (i.e. its position within the concentrator), and consequently the number of neighbouring absorption sites. The more central this location is within the concentrator, the more likely fluorescence will be absorbed since there is a higher number of neighbouring local Ce:YAG islands (sites located towards the edge of the concentrator risk fluorescence to be refracted out of the concentrator). Using the Ce:YAG island (s_o) outlined in red in Figure 52 as a reference, the probability of intersection from the first 6 nearest neighbours at r1 is

$$P(itersection) = \frac{A}{4\pi r^2} \cdot \#\ of\ sites = \frac{0.5\ mm^2}{4\pi(2.3\ mm)^2} \cdot 6 = 0.022564$$

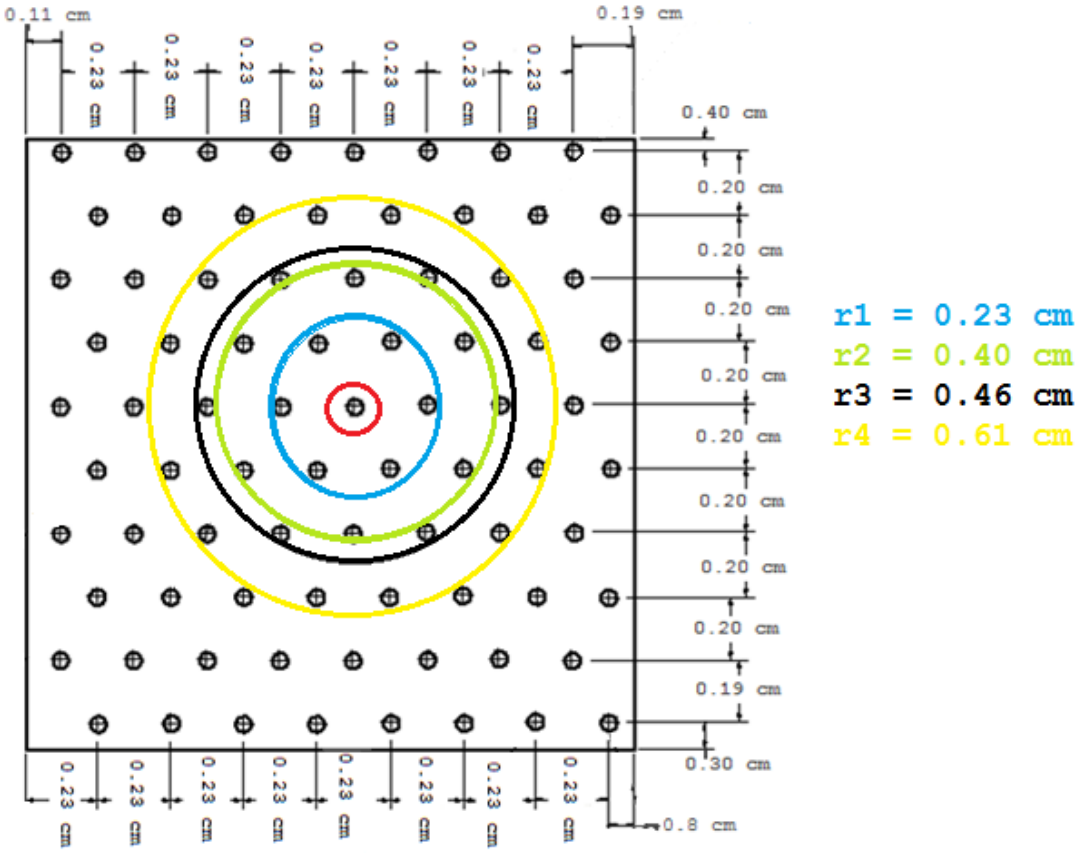

Figure 52: Outlining nearest neighbours for a central Ce:YAG site.

Table 13 outlines the probability of intersection for all absorption sites from s_o, with a total of 5.47% for all 79 sites in the prototype fabricated in section 6.3. The probability was anticipated to be low since the total Ce:YAG area within the concentrator accounts for only 4.35%, therefore there are very limited absorption sites in the first place. In addition, the absorption coefficient of yellow light at peak emission is only 1.57 cm^{-1} compared to 25.8 cm^{-1} at peak excitation of blue light, thus Ce:YAG has a very weak absorption capability of yellow light.

Table 13: Probability of intersection of local islands of Ce:YAG.

Radius (cm)	# of Sites	Probability (%)
r1 = 0.23	6	2.256
r2 = 0.40	6	0.0746
r3 = 0.46	6	0.0564
r4 = 0.61	12	0.0642
r5 = 0.69	6	0.0251
r6 = 0.79	10	0.0313
r7 = 0.832	8	0.0230
r8 = 0.92	5	0.0117
r9 = 1.003	8	0.0158
r10 = 1.056	6	0.0169
r11 = 1.15	2	0.0030
r12 = 1.219	3	0.0040
r13 = 1.28	1	0.0012
Total	**79**	**5.47**

Although the internal quantum yield was originally determined to be 80.0% previously, a value of 0.757 was indicated in Table 15 to account for reabsorption. If no reabsorption occurs, then the quantum yield remains at 80.00%. However, Figure 20 shows that at the yellow wavelength range, the intensity of the excitation level is very low compared to that of blue. Therefore, it

was assumed that the energy of the fluorescence is not high enough to excite electrons in the Ce atom in the first place and consequently, any fluorescence absorbed is lost. Since η_{self} was calculated to be 5.47%, it follows that there is a factor of 5.47% less photons emitted as a result of reabsorption events, therefore making a quantum yield of 75.7% instead of 80.0%.

7.4.2 Comparison

The experimental results for optical efficiency of the concentrator with respect to input power instead of total amount emitted by Ce:YAG are summarized in Table 14. Meanwhile the different components of optical efficiency as per Equation 4 are outlined in Table 15, where most of those values were obtained from previous experiments.

Table 14: Optical efficiency of concentrator with respect to input power.

	$\lambda \leq 500$ nm		**530 nm $\leq \lambda \leq$ 600 nm**		**$\lambda \leq 600$ nm**	
	No Lenses	**Lenses**	**No Lenses**	**Lenses**	**No Lenses**	**Lenses**
Edge Surface (%)	4.80	13.60	27.65	39.99	32.46	53.53
Back Surface (%)	9.65	9.35	10.04	14.14	19.70	23.49

Table 15: Optical efficiency calculated using the product of different loss mechanisms.

Quantity	Value for No Lenses	Value for Lenses
1-R	0.96	0.96
P_{TIR}	0.745	0.745
η_{abs}	0.877	1.683
η_{FQY}	0.756	0.756
η_{Stokes}	0.898	0.898
η_{host}	0.911	0.911
η_{TIR}	0.8998	0.8998
$1-\eta_{self}$	0.945	0.945
η_{Opt}	**0.3299**	**0.6333**

When the results for both spectral ranges in Table 14 were combined, the optical efficiency of the concentrator was 32.46% (without lenses) and 53.53% (with lenses), whereas the calculated optical efficiency from Table 15 yielded 32.99% and 63.3% without and with lenses, respectively. There are two main reasons that could explain this discrepancy, with regards to the results for the case with lenses. Firstly, the Ce:YAG islands are made of congealed powder instead of a perfect single crystal. Light will always scatter when interacting with a powder material, therefore causing some light to be lost. Secondly, the refractive index of Ce:YAG is 1.83 while acrylic is only 1.5. Since the fluorescent material has a

higher refractive index, it leads to some light being trapped within those local islands as explained previously through Snell's Law.

The dominant factors that caused a decrease in optical efficiency came from P_{TIR}, η_{FQY} and $\eta_{abs.}$ These parameters must be improved to achieve higher efficiencies. The main loss associated with P_{TIR} is the escape cone fraction, which is mainly dependent on the refractive index of the substrate. There are some methods that can be applied to capture this loss and direct them back into the concentrator such as mirrors and antireflection coatings, or using a substrate with a higher refractive index to reduce the escape cone fraction. The presence of lenses improved the absorption efficiency by a factor of 1.92, from 87.68% to 168.3%. The only other way to overcome this issue is to use multiple fluorophores that absorb different regions of the spectrum. However, increasing this absorption range can lead to a decrease in η_{stokes}, since it would lead to a larger difference between absorption and emission (large Stokes Shift), thereby limiting the degree to which η_{abs} could be improved by. Although η_{TIR} is not as low as the other efficiencies, it still has the potential to improve by modifying the fabrication technique to achieve a better optical finish. This can include using new and different grades of polishing cloths (so that debris from other samples and materials do not get trapped in the waveguide) and perhaps polishing for a longer period of time. Also, heat treatment processes could be implemented so that the acrylic is heated sufficiently to create material flow, thereby resulting in a

smoother finish. η_{FQY} and η_{Stokes} cannot be improved since they are an inherent property of the fluorescent material.

The overall performance of the FSC is displayed in Table 16 with both silicon and indium gallium phosphide solar cell at the edges. Since essentially the light waveguided to the edges has an approximate energy of 2.34 eV, which is higher than either of the materials' band gaps, the thermalization losses are equivalent to 52.99% for silicon and 27.35% for indium gallium phosphide. When calculating the overall efficiency of the fluorescent concentrator, only the Stokes shift limitations between the energy of the emitted photons and the bandgap of solar cell material were investigated.

Analysing those results in Table 16 shows that when using either silicon or indium gallium phosphide, the efficiency of this concentrator is higher than the typical range of reported efficiencies for FSCs (refer to Table 1), and even higher than the current reported highest efficiency (7.1%) [6].

Table 16: Overall FSC efficiencies, using InGaP and Si as edge solar cells.

Solar Cell	**Indium Gallium Phosphide**		**Silicon**	
	No Lenses	**Lenses**	**No Lenses**	**Lenses**
η_{Opt} (%)	32.99	63.33	32.99	63.33
1-η_{Therm} (%)	72.65	72.65	47.43	47.43
η_{FSC} (%)	23.96	46.01	15.51	29.77

8 Conclusions & Future Work

8.1 Summary

This work involved using third-generation photovoltaics concentrator concept to achieve higher efficiencies at lower costs. Fluorescent solar concentrators (FSCs) consist of a fluorescent material embedded in a substrate that absorbs light at a specific wavelength and emits it at another, which is then concentrated along the edges to be absorbed by the solar cells attached at the edges. FSCs offer cost reduction by decreasing the required active solar cell area and incorporating them into buildings to offset installation costs. The fluorescent material used in this design is required to have a large absorption range and fluoresce at an energy equivalent to the solar cell's band gap to minimize thermalization losses. In addition, it must be highly stable in order to withstand all the energy absorbed and have a high quantum yield. For those reasons, this research focused on investigating Ce:YAG as a suitable fluorescent material as well as enhancing the optical transport of fluorescence to the solar cell, specifically for either a silicon or an indium gallium phosphide solar cell.

8.1.1 Characterizing Ce:YAG

Ce:YAG was not fabricated or grown throughout the course of this project, instead, a cerium doping level of 0.180 mol% single crystal and powder sample

were purchased from Scientific Materials Corporation and Phosphor Technology. Preliminary analysis including a physical, chemical and optical analysis was conducted on a 0.926x0.924x0.214 cm sample to characterize its properties. X-ray analysis was used to determine a body-centred cubic crystal structure, '$Ia\bar{3}d$', a preferred orientation of <111>, a lattice constant of 12.004 Å and a density of 4.56 g/cm^3. Phase analysis showed no evidence of additional phases in the powder sample which is indicative of the high-quality of the sample.

Optical characterization of Ce:YAG generated the absorption, emission and transmission profile for this material for any given wavelength. A peak excitation was detected at 476 nm with an absorption coefficient of 25.8 cm^{-1} and a peak emission at 530 nm with an absorption coefficient of 1.57 cm^{-1}. Using the results of the absorption coefficient for any given wavelength, the transmission profile was modelled by varying the thickness of the Ce:YAG using Beer-Lambert's Law. It was deduced that a thickness of 0.050 cm provided the best balance between the absorption of blue light and transmission of yellow light, which yielded 65% and 90%, respectively. TCSPC measured a fluorescence lifetime of 62.3 ns, which falls within the reported values of 60.0 – 67.0 ns. Meanwhile, an Ocean Optics spectrometer measured the EQE to be 67.6% and 80.0% for IQE, which is typically less than the reported values.

An initial analysis was conducted to ascertain the feasibility of using Ce:YAG as a fluorescent material by determining the amount of light waveguided towards the solar cell and the cost of using this material, which yielded very poor

results. Only 23.4% reaches the edges at a cost of $5 688.87 - $15 974.17 for a sheet of 1.00 m^2 with a thickness of 0.050 cm Ce:YAG. This outcome was the cause of motivation for a new design consisting of a spatially patterned Ce:YAG arrangement of 500 µm diameter and thickness embedded at a distance of 0.30 cm from the top surface of the concentrator. A lens sheet was placed on top of the concentrator to concentrate light onto these local islands of Ce:YAG to provide a strong sunlight coupling. The waveguided portion of fluorescence in addition to the cost of Ce:YAG for this new design was calculated to be 75.46% and $3.74 – $10.51, which is a substantial improvement over the old design. A prototype made of acrylic with local islands of Ce:YAG was successfully fabricated to a final size of 1.90x1.90x0.90 cm.

8.1.2 Concentrator Analysis

Before carrying out experimental procedures, the fluorescent concentrator was first analysed theoretically through modelling techniques, using Optics Lab, a ray tracing software, and Monte Carlo simulations. Both of those analyses were initialized after Ce:YAG fluoresces to determine how much light is waveguided towards the edges, therefore the results were normalized to 100% emitted from Ce:YAG. Two main assumptions were made to carry out these simulations, (1) only blue light is absorbed by Ce:YAG and is effectively converted to yellow (i.e. conversion efficiency is 100%), and (2) no reabsorption of fluorescence occurs. This was mainly done due to the limitations of Optics Lab software which does

not model absorption effects. The same assumptions were applied to MCS so that the results between the two would be comparable. In addition, from the absorption profile obtained earlier, the absorption coefficient for yellow light was only 1.57 cm^{-1}, which is only a fraction of the capability for this material to absorb blue (25.8 cm^{-1}) light, thereby, validating these assumptions. Optics Lab and MCS yielded 56.10% and 59.20% waveguided to the edges, while 43.90% and 40.80% of light was refracted out of the device, respectively, and lost to the environment.

A photometer was used to measure luminance out of the edge and back surfaces of the fabricated prototype both with and without the presence of lenses. Filters were used to determine the exact amount of either blue or yellow light actually being measured. Three sets of results were obtained for this measurement, where the first one was normalized to 100% emitted by the Ce:YAG, so that it could be compared to the simulation results. Those outcomes yielded a total of 57.14% and 58.22% of both blue and yellow light waveguided towards the edges, with out and with the presence of lenses, respectively, whereas 42.86% (with lenses) and 41.77% (without lenses) was refracted out of the concentrator which con coincided with the simulated results.

Next, the amount waveguided with respect to input power was measured for each colour. Those results yielded that only 27.65% (no lenses) and 39.93% (with lenses) of yellow light is waveguided, while 4.80% (no lenses) and 13.61% (lenses) of blue light is waveguided. Regardless, a total of 67.54% (without lenses) and 46.47% (lenses) of light was refracted out of the device. Since much

more yellow light is waveguided compared to blue, those results are indicative of the high conversion efficiency of Ce:YAG.

The third set of measurements consisted of varying the lenses position with respect to the location of the islands of Ce:YAG. This experiment was conducted to gain a better understanding of the efficiency of this concentrator design if light was not focused perfectly onto Ce:YAG, since the sun constantly moves across the sky and would not always be situated perpendicular to the lenses. The results determined that regardless of the lens position with respect to Ce:YAG, yellow light would always be detected and either waveguided to the edges or refracted out of the device. As expected, a positive correlation between blue and yellow was observed when luminance was measured out of the edge surface, i.e. a maximum luminance of yellow light showed also a maximum luminance for blue light, and vice versa. This was anticipated since essentially the light emitted from the Ce:YAG was supposed to be measured as opposed to the transmitted incident power. The opposite effect was observed out of the back surface, meaning a negative correlation between the yellow and blue light was detected. Once again, this was predicted since at optimal positions, most of the blue light should have been absorbed and converted to yellow. Therefore, there should be a much weaker luminance of blue light at those positions. In contrast, at non-optimal positions there is theoretically little or no cerium to convert those blue photons to yellow, thereby maximizing the transmission of blue light. This experiment concluded

that this concentrator with this design would be only efficient between the hours of 11:43 am to 12:17 pm.

Finally, the overall fluorescent concentrator efficiency was computed by determining the optical efficiency first. This was done by isolating its individual parameters, and obtaining each one experimentally and comparing the product to the measured optical efficiency of the concentrator (from the measured output power with respect to input power). A total output power of 0.770 mW was measured with respect to an input power of 0.783 mW for lenses. This was a result of lenses theoretically increasing the absorption efficiency by a factor of approximately 1.92 to 168.34%. The assumption made earlier during simulations that no reabsorption occurs was somewhat validated in this section, since it was calculated that the probability for intersecting an absorption site in the first place was only 5.47%. In addition, the absorption efficiency of yellow light is quite low compared to blue light. The second and third largest loss mechanisms came from the probability of total internal reflection and the fluorescence quantum yield efficiency, which were 74.5% and 75.6%, respectively. The η_{FQY} decreases due to reabsorption losses, since there would be a factor of 5.47% less fluoresced photons absorbed. The overall optical efficiency was calculated to be 32.99% without lenses and 63.33% with lenses. Experimentally, optical efficiency was measured to be 32.46% (without lenses) and 53.53% (lenses).

8.2 Future Research

To improve the optical efficiency for this concentrator, the fabrication technique must be improved. One way of achieving this is to use substrates with higher refractive indices (~1.80) to reduce the amount of light that could be trapped within the holes, in addition to reducing the escape cone fraction into the environment (i.e. P_{TIR} increases). Another mechanism is to improve the fabrication technique in order to reduce losses arising from the η_{TIR} term. This can be accomplished through using optically finished substrates, free of any damages or foreign particles. Also, potentially highly polished single crystals (with a volume of 1.25×10^{-4} m^3) could be used instead of powder to reduce scattering effects.

This project was concluded without applying any solar cells to the edges. A theoretical calculation was made based on thermalization losses between incoming photons from the fluorescent material to silicon or indium gallium phosphide solar cells. The $1-\eta_{therm}$ term is the maximum possible efficiency that would be exhibited by the solar cells, but not what is available today in practice. The theoretical calculations yield higher efficiencies than the typically reported ones for both silicon and InGaP. In addition, GaInP's bandgap can be tuned depending on the indium content, where decreasing In increases its bandgap. Therefore, it would be more useful if this cell was fabricated to increase its

bandgap such that it matches the incoming energy from Ce:YAG, and thereby reducing thermalization losses.

9 References

[1] e. a. A. Adegbululgbe, "Energy Supply," Cambridge University Press, Cambridge, 2007.

[2] David, "Solar Power - Advantages and Disadvantages," 2008. [Online]. Available: http://alternate-power.org/solar-power-advantages-and-disadvantages/. [Accessed October 2012].

[3] "High Efficiency Solar Cells," PV Education, [Online]. Available: http://www.pveducation.org/pvcdrom/manufacturing/high-efficiency.

[4] V. Sark, "Luminescent Solar Concentrators," *Renewable Energy,* vol. 2013, no. 49, pp. 207 - 210, 2012.

[5] V. Sholin, J. Olson and S. Carter, "Semiconducting polymers and quantum dots in luminescent solar concentrators for solar energy harvesting," Santa Cruz, 2007.

[6] M. Debije and P. Verbunt, "Thirty years of luminescent solar concentrators reasearch: solar energy built for the environment," *Advanced Energy Materials,* 2012.

[7] K. McIntosh, N. Yamada and B. Richards, "Theoretical comparison of cylindrical and square-planar luminescent solar concentrators," *Applied Physics B: Lasers & Optics*, vol. 88, no. 2, pp. 285-290, 2007.

[8] E. v. d. Kolk and J. Wiegman, "Building integrated thin film luminescent solar concentrators: Detailed efficiency characterization and light transport modelling," *Solar Energy Materials and Solar Cells,* vol. 103, pp. 41-47, 2012.

[9] J. Batchelder, *The luminescent solar concentrator,* Pasadena, California, 1982.

[10] M. Currie, "Fabrication of a luminescent solar concentrator that minimizes self-absorption losses using inter-chromophore energy transfer," 2007.

[11] J. Lambe and W. Weber, "Luminescent greenhouse collector for solar radiation," *Applied Optics,* vol. 15, no. 10, pp. 2299 - 2300, 1976.

[12] A. Pelegrini, *Refractive integrated nonimaging solar collectors,* Uxbridge, 2009.

[13] B. Rowan, L. Wilson and B. Richards, "Advanced materials concepts for luminescent solar concentrators," *Journal of Selected Topics in Quantum*

Electronics, vol. 14, no. 5, pp. 1312 - 1323, 2008.

[14] M. Baldo, *Luminescent solar concentrators explained,* Cambridge, Massachusetts, 2009.

[15] C. Honsberg and S. Bowden, "Light Trapping," PV Education, [Online]. Available: http://pveducation.org/pvcdrom/design/light-trapping.. [Accessed October 2012].

[16] E. Yablonovitch, "Thermodynamics of the fluorescent planar concentrator," *Journal of Optical Society of America,* vol. 70, no. 11, pp. 1362-1363, 1980.

[17] G. Smestad, H. Ries and E. Yablonovitch, "The thermodynamics limits of light concentrator," *Solar Energy Materials,* vol. 21, pp. 99 - 111, 1990.

[18] "Concentrator optics," Power from the Sun, [Online]. Available: http://www.powerfromthesun.net/Book/chapter08/chapter08.html#8.1 Why Concentration?.

[19] W. van Sark, "Luminescent solar concentrators - a low cost photovoltaics alternative," *Renewable Energy,* vol. 49, pp. 207 - 210, 2013.

[20] D. Farrell and M. Yoshida, "Operating regimes for second generation luminescent solar concentrators," *Progress in Photovoltaics: Research and Applications,* vol. 20, pp. 93 - 99, 2012.

[21] B. S. Richards and K. R. McIntosh, "Ray-tracing simulations of luminescent solar concentrators containing multiple luminescent species," in *21st European Photovoltaic Solar Energy Conference,* Dresden, Germany, 2006.

[22] "Stokes Shift," AbD SeroTec, [Online]. Available: http://www.abdserotec.com/resources/flow-cytometry-ebook/principles-of-fluorescence/stokes-shift.html. [Accessed November 2012].

[23] B. Herman, J. R. Lakwicz, D. B. Murphy, T. J. Fellers and M. W. Davidson, "Fluorescence excitation and emission fundamentals," Olympus FluoView Resource, 2009. [Online]. Available: http://www.olympusfluoview.com/theory/fluoroexciteemit.html.

[24] A. M. Hermann, "Luminescent Solar Concentrators - A Review," *Solar Energy,* vol. 29, no. 4, pp. 323 - 329, 1982.

[25] S. Chandra, M. Kennedy, J. Doran, S. McCormack and A. Chatten, "Enhanced quantum dot emission for luminescent solar concentrators using plasmonic interaction," *Solar Energy Materials & Solar Cells,* pp. 1 - 6, 2011.

[26] B. Fisher and J. Bidde, "Luminescent spectral splitting: Efficient spatial division of solar spectrum at low concentration," *Solar Energy Materials and Solar Cells,* vol. 95, no. 7, pp. 1741 - 1755, 2011.

[27] R. Inman, G. Shcherbatyuk, D. Medvedko, A. Gopinathan and S. Ghosh, "Cylindrical luminescent solar concentrators with near infra-red quantum dots," *Optics Express,* vol. 19, no. 24, 2011.

[28] "Solar Technology," New Solar Inc, [Online]. Available: http://www.newsolarinc.com/solartechnology.php.

[29] "III-V Multijunction Materials and Devices R&D," National Renewable Energy Laboratory, May 2012. [Online]. Available: http://www.nrel.gov/pv/multijunction.html.

[30] "Silicon Materials and Devices R&D," National Renewable Energy Laboratory, April 2012. [Online]. Available: http://www.nrel.gov/pv/silicon_materials_devices.html.

[31] "Solar efficiency limits," Solar Cell Central, [Online]. Available: http://solarcellcentral.com/limits_page.html.

[32] O. Semonin, J. M. Luther and M. C. Beard, "Multiple exciton generation in a quantum dot solar cell," SPIE, 2014. [Online]. Available: http://spie.org/x86511.xml.

[33] "Luminescent down shifting," Scottish Institute for Solar Energy Research, [Online]. Available: http://siser.eps.hw.ac.uk/research/next-generation/luminescent-down-shifting.

[34] B. S. Richards, "Luminescent layers for enhanced silicon solar cell performance: down-conversion," *Solar Energy Materials and Solar Cells,* vol. 90, no. 9, pp. 1189 - 1207, 2006.

[35] W. W. Piper, J. A. DeLuca and F. S. Ham, "Cascade fluorescent decay in Pr3+ doped fluorides," *Journal of Luminescence,* vol. 8, no. 4, pp. 344 - 348, 1974.

[36] V. D. Rodriguez, V. K. Tikhomirov, J. Mendez-Ramos, A. C. Yanes and V. V. Moshchalkov, "Towards broad range and highly efficient down-conversion of solar spectrum by Er3+-Yb3+ co-doped nano-structured glass-ceramics," *Solar Energy Materials and Solar Cells ,* vol. 94, pp. 1612 - 1617, 2010.

[37] H. Lin, D. Chen, Y. Yu, Z. Shan, P. Huang, A. Yang and Y. Wang, "Broadband UV excitable near-infrared downconversion luminescence in Eu2+/Yb3+:CaF2 nanocrystals embedded in glass ceramics," *Journal of*

Alloys and Compounds, vol. 509, pp. 3363 - 3366, 2011.

[38] J. Li, Y. Zalloum, T. Roschuk, C. L. Heng, J. Wojcik and P. Mascher, "Light emission from rare-earth doped silicon nanostructures," *Advances in Optical Technologies,* vol. 10, pp. 295 - 601, 2008.

[39] J. Sacks, "Spectral engineering via silicon nanocrystals grown by ECR-PECVD for photovoltaic applications," Hamilton, 2012.

[40] Z. Y. Liu, S. Liu, K. Wang and X. B. Luo, "Optical analysis of colour distribution in white LEDs with various packaging methods," *IEEE Photonics Technology Letters,* vol. 24, no. 21, pp. 2027 - 2029, 2008.

[41] Z. Y. Liu, S. Liu, K. Wang and X. B. Luo, "Status and prospects for phosphor-based white LED packaging," *Frontiers of Optoelectronics in China,* vol. 2, no. 2, pp. 119 - 140, 2009.

[42] C. C. Lin, Y. S. Zheng, H. Y. Chen, C. H. Ruan, G. W. Xiao and R. S. Liu, "Improving optical properties of white LED fabricated by a blue chip with yellow/red phosphors," *Journal of the Electrochemical Society,* vol. 157, no. 9, pp. 900 - 903, 2010.

[43] G. Blasse and A. Bril, "A new phosphor for flyingspot cathoderay tubes for colour television: yellow-emitting Y3Al5O12Ce3+," *Applied Physics Letters,* vol. 11, no. 2, pp. 53 - 54, 1967.

[44] T. Mesli, "Improvement of ultra-high-brightness white LEDs," in *Manufacturing LEDS for Lighting and Displays,* Berlin, 2007.

[45] S. C. Allen and A. J. Steckl, "A nearly ideal phosphor-converted white light-emitting diode," *Applied Physics Letters,* vol. 92, 2008.

[46] V. K. Pecharsky and P. Y. Zavalij, Fundamentals of powder diffraction and structural characterization of materials, New York: Springer Science+Business Media, Inc., 2005.

[47] [Online]. Available: http://cnx.org/content/m38321/latest/Spec.jpg.

[48] J. Clark, "The Beer-Lambert Law," 2007. [Online]. Available: http://www.chemguide.co.uk/analysis/uvvisible/beerlambert.html.

[49] E. Zych, C. Brecher and J. Glodo, "Kinetics of cerium emission in a YAG:Ce single crystal: the role of traps," *Journal of Physics: Condensed Matter,* vol. 12, no. 8, 1947.

[50] *Temperature quenching of the yellow Ce3+ luminescence in YAG:Ce,* pp. 87 - 107.

[51] "Reference solar spectral irradiance : air mass 1.5," American Society for Testing and Materials (ASTM) Terrestrial Reference Spectra for Photovoltaic Performance Evaluation, [Online]. Available: http://rredc.nrel.gov/solar/spectra/am1.5/.

[52] J. V. Foreman, H. O. Everitt, J. Yang and J. Liu, "Influence of temperature and photoexcitation density on the quantum efficiency of defect emission in ZnO powders," *Applied Physics Letters*, vol. 91, no. 1, 2007.

[53] J. Silver, R. Withnall, J. Rose, N. Wilstead, G. Fern, S. Bishton, D. Klein, B. Rhodes, C. Barclay and Whitmarsh, "Broad-band green phosphor screens as a light source for head up displays in moving platforms," in *Optical Sensing and Spectroscopy*, Dublin, 2005.

[54] Optical Ray Tracing Software, [Online]. Available: http://www.optics-lab.com/index.html.

[55] S. Mark and S. Mordechai, Eds., in *Applications of mote carlo method in science and engineering*, Janeza Trdine, Rijeka, 2011.

[56] A. A. Earp, G. B. Smith, P. D. Swift and J. Franklin, "Maximizing the light output of a luminescent solar concentrator," *Solar Energy*, vol. 76, pp. 655 - 667, 2004.

[57] C. Manfredotti and M. Meliga, "Monte Carlo simulation of solar cells," *Solar Cells*, vol. 10, pp. 211 - 222, 1983.

[58] A. Schueler, A. Kostro, B. Huriet, C. Galande and J. Scartezzini, "Monte Carlo simulations of quantum dot solar concentrators: ray-tracing based on fluorescence mapping," in *Optics and Photonics*, San Diego, 2008.

[59] M. Kennedy, S. J. McCormack, J. Doran and B. Norton, "Modelling the effect of device geometry on concentration ratios of quantum dot solar concentrators," in *Proceedings of ISES World Congress*, 2007.

[60] Alpha Aesar, [Online]. Available: http://www.alfa.com/.

[61] MTI Corporation, [Online]. Available: http://www.mtixtl.com/.

[62] "Materials AeroView 70," Stewart Filmscreen, 2014. [Online]. Available: http://www.stewartfilmscreen.com/materials/rear-projection/aeroview-70.

[63] "UV Curing," Summers Optical: Optical Cements, [Online]. Available: https://www.optical-cement.com/cements/cements/uv.html.

[64] "Surface tension and bubbles," Surface Tension, [Online]. Available: http://hyperphysics.phy-astr.gsu.edu/hbase/surten2.html.

[65] J. Stewart, Calculus Early Transcendentals, 5 ed., Thomson, 2006.

[66] L. R. Wilson, *Luminescent solar concentrators: a study of optical properties, reabsorption and device optimization*, Edinburgh, 2010.

[67] R. M. Swanson, "Photovoltaic Concentrators," SunPower Corporation , [Online]. Available: http://www.kepu.dicp.ac.cn/photo/07sl02/Handbook%20of%20Photovoltaic%20Science%20and%20Engineering/11.%20Photovoltaic%20Concentrators.pdf.

[68] S. McDowall, T. Butler, E. Bain, K. Scharnhorst and D. Patrick, "Comprehensive analysis of escape-cone losses from luminescent waveguides".

[69] E. F. Schubert, Light-Emitting Diodes, Cambridge: Cambridge University Press, 2006.

[70] F. L. Pedrotti, L. M. Pedrotti and L. S. Pedrotti, Introduction to Optics, Pearson Education Limited, 2006.

Appendix

A.1. Escape Cone Fraction Derivation

The derivation for escape cone fraction for a concentrator with rectangular prism geometry [68]:

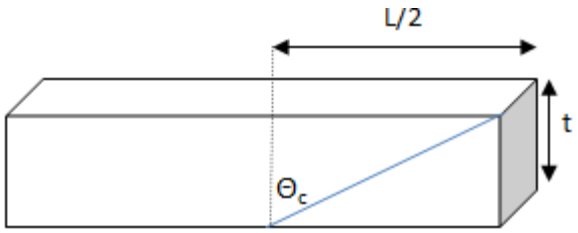

Figure 53: Escape cone fraction for a rectangular prism geometry

$$\frac{I_{escape}}{I_{source}} = \frac{\int_{\theta_o}^{\theta_c} A\, dA}{A} = \frac{\int_{\theta_o}^{\theta_c} \frac{tl}{2}\, \sin\theta\, d\theta}{tl} = \frac{\frac{tl}{2}\,(1 - \cos\theta)|_{\theta_o}^{\theta_c}}{tl} = \frac{1}{2}\,(1 - \cos\theta)|_{\theta_o}^{\theta_c}$$

A.2. Geometric Ratio for Cylindrical Design

The higher geometric concentration ratio of a cylindrical FSC to a planar FSC was derived as follows [7]:

$$G_{cyl} = \frac{2RL}{2\pi R^2} = \frac{L}{\pi R}$$

And

$$G_{sq} = \frac{L^2}{4LW} = \frac{L}{4W}$$

From Equation 6, the relationship between G_{cyl}/G_{sq} can be determined by assuming that the volume of the host material is equal for both. It follows that that the relationship between R and W would be

$$R = \frac{2W}{\pi}$$

Therefore,

$$G_{cyl} = \frac{L}{2W} = 2G_{sq}$$

A.3. Quantum Yield

A.3.1. Sphere's Response ($R_s(\lambda)$):

Table 17: Integrating sphere's spectral response [39].

Wavelength (nm)	Integrating Sphere IRF	Wavelength (nm)	Integrating Sphere IRF	Wavelength (nm)	Integrating Sphere IRF
200	1.69E-04	470	5.01E-04	**740**	5.53E-04
210	1.69E-04	480	5.01E-04	**750**	5.53E-04
220	1.69E-04	490	5.01E-04	**760**	5.53E-04
230	1.69E-04	500	5.26E-04	**770**	5.53E-04
240	1.69E-04	510	5.26E-04	**780**	5.53E-04
250	1.69E-04	520	5.26E-04	**790**	5.53E-04
260	1.69E-04	530	5.26E-04	**800**	5.26E-04
270	1.69E-04	540	5.26E-04	**810**	5.26E-04
280	1.69E-04	550	5.26E-04	**820**	5.26E-04
290	1.69E-04	560	5.26E-04	**830**	5.26E-04
300	4.05E-04	570	5.26E-04	**840**	5.26E-04
310	4.05E-04	580	5.26E-04	**850**	5.26E-04
320	4.05E-04	**590**	5.26E-04	**860**	5.26E-04
330	4.05E-04	**600**	5.53E-04	**870**	5.26E-04
340	4.05E-04	**610**	5.53E-04	**880**	5.26E-04
350	4.05E-04	**620**	5.53E-04	**890**	5.26E-04
360	4.05E-04	**630**	5.53E-04	**900**	5.26E-04
370	4.05E-04	**640**	5.53E-04	**910**	5.26E-04
380	4.05E-04	**650**	5.53E-04	**920**	5.26E-04
390	4.05E-04	**660**	5.53E-04	**930**	5.26E-04
400	5.01E-04	**670**	5.53E-04	**940**	5.26E-04
410	5.01E-04	**680**	5.53E-04	**950**	5.26E-04
420	5.01E-04	**690**	5.53E-04	**960**	5.26E-04
430	5.01E-04	**700**	5.53E-04	**970**	5.26E-04
440	5.01E-04	**710**	5.53E-04	**980**	5.26E-04
450	5.01E-04	**720**	5.53E-04	**990**	5.26E-04
460	5.01E-04	**730**	5.53E-04	**1000**	5.83E-04

A.3.2. CCD ($C_s(\lambda)$) Detector's Response:

Table 18: CCD detector's spectral response [39].

Wavelength (nm)	CCD Response (mW/cm^2 count)	Wavelength (nm)	CCD Response (mW/cm^2/count)
400.38	4.20E-01	**600.30**	9.70E-01
410.23	4.20E-01	**610.09**	9.70E-01
420.05	5.00E-01	**620.28**	9.65E-01
430.29	5.00E-01	**630.02**	9.65E-01
440.07	5.00E-01	**640.16**	9.65E-01
450.27	5.00E-01	**650.26**	9.65E-01
460.01	5.00E-01	**660.34**	9.00E-01
470.16	5.00E-01	**670.38**	1.10E+00
480.29	5.00E-01	**680.39**	1.10E+00
490.39	5.00E-01	**690.37**	1.10E+00
500.03	8.35E-01	**700.33**	7.00E-01
510.09	5.00E-01	**710.25**	7.00E-01
520.12	5.00E-01	**720.13**	6.00E-01
530.13	5.00E-01	**730.40**	4.90E-01
540.11	5.00E-01	**740.22**	4.60E-01
550.06	9.20E-01	**750.01**	4.70E-01
560.42	9.20E-01	**760.18**	4.70E-01
570.32	9.20E-01	**770.31**	4.20E-01
580.20	9.20E-01	**780.00**	3.70E-01
590.05	9.20E-01	**800.88**	3.00E-01

A.4. Preliminary Analysis

A.4.1. Initial Cost Analysis

For a sheet of Ce:YAG with a dimension of 1.00x1.00x0.005 m^3 to be used for a typical 1.00x1.00 m^2 solar cell panel:

$$m = V \cdot \rho_{Ce:YAG} = l \cdot w \cdot t \cdot \rho_{Ce:YAG} = (1.0 \cdot 1.0 \cdot 0.0005)m^3 \cdot \left(4560000 \frac{g}{m^3}\right)$$

$$= 2280\ g$$

Table 19: Alpha Aesar's and MTI Corporation's price for each element.

Material	Weight (g)	Price ($) Alpha Aesar [60]	Price ($) MTI Corporation [61]
$Y_3Al_5O_{12}$	100.00	610.00	180.00
Y	25.00	308.00	--
Al	1000.00	75.70	--
O	100.00	0.30	--
Ce	25.00	694.00	460.36

Table 20: Weight of element or compound for a total Ce:YAG weight of 2280 g.

Material	Mols %	Molar Weight (g/mol)	Weight %	Weight (g)
Total	100.00	602.84	100.0	2 280.00
$Y_{2.82}Al_5O_{12}$	99.10	577.61	95.82	2 184.61
$Y_{2.82}$	14.10	88.906	41.59	948.23
Al_5	25.00	26.98	22.38	510.21
O_{12}	60.00	15.99	31.85	726.17
$Ce_{0.18}$	0.900	140.12	4.18	95.39

Table 21: Price for each element for a total weight of 2280 g.

Material	$Y_{2.82}$	Al_5	O_{12}	$Ce_{0.18}$	$Y_{2.82}Al_5O_{12}$	Total
Price/Element – Alpha Aesar ($)	11 682.24	108.67	2.18	2 648.06	13 326.11	14 441.15 – 15 974.17
Price/Element MTI Corporation ($)	--	--	--	1 756.57	3 932.30	5 688.87

A.4.2. Cost Analysis for the New Design

Table 22: Weight of each element for a total of 1.50 g.

Material	Mols %	Molar Weight (g/mol)	Weight %	Weight (g)
Total	100.00	602.84	100.0	1.50
$Y_{2.82}Al_5O_{12}$	99.10	577.61	95.82	1.44
$Y_{2.82}$	14.10	88.906	41.59	0.62
Al_5	25.00	26.98	22.38	0.33
O_{12}	60.00	15.99	31.85	0.48
$Ce_{0.18}$	0.900	140.12	4.18	0.06

Table 23: Price for each element or compound for a total of 1.50 g of $Ce_{0.18}$:$Y_{2.82}Al_5O_{12}$.

Material	$Y_{2.82}$	Al_5	O_{12}	$Ce_{0.18}$	$Y_{2.46}Al_5O_{12}$	Total
Price/Element Alpha Aesar ($)	7.69	0.07	0.001	1.74	8.77	9.50 – 10.51
Price/Element MTI Corporation ($)	--	--	--	2.59	1.16	3.75

A.5. Monte Carlo Simulation Code

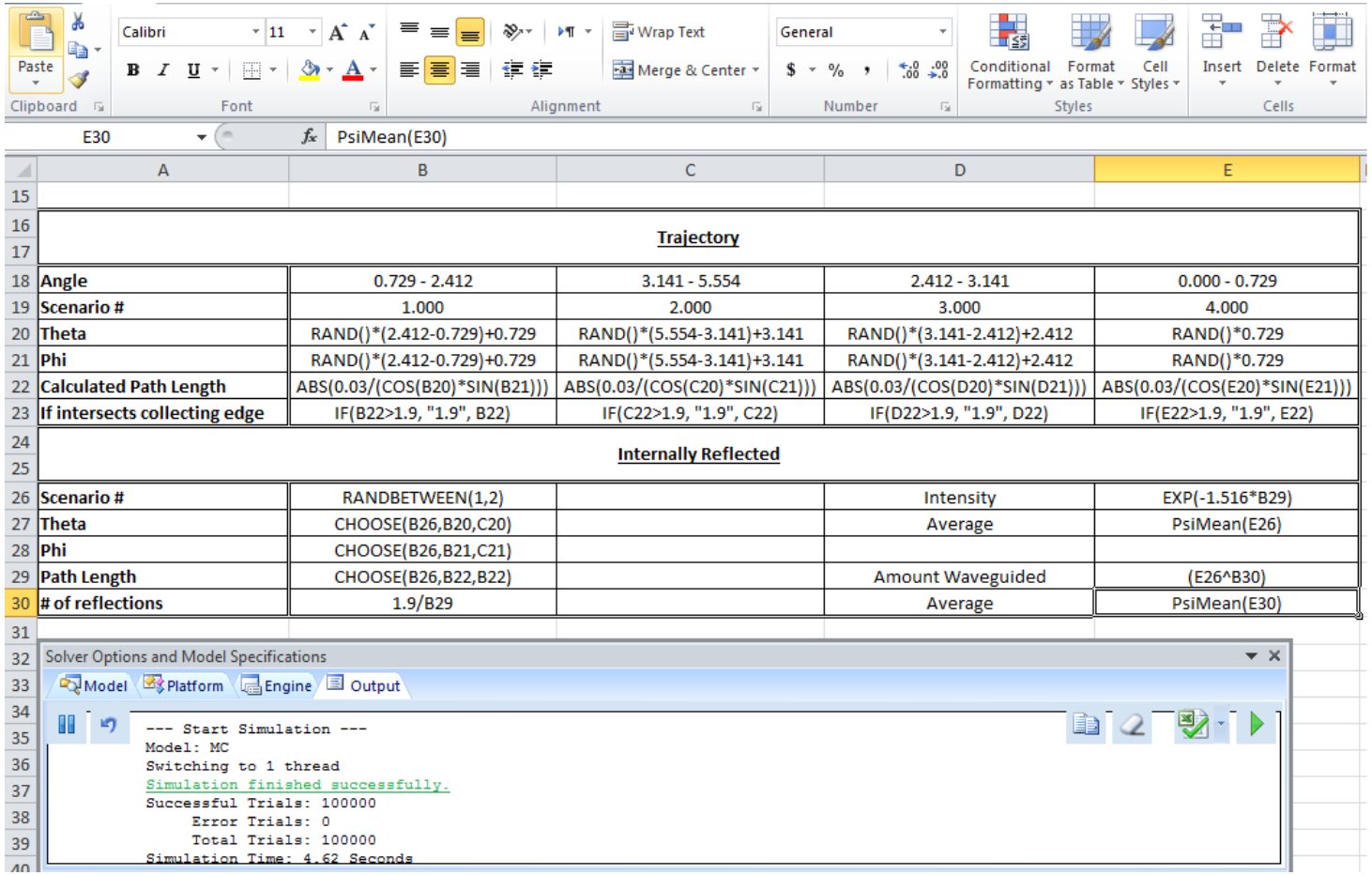

Paste | Calibri | 11 | Wrap Text | General | Conditional Formatting | Format as Table | Cell Styles | Insert | Delete | Format

Clipboard | Font | Alignment | Number | Styles | Cells

E30 | PsiMean(E30)

	A	B	C	D	E
15					
16	**Trajectory**				
17					
18	**Angle**	0.729 - 2.412	3.141 - 5.554	2.412 - 3.141	0.000 - 0.729
19	**Scenario #**	1.000	2.000	3.000	4.000
20	**Theta**	RAND()*(2.412-0.729)+0.729	RAND()*(5.554-3.141)+3.141	RAND()*(3.141-2.412)+2.412	RAND()*0.729
21	**Phi**	RAND()*(2.412-0.729)+0.729	RAND()*(5.554-3.141)+3.141	RAND()*(3.141-2.412)+2.412	RAND()*0.729
22	**Calculated Path Length**	ABS(0.03/(COS(B20)*SIN(B21)))	ABS(0.03/(COS(C20)*SIN(C21)))	ABS(0.03/(COS(D20)*SIN(D21)))	ABS(0.03/(COS(E20)*SIN(E21)))
23	**If intersects collecting edge**	IF(B22>1.9, "1.9", B22)	IF(C22>1.9, "1.9", C22)	IF(D22>1.9, "1.9", D22)	IF(E22>1.9, "1.9", E22)
24					
25	**Internally Reflected**				
26	**Scenario #**	RANDBETWEEN(1,2)		Intensity	EXP(-1.516*B29)
27	**Theta**	CHOOSE(B26,B20,C20)		Average	PsiMean(E26)
28	**Phi**	CHOOSE(B26,B21,C21)			
29	**Path Length**	CHOOSE(B26,B22,B22)		Amount Waveguided	(E26^B30)
30	**# of reflections**	1.9/B29		Average	PsiMean(E30)
31					

Solver Options and Model Specifications

Model | Platform | Engine | Output

```
--- Start Simulation ---
Model: MC
Switching to 1 thread
Simulation finished successfully.
Successful Trials: 100000
     Error Trials: 0
     Total Trials: 100000
Simulation Time: 4.62 Seconds
```

Figure 54: A snapshot of the code used for Monte Carlo simulation in Excel.

A.6. Filters' Transmission

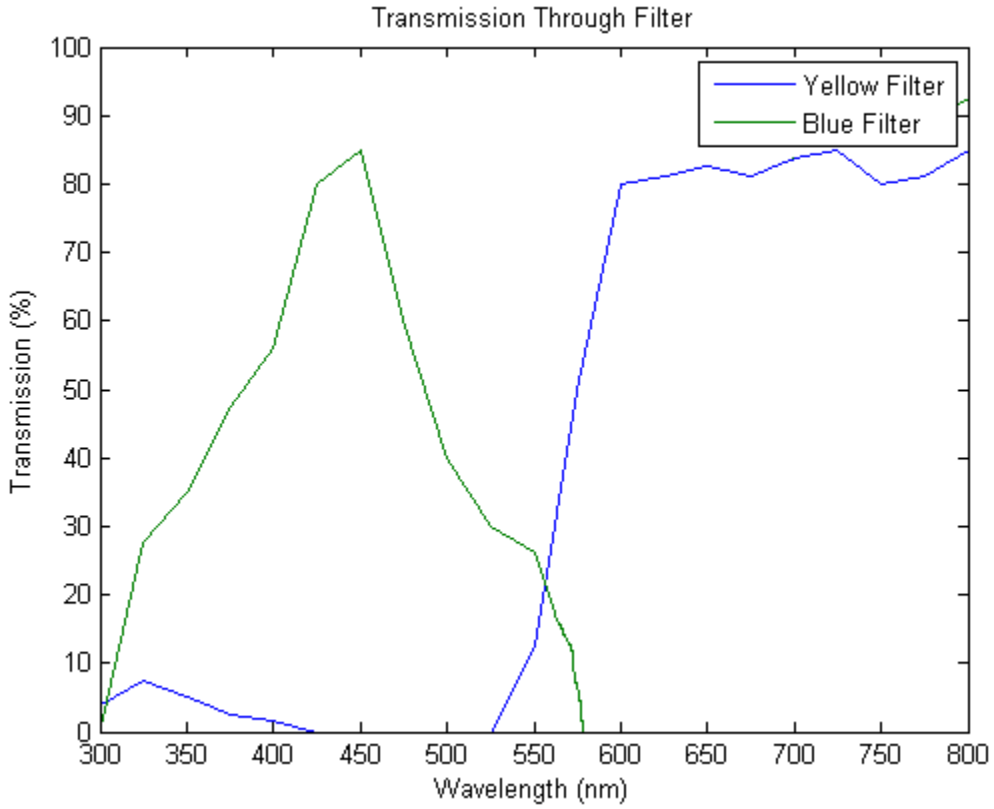

Figure 55: Transmission through filters for any given wavelength.

A.7. 2D Plot of Luminance with Respect to Position of Lenses

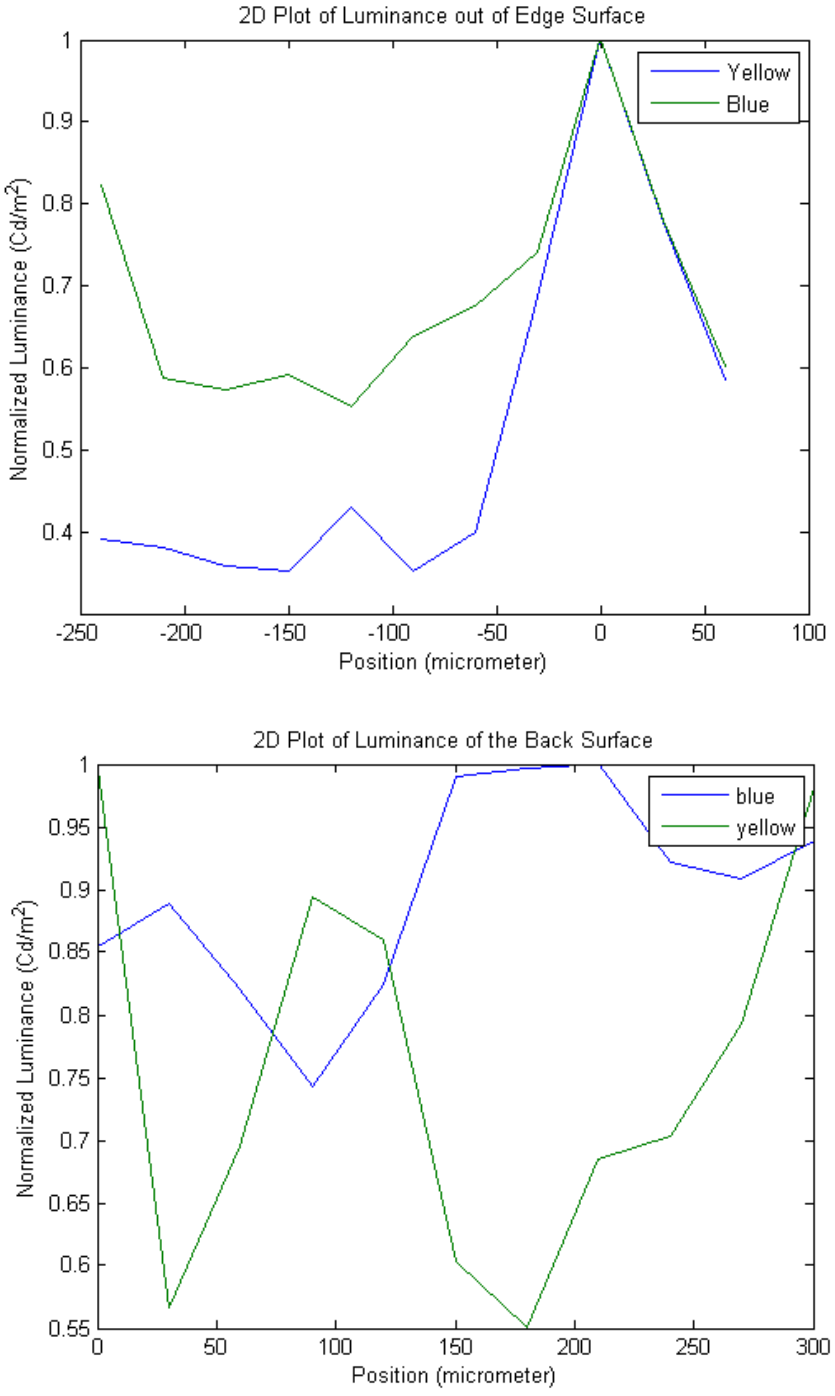

Figure 56: 2D plot of luminance with respect to position of lenses to Ce:YAG.

A.8. LED Image Size

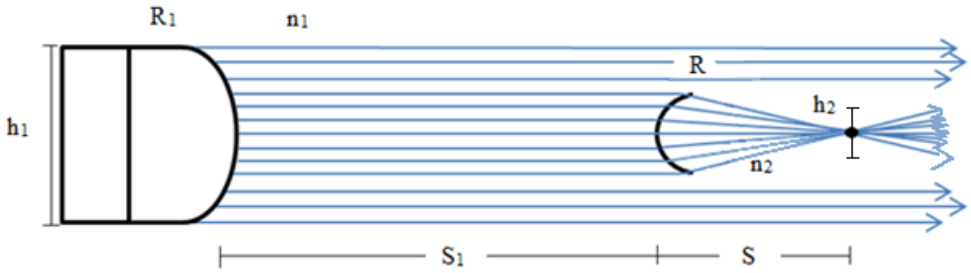

Figure 57: LED image size produced after the refraction of light through lenses [70].

$$\frac{n_1}{S_1} - \frac{n_2}{S} = \frac{n_1 - n_2}{R}$$

$$S = -\left[\frac{n_1 - n_2}{R} - \frac{n_1}{S_1}\right]^{-1}\left(\frac{1}{n_2}\right)^{-1}$$

$$S = -\left[\frac{1.00 - 1.50}{0.1143} - \frac{1}{10.00}\right]^{-1}\left(\frac{1}{1.50}\right)^{-1} = -0.3509$$

$$m = -\frac{n_1 S}{n_2 S_1} = \frac{h_1}{h_2}$$

$$h_2 = -\frac{n_1 S}{n_2 S_1} h_1 = -\frac{(1)(-0.3509)}{(1.5)(10.0)} = 0.02339\ cm$$

∴ Size of image produced by the LED through lenses is 0.02339 cm

A.9. Gaussian Distribution of LED (graph and function derivation)

Gaussian Distribution:

$$f(x) = a \cdot exp\left(-\frac{(x-b)^2}{2 \cdot c^2}\right) + d$$

a = maximum luminance for an LED = 32.07

b = position of the centre of the peak = 0.25

c = standard deviation = $\frac{FWHM}{2\sqrt{2 \cdot \ln(2)}} = \frac{0.234}{2\sqrt{2 \cdot \ln(2)}} = 0.09937$

d = y-intercept = 0

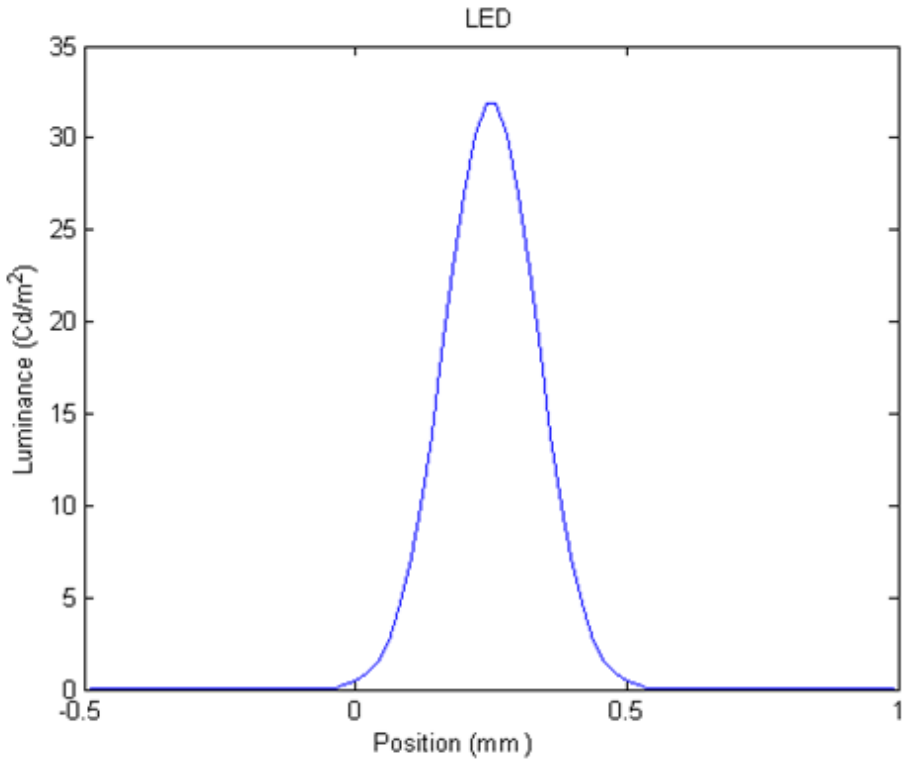

Figure 58: Gaussian distribution of LED luminance.

A.10. Luminous Efficacy

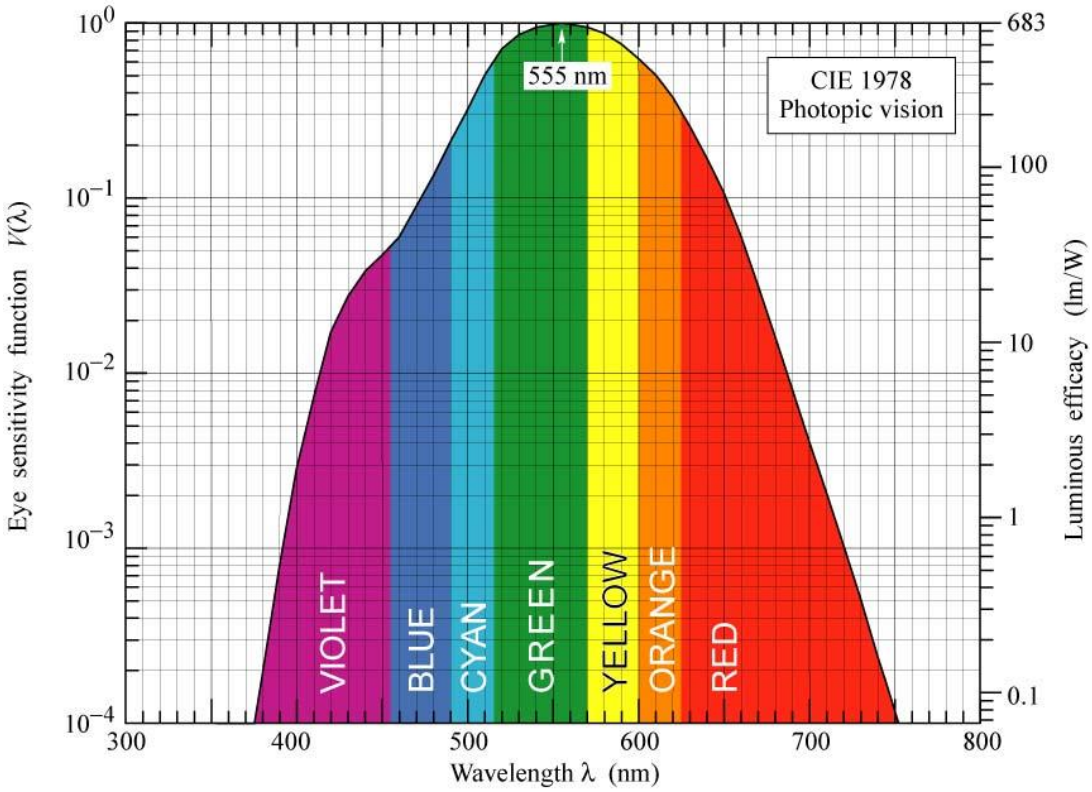

Figure 59: Eye sensitivity function and luminous efficacy for any given wavelength [69].

A.11. LED Optical Power as a Function of Wavelength

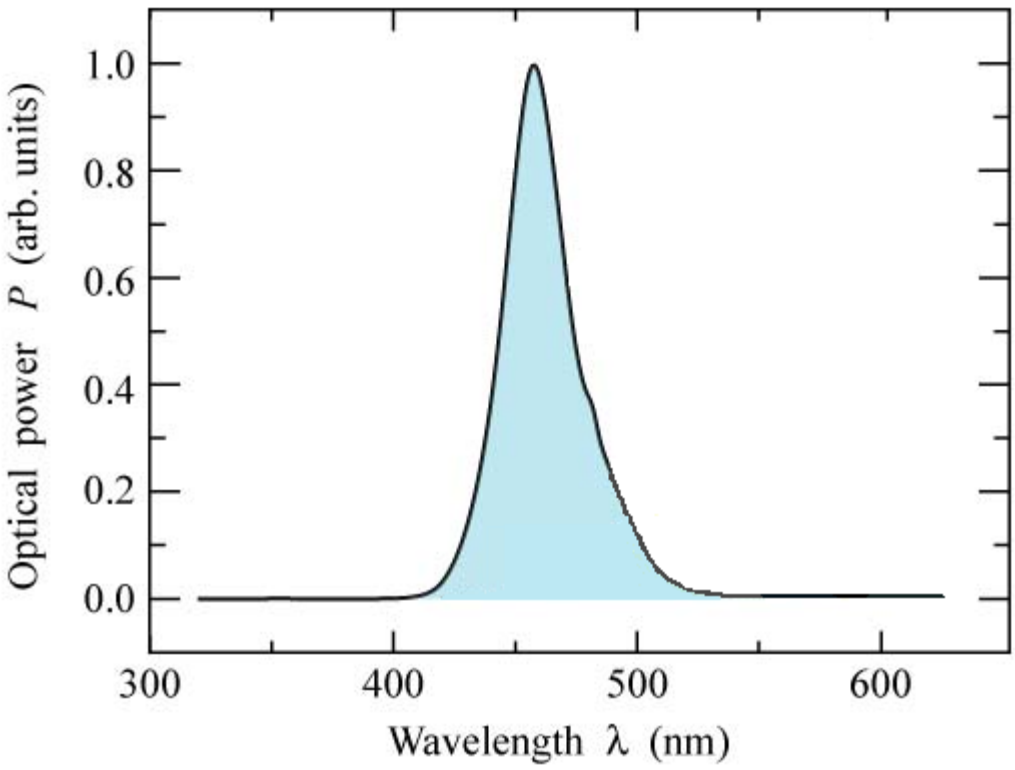

Figure 60: Normalized optical power of LED as a function of wavelength [68]

A.12. Acrylic Transmission

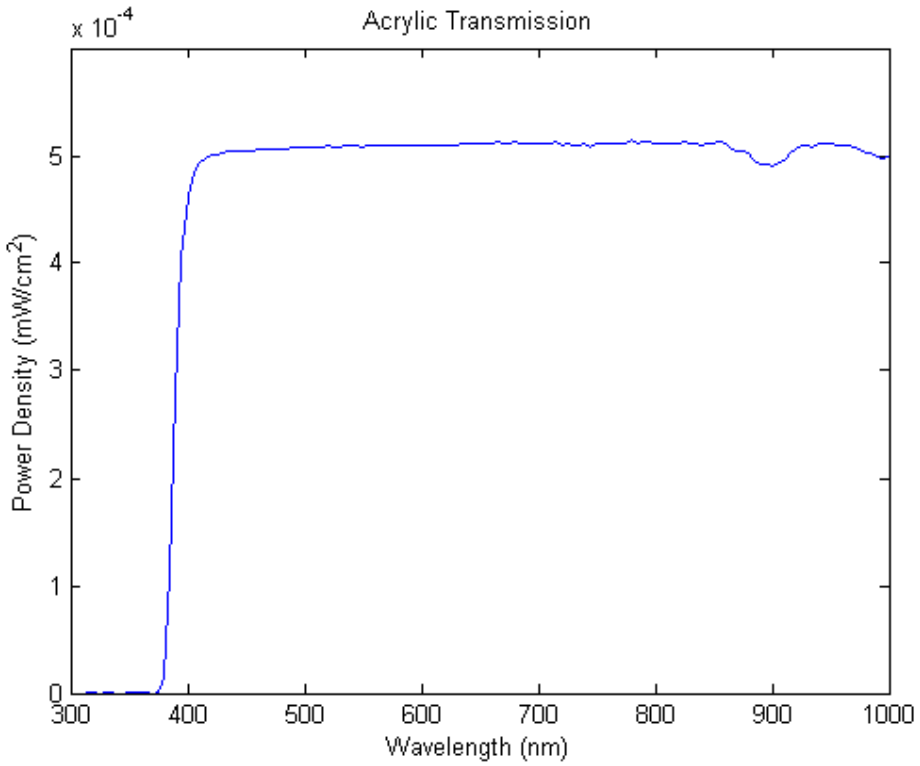

Figure 61: Transmission through acrylic substrate for any given wavelength.